

Evaluation of slaking and crack evolution using photographic method and  
the effects on shear strength of mudstones

写真技術を活用した泥岩のスレーキングおよびひび割れ進展状況の  
評価とせん断強度への影響

October, 2023

Danxi SUN  
孫 丹曦



Evaluation of slaking and crack evolution using photographic method and  
the effects on shear strength of mudstones

写真技術を活用した泥岩のスレーキングおよびひび割れ進展状況の  
評価とせん断強度への影響

October, 2023

Waseda University Graduate School of Creative Science and Engineering

Department of Civil and Environmental Engineering, Research on  
Geotechnical Engineering

Danxi SUN  
孫 丹曦

## Abstract

The wide distribution of mudstone affects the efficient construction and safe maintenance of projects due to the slaking behavior, volume change and cracking evolution. To explore the mechanisms of mudstone slaking, swelling strain tests and atmospheric and vacuum cyclic drying–wetting slaking tests were conducted for a natural mudstone from the Akita Prefecture, Japan. Moreover, a multi-view approach was used to measure the evolution of the three-dimensional particle shape during cyclic drying–wetting slaking tests. The results imply that swelling strains of natural specimens are lower than that of remolded ones. In slaking tests, the slaking rate in atmospheric slaking tests is higher than in vacuum slaking tests. However, unlike the decrease in the slaking rate in atmospheric slaking tests, the slaking rate in vacuum slaking is constant because it eliminates the air-breakage phenomenon. Moreover, the shape parameter extracted using the multi-view approach indicates that the medium particle has a larger specific surface area caused by the typical layered slaking phenomenon observed during slaking. Finally, a new insight into the differential swelling mechanism caused by the uneven distribution of water during slaking is proposed. A larger specific surface area of particles in the vacuum slaking tests proved this mechanism. Furthermore, the particle shape analysis can explain the assumption of dividing particles into three groups in a tri-piecewise linear fractal dimension model. Volume change of mudstone along wetting and drying is also explored by swelling strain and shrinkage tests, especially under the influence of sodium chloride solution. Results show that swelling strains of Akita mudstone decrease with the increase of vertical stress and increase with the increase of dry density. With different concentration of sodium chloride solution, the swelling strains increase due to the

conversion of some calcium-based montmorillonite into sodium-based montmorillonite under low stress and this increase can be compacted by applying larger stress. Except swelling behavior, sodium chloride solution also restrains the shrinkage behavior of Akita mudstone. Furthermore, the cracking evolution is weakened due to the decrease in shrinkage capacity.

Preferred orientation of particles and pores will result in the macroscopic anisotropy of compacted soil. In this study, the SEM images of compacted crushed mudstone with different dry densities were analyzed and the orientation of pores and particles were counted. The results show that with the increase of dry density, the orientation distribution of pores and particles will appear anisotropy: the particle orientation distribution concentrates in the direction perpendicular to the compacting direction. While the pore orientation distribution gradually concentrates on the direction which is perpendicular to and parallel to compacting direction. The grain anisotropy index increases with the increase of dry density, and the growth slows down after reaching the maximum dry density.

Key words: Muti-view approach, 3D model, Slaking behavior, Mudstone, Cracking evolution, Soil anisotropy, Swelling behavior, Shrinkage behavior

## Content

Chapter 1.	INTRODUCTION .....	6
1.1	Background .....	7
1.2	Slaking mechanisms of mudstone.....	9
1.3	Volume change and cracking evolution.....	12
1.4	Research objectives.....	14
1.5	The innovations of this study .....	15
1.6	Construction of the thesis.....	15
Chapter 2.	MATERIALS AND PHYSICAL PARAMETERS .....	18
2.1	Materials .....	19
2.2	Physical parameters .....	19
2.2.1	Soil particle density.....	19
2.2.2	Liquid limit and plastic limit.....	21
2.2.3	Montmorillonite content .....	22
2.3	Accelerated rock-slaking test.....	23
2.4	X-ray diffraction (XRD) tests .....	25
2.4	Scanning electron microscope (SEM) tests .....	31
Chapter 3.	STUDY ON SWELLING STRAIN BEHAVIOR OF AKITA MUDSTONE WETTED BY NA CL SOLUTION UNDER DIFFERENT CONCENTRATION AND VERTICAL CONFINING STRESSES .....	33
3.1	Testing equipments and procedures.....	34
3.1.1	Swelling pressure test .....	34
3.1.2	Swelling strain test.....	34
3.1.3	Leaching testing of Akita mudstone with distilled water or NaCl solutions .....	38
3.2	Results and discussion .....	40
3.2.1	Swelling pressure and strain of black mudstone.....	40
3.2.2	Swelling strain of Terashima mudstone.....	41
3.2.3	Swelling strain and pressure of Akita mudstone.....	43
3.2.4	Swelling strain of Akita mudstone with different concentration of NaCl solution and different pressure .....	48
3.2.5	Swelling strain and pressure of Akita mudstone.....	51

Conclusion .....	52
Chapter 4. THE IMPROVEMENT AND APPLICATION OF MUTI-VIEW APPROACH .....	53
4.1 Testing overview .....	54
4.2 Results and discussion .....	60
4.2.1 Application of muti-view approach on different scales .....	60
4.2.2 Improvement of muti-view approach.....	61
4.2.3 The accuracy of the muti-view approach.....	65
Conclusion .....	68
Chapter 5. STUDY ON SLAKING MECHANISMS OF A MUDSTONE BY THREE-DIMENSIONAL SHAPE ANALYSIS USING THE MUTI-VIEW APPROACH .....	69
5.1 Testing overview.....	70
5.2 Results and discussion .....	72
5.2.1 General characterization of the slaking process.....	72
5.2.2 Shape evolution of particles.....	78
5.2.3 Slaking mechanism of Akita mudstone .....	84
5.2.4 Fractal models of mudstone .....	87
Conclusions.....	88
Chapter 6. SLAKING BEHAVIOR OF AKITA MUDSTONE UNDER STRESS AND THE SHEAR STRENGTH EVOLUTION DURING SLAKING PROCESS...90	
6.1 Testing overview.....	91
6.2 Results and discussion .....	93
6.2.1 Slaking behavior of Akita mudstone under stress.....	94
6.2.2 Shear strength evolution during slaking process .....	96
6.2.3 Slaking mechanism of Akita mudstone under stress .....	99
Conclusion .....	100
Chapter 7. SHRINKAGE AND CRACKING EVOLUTION OF AKITA MUDSTONE WITH DIFFERENT NA CL SOLUTION .....	101
7.1 Testing overview.....	102
7.1.1 Cracking test .....	102
7.1.2 Soil-water retention curve test .....	104
7.1.3 Shrinkage test.....	105

7.2 Results and discussion .....	107
7.2.1 Cracking evolution of Akita mudstone with different concentration of NaCl solution .....	107
7.2.2 Shrinkage behavior of Akita mudstone with different concentration of NaCl .....	116
7.2.3 Relationship between cracking evolution and shrinkage behavior of Akita mudstone with different concentration of NaCl.....	119
Conclusions.....	123
Chapter 8. SLAKING TESTS ON MUDSTONE AND PORE AND PARTICLE ORIENTATION OF COMPACTED BLACK MUDSTONE.....	125
8.1 Testing overview.....	126
8.2 Results and discussion .....	130
8.2.1 Soil structure and EDS analysis.....	130
8.2.2 Slaking tests on natural mudstone.....	131
8.2.3 Slaking tests on remolded mudstone.....	136
8.2.4 Pores and particles orientation distribution.....	140
Conclusions.....	145
Chapter 9. APPLICATION IN PRACTICAL FIELD.....	147
9.1 Overview.....	148
9.2 Application of mudstone in embankment .....	151
9.3 Application of multi-view approach .....	156
9.4 Slaking problem in tunnel.....	159
9.5 Future plan .....	162
Conclusions.....	162
Chapter 10. CONCLUSIONS.....	164
Chapter 11. References .....	170
Chapter 12. Figure list .....	182
Chapter 13. Table list.....	187



## **Chapter 1. INTRODUCTION**

## 1.1 Background

As clay-bearing rocks, mudstones are not conducive for the safe maintenance of projects in tunnels (Perras, Wannemacher and Diederichs, 2015; Sun *et al.*, 2020), slopes (Yang, Zhang and Zhou, 2006; X. Zhang *et al.*, 2020) and underground storage facilities (Wang *et al.*, 2011; Zhang *et al.*, 2015). **Figure 1-1** shows that the slaking of mudstone in tunnels results in layer-by-layer stone peeling, significantly affecting the project's safety. Mudstone has been widely used in embankments of expressways in Japan (Sakai and Nakano, 2019). However, the failure of mudstone embankments, such as the Tomei expressway embankment failure (Yasuda *et al.*, 2012), caused substantial economic losses. As a standard engineering characteristic, the primary weathering mode from mudstone to soils, the slaking behavior would severely affect the mudstone's strength and gradation and further cause engineering disasters.

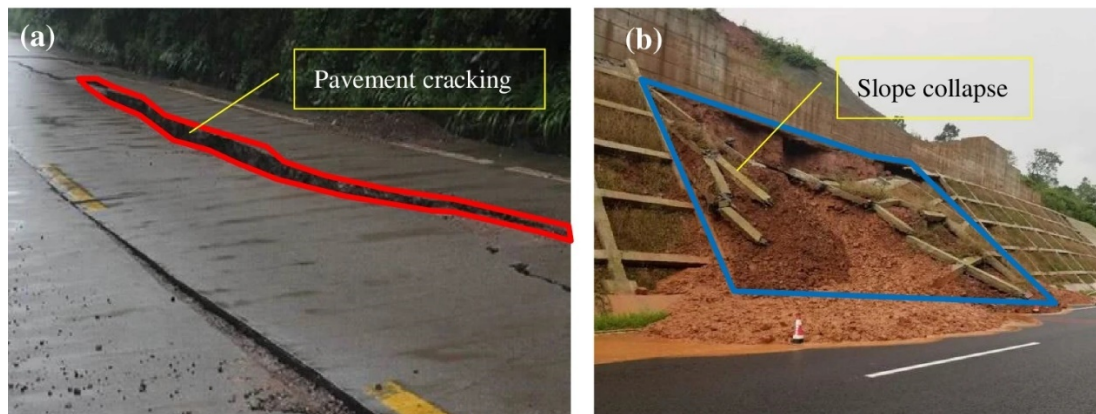


**Figure 1-1 Failure of highway embankment and slaking problem of mudstone in Japan**

In addition to Japan, mudstone has also been widely used in the construction of roads, railways, and tunnels in many other countries. With the continuous expansion of China's

transportation network, there has been a significant increase in the number of expressway construction projects in western mountainous regions. However, these projects are faced with two prominent challenges. Firstly, the lack of suitable embankment fillers such as gravel and sand, which are in short supply and expensive to transport from distant sources. Secondly, the excavation of slopes and tunnels results in large amounts of mudstone waste slag being generated (Ju, Qiu and Yang, 2022).

To overcome these challenges, some projects have attempted to use mudstone waste slag as an alternative embankment filler, in order to shorten the construction period and reduce costs. However, this approach has resulted in a number of road deterioration problems due to the poor mechanical properties of the mudstone, as illustrated in Figure 1-2. Such issues have highlighted the need for further research to improve the understanding of the geotechnical properties of mudstone and its potential applications in road and transportation infrastructure projects.

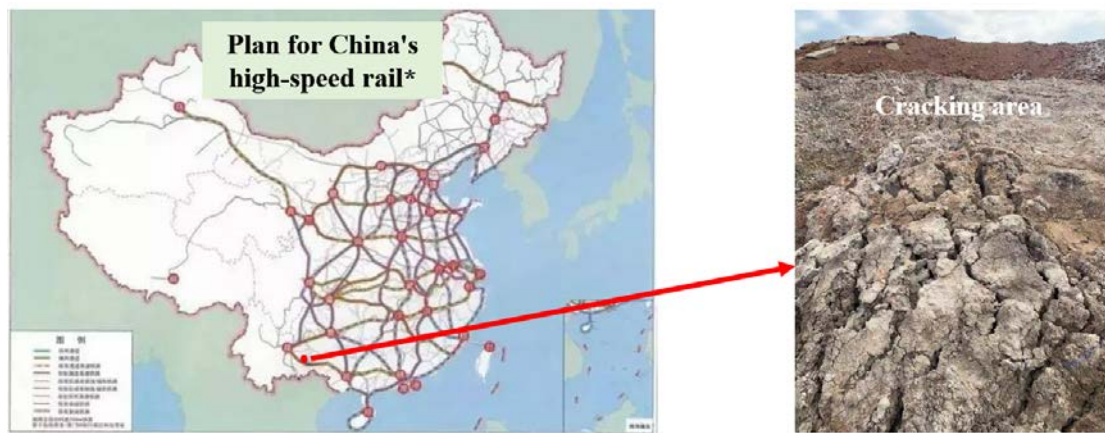


**Figure 1-2 Road diseases in He-chang Expressway, China (Ju, Qiu and Yang, 2022)**

Swelling and shrinkage behavior of some mudstone may result in the uplift or the settlement of expressway embankment (Hopkins and Beckham, 1998; Dai *et al.*, 2021).

Moreover, the volume change of soil may result in the cracks in the ground. The effect

of crack in soil is not a trivial matter (see **Figure 1-3**). The desiccation cracks in soil not only affects the strength of soil, but also provides convenient channels for infiltration and evaporation (Boynton and Daniel, 1985; Rayhani *et al.*, 2007). These influences aggravate the soil swelling and shrinkage. Thus, it is necessary to study the slaking behavior mechanism.



**Figure 1-3 Cracking ground on the field besides high-speed rail in southwest of China**

## 1.2 Slaking mechanisms of mudstone

Many scholars have studied slaking characteristics and mechanisms (Shakoor, 2016; Shen *et al.*, 2019; Liu *et al.*, 2020; Selen, Panthi and Vistnes, 2020). Some tests include slake durability (Franklin and Chandra, 1972) and cyclic drying–wetting slaking test (Sakai and Nakano, 2019; Su *et al.*, 2020) to quantitatively assess the slaking behavior. The slaking mechanisms of mudstone can be summarised in three categories (Liu *et al.*, 2020): (1) the air-breakage phenomenon, (2) differential swelling and (3) the dissolution of cement agents. Studies focus on the influence of pH (Fereidooni and Ghobadi, 2015; Su *et al.*, 2020) and salt action (Kang *et al.*, 2015) during the slaking

process, whereas the air-breakage phenomenon has been proven crucial in the slaking process via slake durability tests (Liu *et al.*, 2020). The atmospheric and vacuum cyclic drying–wetting slaking tests were conducted to explore the different slaking mechanisms in this research.

Some shape parameters are detected to obtain more details during slake durability and cyclic drying–wetting slaking tests. For example, computed tomography (CT) (Jiang, Cui and Feng, 2014) and picture analysis (Fernlund, 1998; Kolay and Kayabali, 2006; Su *et al.*, 2020) were applied to study the three-dimensional (3D) structure of pores and the two-dimensional (2D) shape of particles during slaking behavior. As a non-destructive observation technique, CT can obtain more information than conventional 2D image analysis. However, the high cost of CT equipment limited the 3D shape study in slaking behavior. A method of 3D visualisation was introduced into the study of slaking behavior for 3D particle analysis to overcome this limitation. The multi-view approach has been widely used in many aspects to synthesise 3D models by photos taken from different directions, e.g. 3D world scene reconstruction, filmmaking and virtual reality (Agarwal *et al.*, 2011; Wöhler, 2012). The technique is also used in scientific research. For example, Tafti *et al.* (2015) applied this technology in scanning electron microscopy (SEM) for applications comprising medicine, pharmacology, chemistry and mechanics. However, although the multi-view approach has been introduced into the surface analysis of rock walls (Thoeni *et al.*, 2014) and land surfaces (Asner, 2000), this technique has rarely been applied to quantitative 3D particle analysis in geotechnology.

In general, mudstone often bears ambient stresses in engineering applications, such as construction of expressways, tunnels and dams (Lee, Tien and Juang, 1996; Sattar *et al.*, 2011; Mingbin and Guoguo, 2015; Zhang *et al.*, 2017; Z. Zhang *et al.*, 2020).

Especially in the drawdown area under conditions of Three Gorges Reservoir operation, the stress and cyclic wetting-drying contribution to the slaking problem. Moreover, the ambient stresses on mudstone resulting in accelerating slaking behavior has been proved (Z. Zhang *et al.*, 2020).

Particle size of mudstone is usually used for evaluation of slaking degree. Two kinds of index are calculated by particle size: (1) In slake durability test, slaking durability index ( $I_d$ ) is calculated by the weight of particle with diameter less than 2mm (Franklin and Chandra, 1972; Shakoor, 2016); (2) In cyclic wetting and drying test, slaking ratio ( $SL_{ratio}$ ) calculated by particle size distribution curves (Gautam and Shakoor, 2013; Su *et al.*, 2020). The slaking behavior changes the particle size distribution (PSD) of mudstone and further influence the strength of this material. And the changes on strength of mudstone influence the safety of engineering facilities. For example, the influence of mudstone PSD changes in shear strength has been studied by triaxial compression shear tests (Yamaguchi *et al.*, 1988). Moreover, the direct shear tests on soft rocks with different PSDs were conducted for investigating the evolution of the cohesion ( $c$ ) and angle of internal friction ( $\phi$ ) (Zhong *et al.*, 2016; Wang *et al.*, 2018). However, the PSDs is just artificially determined by well-graded or poorly graded mudstone in these previous study (Zhong *et al.*, 2016; Wang *et al.*, 2018), which is may different from the actual PSD changes caused by slaking behavior.

This study conducted cyclic drying-wetting slaking tests for Akita mudstone, which has been used for embankments of expressways in Japan. During the tests, 3D models of slaked mudstone particles were synthesised from 2D images and shape parameters were extracted from these models. Furthermore, different slaking mechanisms might lead to different slaking particle shapes. Thus, vacuum cyclic drying-wetting slaking tests were conducted to explore the slaking mechanism via shape analysis. In addition,

the changes in PSD caused by the slaking behavior under different vertical stresses were also obtained. Specimens formulated with the same mixing proportions of soil particles as PSDs obtained by the slaking process will be used in direct shear experiments to study the evolution of the cohesion ( $c$ ) and angle of internal friction ( $\varphi$ ) during the slaking process.

### 1.3 Volume change and cracking evolution

Soils with swelling and shrinkage characteristics are widely distributed around the world, and they are notoriously problematic for the infrastructures, such as high-speed railway, light house, etc., due to the significant volume change during the drying-wetting cycles (Yuan *et al.*, 2016, 2019; Jiang *et al.*, 2018). Swelling properties have been widely studied in the past few decades (Komine and Ogata, 1994, 2003; Wang *et al.*, 2020). And the mineral such as montmorillonite in the clayey soil may results in the swelling behavior due to increasing of the basal spacing (Foster, Savins and Waite, 1954; Moore and Reynolds Jr, 1989; Wang, Komine and Gotoh, 2022). Influence of seawater and salt solution on the swelling behavior of clayey soils or clay-rich rock have been studied (Amorim *et al.*, 2007; Komine, Yasuhara and Murakami, 2009), which is related to the type of solution (e.g.  $K^+$  solution;  $Na^+$  solution;  $Ca^+$  solution) and dominant ion (e.g.  $Ca^+$ ;  $Na^+$ ) in CEC tests of material. As a clay-bearing rock, swelling behavior of mudstones also have been studied by some scholars (Zhang, Wiczorek and Xie, 2010; Zeng and Kong, 2019; Liu *et al.*, 2021; Yao *et al.*, 2022). As one kinds of method to evaluate the capacities of soil to retain and store water (Mo *et al.*, 2011), soil shrinkage characteristic has been studied in some researches (Stirk, 1954; Peng and Horn, 2005, 2013; Cornelis *et al.*, 2006). For saturated specimens, the soil

swells and loses water to shrink, and the volume shrinkage equals the volume of water loss. This part is called “normal” shrinkage (Groenevelt and Grant, 2004). However, when the soil is unsaturated and exceeds the entry value or cracking point, the soil shrinkage is less than the volume of water loss during this shrinkage process. And this shrinkage region is called “structural” shrinkage. Finally, the soil enters the residual shrinkage phase with less shrinkage or the zero-shrinkage stage (Peng and Horn, 2005, 2013). Moreover, hysteresis of shrinkage behavior for various salt concentrations on collapsible soils has been proved and analyzed by laboratory investigation (Sadeghi and Nasiri, 2021). However, the salt solution influence on the swelling and shrinkage behavior of mudstone.

Cracks are often observed in the ground due to the large volume change of soil, especially in the active zone (Shi, Chen and Zheng, 2014). As shown by Fredlund and Rahardjo, 1993, Morris, Graham and Williams, 1992 etc., the formation and evolution of cracks are controlled by suction and tensile strength. When soil loses water, it shrinks and cracks due to the internal stresses (Shin and Santamarina, 2011). Generally, contraction deformation at weak points is not in harmony with the surrounding areas, which results in tension concentration and cracking evolution (Towner, 1988; Zabat *et al.*, 1997; Weinberger, 1999). Thus, cracks form at these weak points (Tang *et al.*, 2011) and are named primary cracks in undisturbed soil (Li and Zhang, 2010). Subsequently, sub-cracks develop based on the primary cracks (Konrad and Ayad, 1997). Some conceptual models for the crack of soil were proposed (Konrad and Ayad, 1997; Colina and Roux, 2000; Li and Zhang, 2011).

In order to characterize cracks, several advanced techniques including microscope (Shin and Santamarina, 2011; Wang *et al.*, 2015), and digital camera (Vogel, Hoffmann and Roth, 2005; Chaduvula, Viswanadham and Kodikara, 2017; Tollenaar, Van



Paassen and Jommi, 2017) have been widely used, which mainly for the cracks on the surface of plate-like (Tang *et al.*, 2011) or bar-shaped specimens (Peron *et al.*, 2009; Kodikara and Costa, 2013). Some 2D geometrical parameters were used to quantify the evolution characteristics of desiccation cracks (Vogel, Hoffmann and Roth, 2005; Li and Zhang, 2011; Chaduvula, Viswanadham and Kodikara, 2017). In order to observe the internal cracks, 2D CT images were also used for crack analysis (Gao and El-Zein, 2021). In this study, digital camera was used for obtaining the cracking images from the thin specimens.

In this study, considering that coastal highways may be affected by seawater, swelling and shrinkage tests under NaCl solution were conducted for studying the volume change performance of mudstone. Moreover, digital camera was used to monitor the evolution of cracking in Akita mudstone under the influence of sodium chloride solution. Finally, the swelling, shrinkage and cracking evolution were analyzed.

#### 1.4 Research objectives

In this thesis, swelling properties of three kinds of mudstone were studied. Based on the swelling strain tests, improved multi-view approach was introduced for studying the mechanism of mudstone slaking behavior. Besides, considering different vertical confine stresses, the particle size distributions (PSD) of mudstone during slaking were studied and the shear strength evolution along with the changes of PSD were studied. The cracking evolution of mudstone under different concentration of NaCl solution was also studied by the corresponding shrinkage behavior. Finally, the orientation of pores and particles of compacted mudstone were also studied by scanning electron microscope (SEM) tests.

## 1.5 The innovations of this study

Firstly, based on improvement multi-view approach, the shape evolution of mudstone particles during slaking process and a new insight of slaking mechanism of Akita mudstone was proposed.

Secondly, the particle size distributions of mudstone under different vertical confine stress were studied and the shear strength evolution due to changes on particle size distribution was studied.

Thirdly, volume change of mudstone under NaCl solution was studied and the cracking evolution of mudstone were explained by the shrinkage behavior of mudstone.

Fourthly, pores and particles orientation distributions of crushed mudstone during compaction were studied by scanning electron microscope (SEM) tests.

## 1.6 Construction of the thesis

This thesis is divided into 9 chapters and can be seen as the following flow chart in

**Figure 1-4.** The details were presented as followings:

Chapter 1: Introduction. In this chapter, the background and literature survey were carefully interpreted.

Chapter 2: Materials and physical parameters. Three mudstones used in this study were introduced. The testing methodologies for physical parameters and their values were introduced.

Chapter 3: Swelling strains and pressures of three kinds of mudstones were studied. And the swelling strains of natural and remodeled Akita mudstones was also studied.

Chapter 4: Improvement of multi-view approach was proposed, and this improvement can optimize the 3D model results.

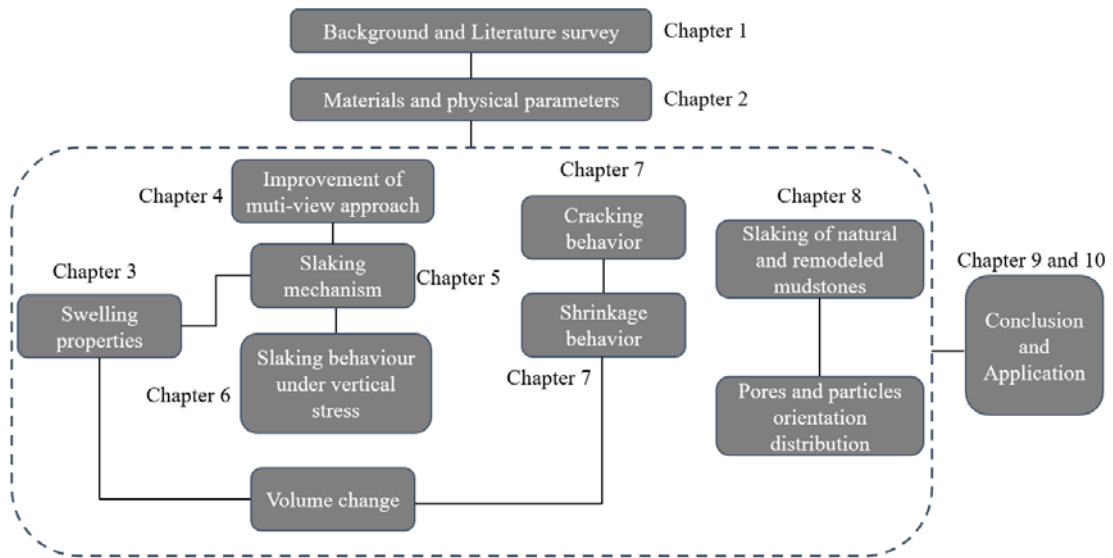
Chapter 5: Slaking mechanisms of Akita mudstone were studied by multi-view approach. A new insight of slaking mechanism (differential swelling) of Akita mudstone was proposed.

Chapter 6: The slaking behavior of mudstone under different vertical confining stresses was studied by evolution of mudstone particle size distributions (PSD). And the shear strength evolution caused by changes of PSDs was studied by direct shear tests.

Chapter 7: Shrinkage behavior of mudstone under different concentrations of NaCl solution was studied. And the relationship between shrinkage behavior and cracking evolution of mudstone was investigated.

Chapter 8: The slaking behavior of natural and remodeled mudstones were studied. And pores and particle orientation distributions of crushed mudstone during compaction were studied by scanning electron microscope (SEM) tests.

Chapter 9: Conclusion and Application. The conclusions from this thesis were concluded in this chapter. Besides that, how this thesis can progress the application of mudstones in project was interpreted.

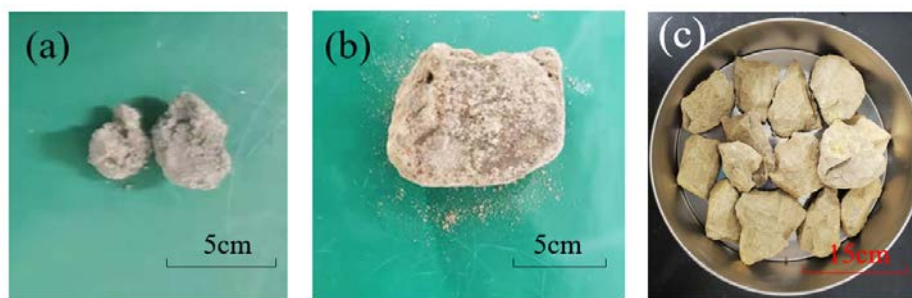


**Figure 1-4 Research flow**

## **Chapter 2. MATERIALS AND PHYSICAL PARAMETERS**

## 2.1 Materials

Three mudstones were used in this study and **Figure 2-1** shows outlooking of these three mudstones: a) Black mudstone is black and it includes three different levels of hardness, namely hard, medium, and soft. For the hard black mudstone, it is hard to broken by the harmer. While medium black is easy broken by the harmer. For the soft mudstone, we can break it by hands easily; b) Terashima mudstone one kind of grey mudstone which is from the Terashima and it is one kind of soft mudstone with observable pores; and c) Akita mudstone is yellow mudstone from the Akita Prefecture, and it is one kind of soft mudstone with distinct layered joints.



**Figure 2-1 Outlooking of three kinds of mudstone:(a) Black mudstone; (b) Terashima mudstone (c) Akita mudstone**

## 2.2 Physical parameters

### 2.2.1 Soil particle density



**Figure 2-2 Soil particle density testing details**

Soil particle density was measured by JIS A 1202:2020. It is noted that 5g powders was used for the soil particle density tests, even though ~10 g was recommended by JIS A 1202:2020. The test apparatuses required are as followings:

- (1) Pycnometer
- (2) Thermometer
- (3) Gas stove
- (4) Desiccator, decompression pump

Procedures for the test method are as follows:

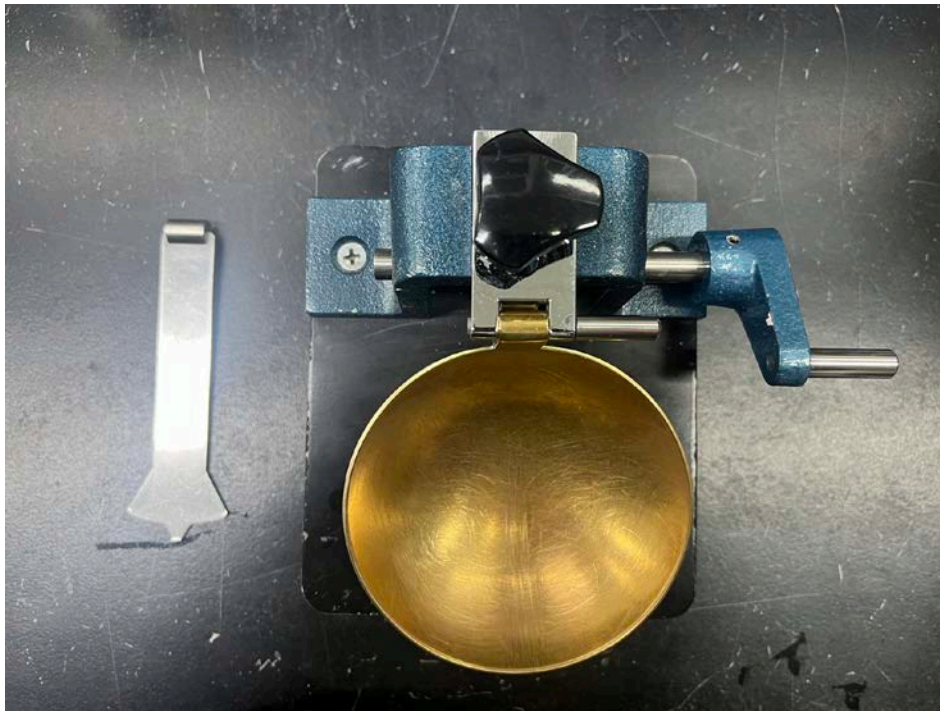
- (1) Measure the mass of the pycnometer and the mass when the pycnometer is filled with pure water. Also, measure the temperature of distilled water.
- (2) Put 50 ml of pure water and ~ 5 g of powdered sample in a beaker and disperse the sample using an ultrasonic disperser.
- (3) Use a funnel to transfer the beaker contents to the pycnometer and add pure water to two-thirds of the total pycnometer.
- (4) Use a Gas stove to heat the pycnometer in a water bath to promote degassing
- (5) Determine the density of soil particles.

Soil particle densities of mudstones are indicated in Table 2-1.

**Table 2-1 Soil particle densities of mudstones**

	Akita mudstone	Black mudstone	Terashima mudstone
Soil particle density (g/cm <sup>3</sup> )	2.58	2.72	2.69

### 2.2.2 Liquid limit and plastic limit



**Figure 2-3 Liquid limits testing device**

The liquid limit and plastic limit tests were conducted to investigate the changes in the state of soil depending on its water content. The liquid and plastic limit test is performed according to general method (JIS A 1205:2020). Following list presents the test apparatus.

- (1) Liquid limit measuring apparatus
- (2) Groove-cutting gauge
- (3) Glass plate
- (4) Spatula
- (5) Evaporating dish
- (6) Constant temperature drying oven
- (7) Round bar of 3 mm in diameter



Plastic and liquid limit of bentonites are indicated in Table 2-2.

**Table 2-2 Liquid and plastic limits of mudstones**

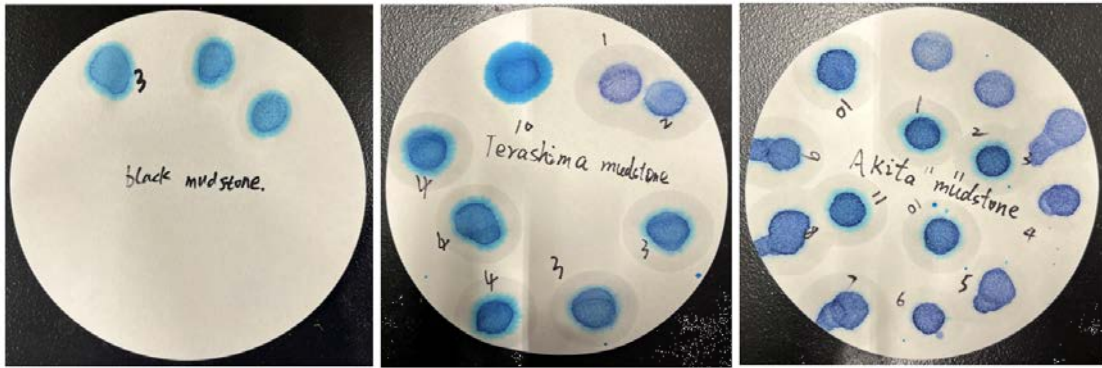
	MX80	KV1	KB
Liquid limit (%)	437.3	468.1	128.7
Plastic limit (%)	28.7	29.1	58.4
Plasticity index (%)	408.6	439	70.3

### 2.2.3 Montmorillonite content

The swelling properties of soft rock are mainly attributed to montmorillonite. Therefore, the content of montmorillonite is a significant indicator to describe the property of mudstones. Montmorillonite content was determined by the methylene blue adsorption capacity test using the spot method (JIS Z 2451:2019). The final results are revealed in Fig. 2-6. And, the montmorillonite contents of mudstones are listed in Table 2-3.

**Table 2-3 Montmorillonite contents of bentonites**

	Black mudstone	Terashima mudstone	Akita mudstone
Montmorillonite content (%)	4.3	5.7	15.7



**Figure 2-4 Montmorillonite content testing details**

### 2.3 Accelerated rock-slaking test

As a standard engineering characteristic, the primary weathering mode from mudstone to soils, the slaking behavior would severely affect the mudstone's strength and gradation and further cause engineering disasters. According to JGS 2124-2006, Accelerated rock-slaking tests on three kinds of mudstones were conducted to obtain the Slaking Index (see **Table 2-4**).

**Table 2-4 Definition of slaking classes (JGS 2125-2006)**

Class	0	1	2	3	4
A					
	There is no change.	Original shape remains with a few cracks.	Many cracks appear, specimen is divided into some fragments, and original shape can be recognized.	Whole body has crumbled; however, not muddy. Original shape cannot be recognized.	Whole body is muddy.
B					
	There is no change.	Original shape remains with a few cracks or with light circumferential disintegration.	Circumference has crumbled and it is difficult to recognize original shape.	Circumference has crumbled completely and separated into many particles. Original shape cannot be recognized.	Whole body is sandy.

A: Typical states for mudstone or fine-grained tuff

B: Typical states for siltstone, sandstone or coarse-grained tuff

The results of accelerated rock-slaking test can be seen in **Figure 2-5**. The rock specimens are put in the containers and then the water is added into the container. By comparing the definition of slaking classes, the Black mudstone with different levels of hardness can be classified as two different slaking level. For the hard and medium black mudstones, there seems no slaking behavior after add water. Thus, these two kinds of Black mudstone are classified as B0. However, the softer mudstone with observable pores is crumbling into sand in tens of seconds, which is classified as B4. The Terashima mudstone can be classified as A2 because it is crumbling into mud as shown in **Figure 2-5**. Meanwhile the Akita mudstone can be classified as B0. However, this classification does not indicate that Akita mudstone does not have slaking properties. In the following chapters, we will use other experiments to study the slaking characteristics of Akita mudstone.

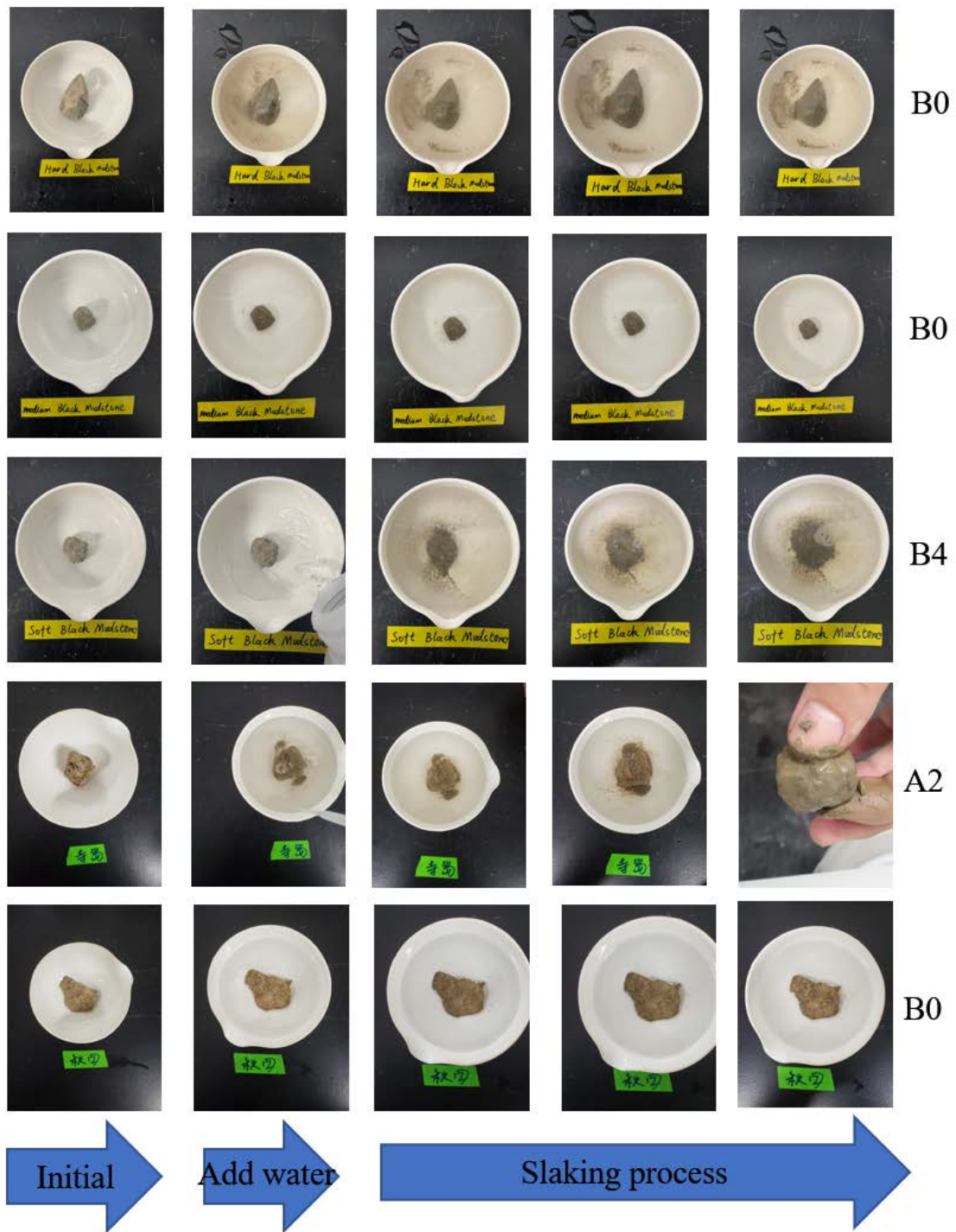


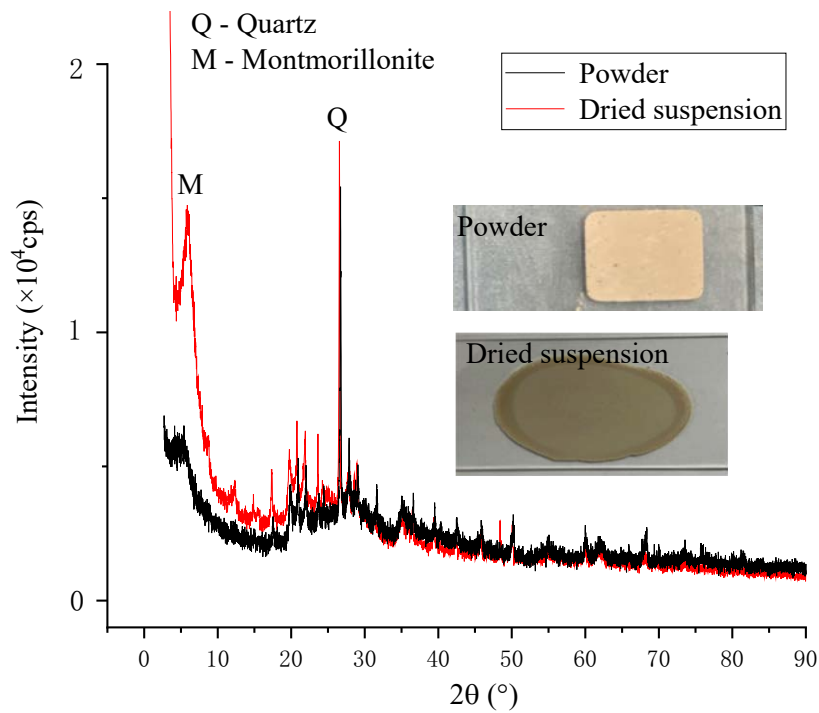
Figure 2-5 Results of accelerated rock-slaking tests

#### 2.4 X-ray diffraction (XRD) tests

Three kinds of mudstones were crashed into powder for X-Ray Diffraction (XRD) tests by RINT-UltimaIII (Rigaku Corp., Japan) as shown in **Figure 2-6** under the Bragg–Brentano geometry with an X-ray scan range  $2.7^{\circ}$ - $90^{\circ}$  and scan speed of  $10^{\circ}/\text{min}$  except black mudstone. X-ray scan range  $10^{\circ}$ - $90^{\circ}$  is used in black mudstone.

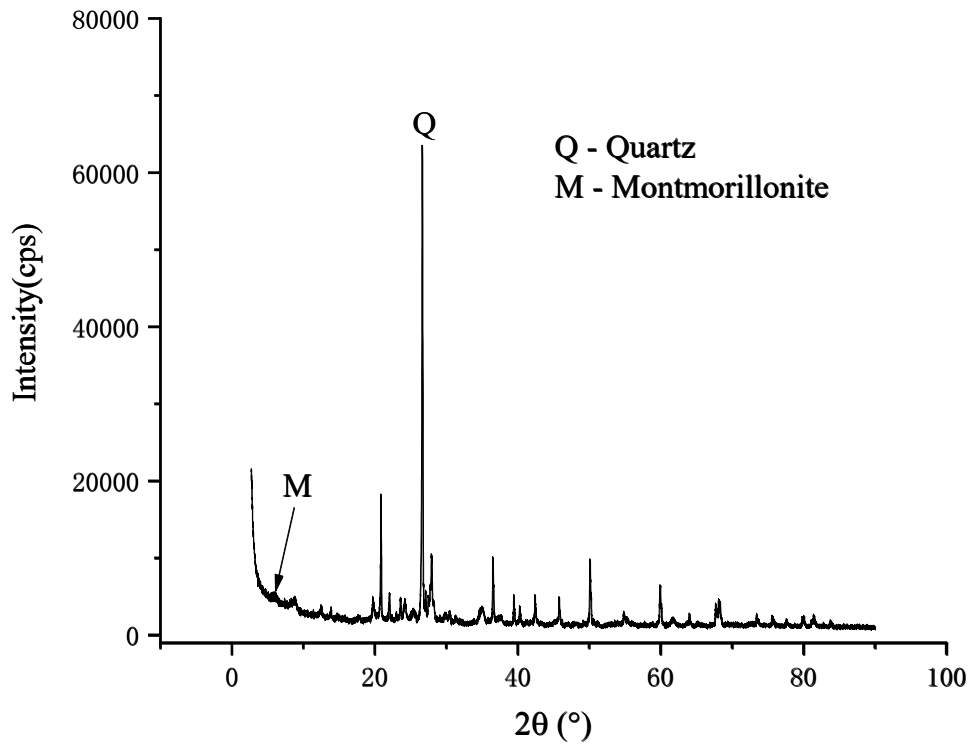


**Figure 2-6 XRD apparatus**



**Figure 2-7 XRD results of Akita mudstone**

As shown in **Figure 2-7**, although the Quartz can be recognized clearly at about  $26.7^\circ$ , the peak of Montmorillonite is not obvious. In order to detect Montmorillonite more clearly, Akita mudstone powder was mixed with water and pass the sieve with the size of  $20\mu\text{m}$ . Finally, some upper suspension was air-dried on the carrier glass for XRD test. As the results shown in **Figure 2-7**, the Montmorillonite peak can be recognized clearly at about  $6^\circ$ . In summary, there are some minerals including Montmorillonite and Quartz in Akita mudstone.



**Figure 2-8 XRD result of Terashima mudstone**

As can be seen in **Figure 2-8**, the Quartz can be recognized clearly at about 26.7° in Terashima mudstone. However, the peak of Montmorillonite is not obvious, and a small peak can be recognized in 6°. This means that the most mineral content in Terashima mudstone is Quartz.

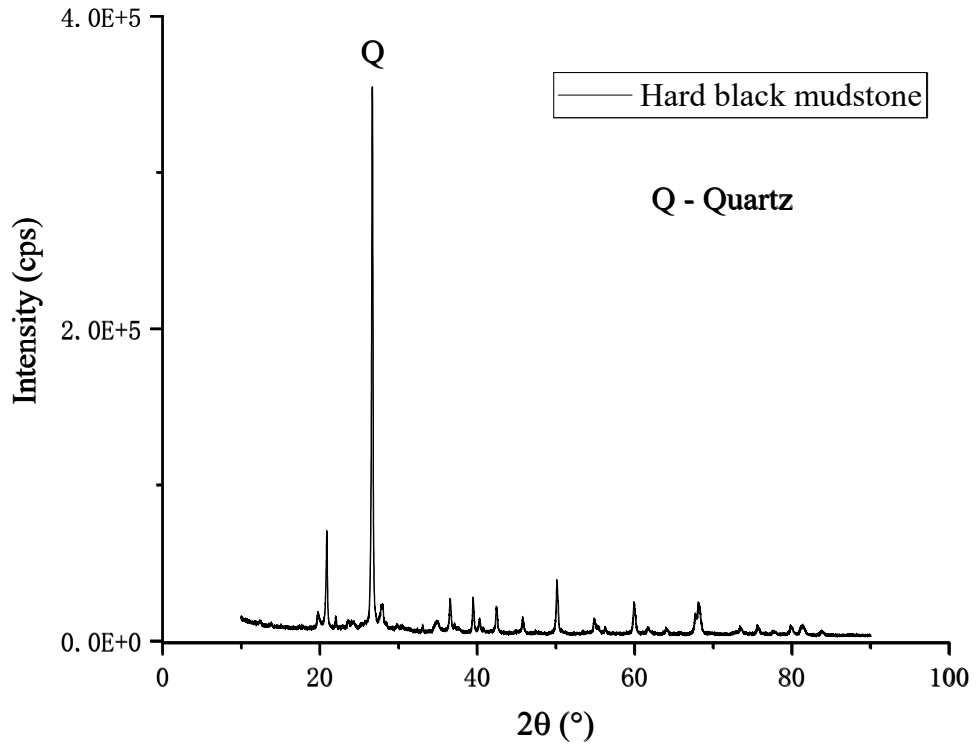


Figure 2-9 XRD result of hard black mudstone

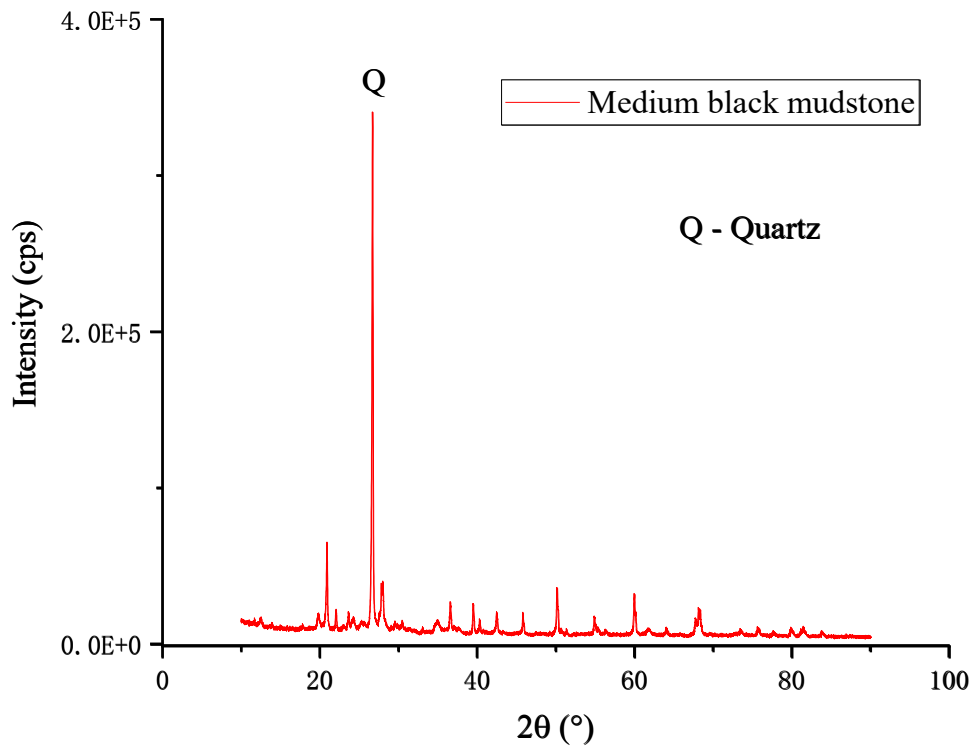
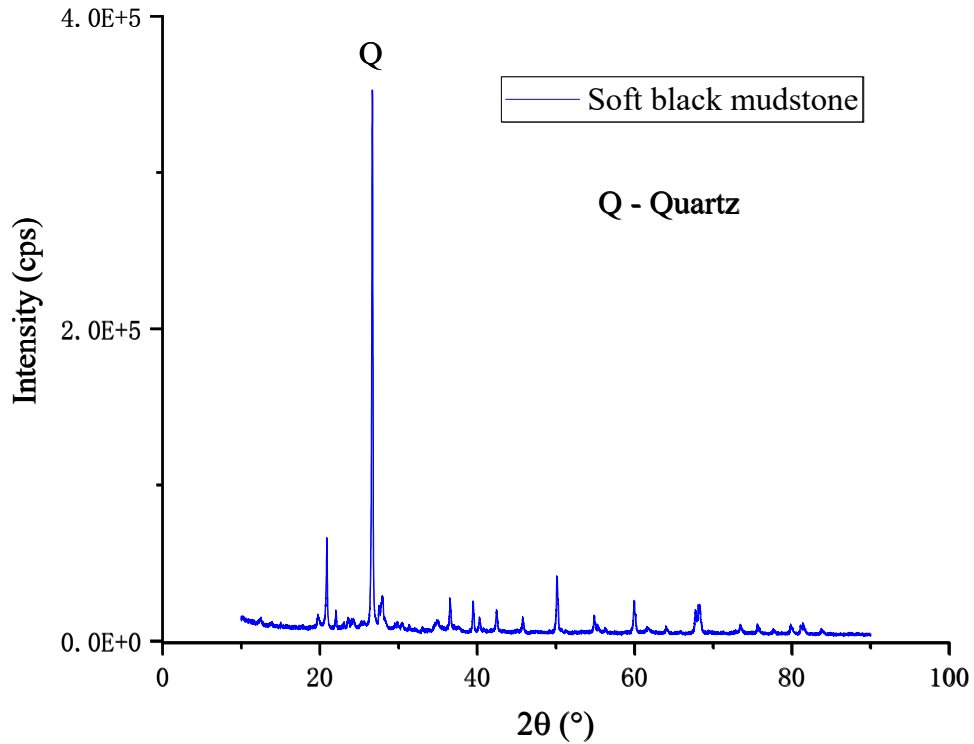


Figure 2-10 XRD result of medium black mudstone





**Figure 2-11 XRD result of soft black mudstone**

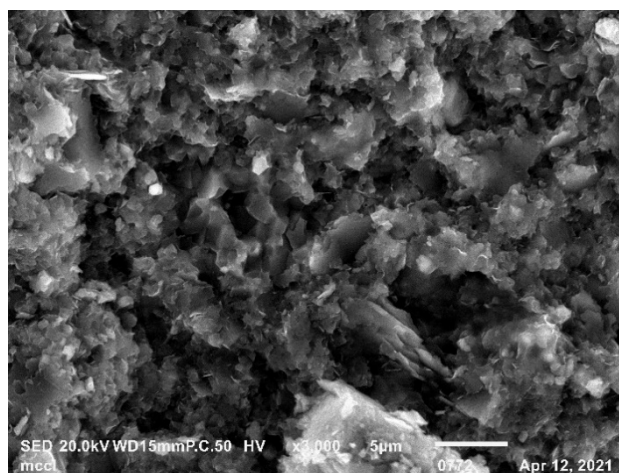
For the three different hardness of black mudstone. There is almost no difference from the point view of XRD results. The most mineral content in this three different hardness of black mudstone is Quartz. This may be because the different hardness of black mudstone is caused by different degrees of weathering, and the difference before and after weathering is difficult to recognized in XRD results. In general, XRD results are consistent with the montmorillonite content in section 2.3.3. The akita mudstone has the most montmorillonite, while Terashima mudstone has a very low amount.

## 2.4 Scanning electron microscope (SEM) tests

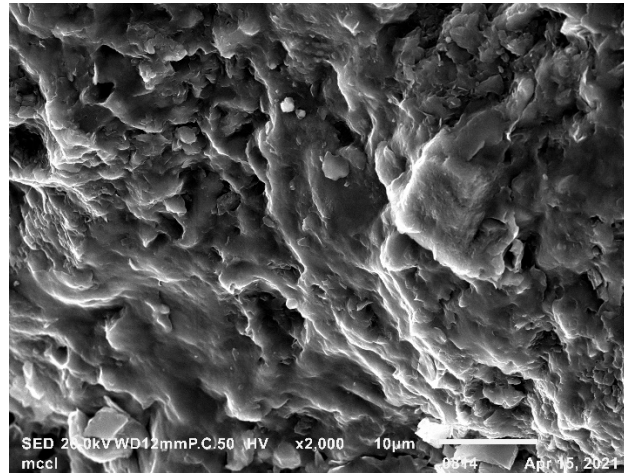


**Figure 2-12 Scanning electron microscope (JEOL JSM-IT100LA)**

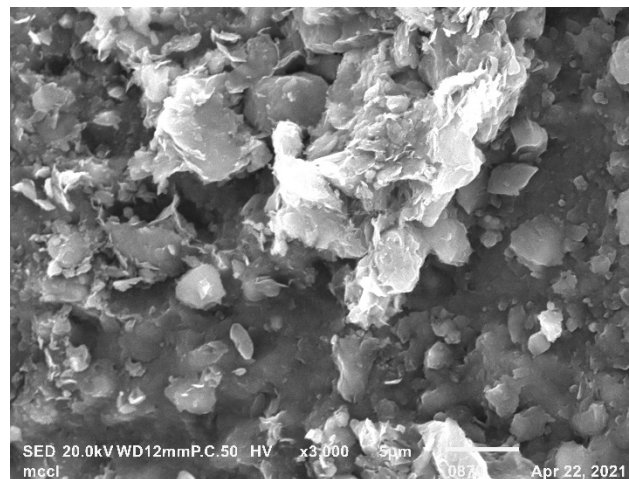
The SEM (IT100) with magnification of  $\times 5 \sim \times 30000$  were used in this study, which can be seen in **Figure 2-12**. The acceleration voltage is in the range of 0.5kV ~ 30kV, and the SEM image consist of 5120 $\times$ 3840 pixels. Before the observation, the specimens are coating to keep electrons from gathering.



**Figure 2-13 SEM image of hard black mudstone**



**Figure 2-14 SEM image of medium black mudstone**



**Figure 2-15 SEM image of soft black mudstone**

In order to study the structure difference of black mudstone with different harness. The SEM images of black mudstone with different harness can be seen from **Figure 2-13** to **Figure 2-15**. For the hard black mudstone, there are some crystals can be seen in **Figure 2-13**, which can usually be observed in hard rock. While some flocs and crystals can be observed in SEM images of medium black mudstone. However, flocs are observed most frequently in soft black mudstone. These three images of black mudstone with different hardness indicate that during the weathering process, the crystallization of mudstone is transformed from crystal to flocculent from the point view of SEM tests.

**Chapter 3. STUDY ON SWELLING STRAIN  
BEHAVIOR OF AKITA MUDSTONE  
WETTED BY NA CL SOLUTION UNDER  
DIFFERENT CONCENTRATION AND  
VERTICAL CONFINING STRESSES**

### 3.1 Testing equipments and procedures

#### 3.1.1 Swelling pressure test

An apparatus (Wang, Komine and Gotoh, 2022) was used for measuring swelling pressure. In this study, two different dry density (1.8 and 2.0 g/cm<sup>3</sup>) of black mudstone and three different dry density (0.9; 1.0 and 1.1 g/cm<sup>3</sup>) of Akita mudstone were used for swelling pressure tests. The details of specimens can be seen in **Table 3-1**. It is noteworthy that a 24-hour wetting is sufficient to saturate the sample and achieve the equilibrium ( $p_{eq}$ ) points of the swelling curve.

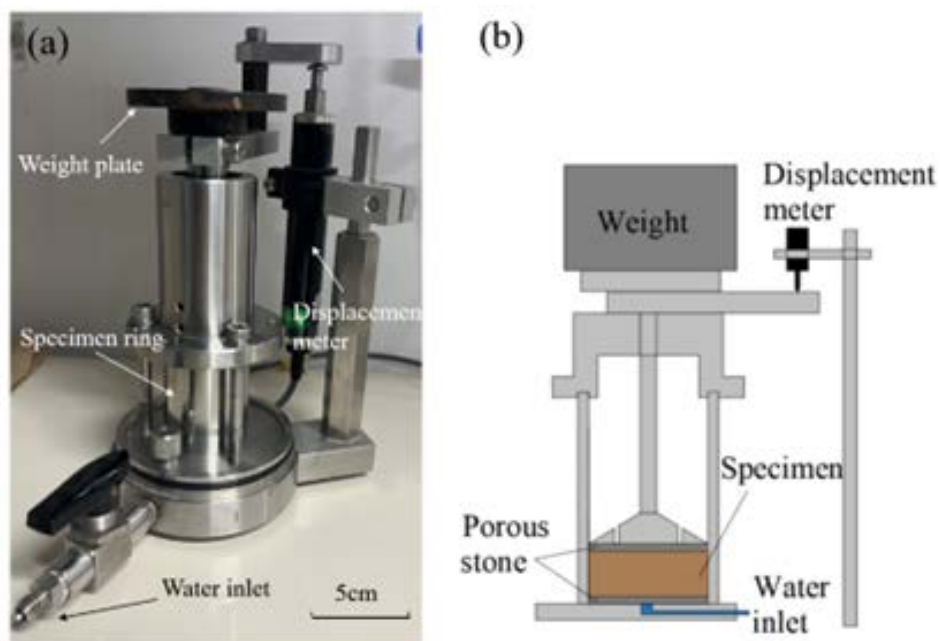
**Table 3-1 Specimens information for swelling pressure tests**

Specimen	Target Dry density (g/cm <sup>3</sup> )	Initial water content (%)	Size (Hight× Diameter)	Wetting duration (h)
Black mudstone	1.8; 2.0	3.2%	~10mm×28m	24
Akita mudstone	0.9; 1.0; 1.1	0%	m	

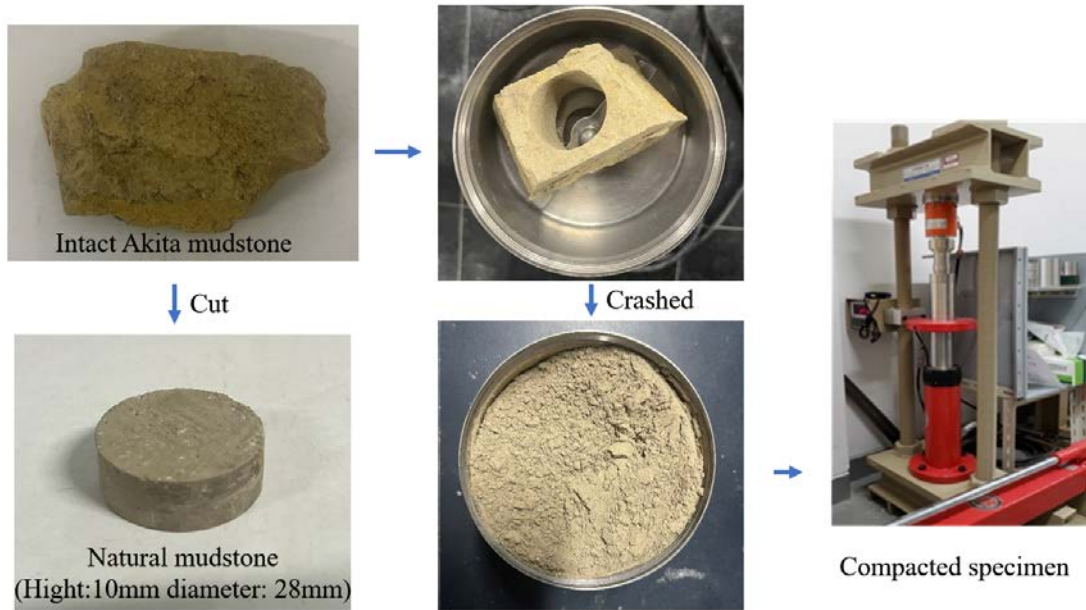
#### 3.1.2 Swelling strain test

In this chapter, Black mudstone, Terashima mudstone and Akita mudstone were used. For each mudstone, several specimens were prepared for the wetting duration of 24 h. The swelling strain apparatus used in this chapter is shown in **Figure 3-1**. Natural and remolded Akita mudstone were used for swelling strain tests. The process of specimen

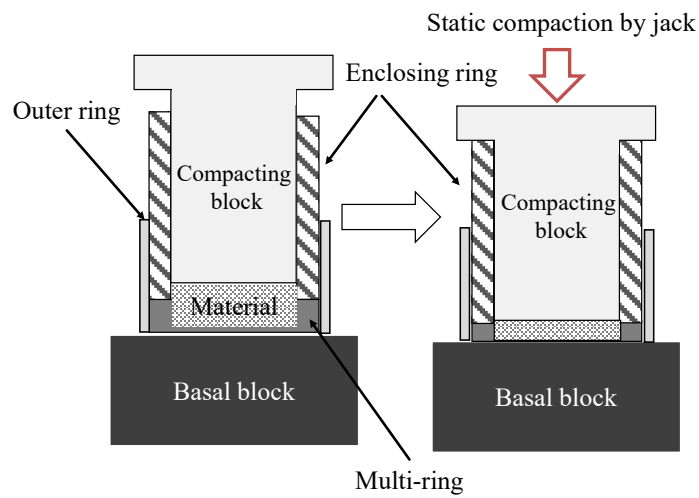
making can be seen in **Figure 3-2**. The sampling ring from a large mudstone block cut the natural Akita mudstone 10 mm high and 28 mm in diameter. The other part of the mudstone block was gathered and crushed into a powder and compacted into remolded specimens of the same size and dry density as the natural one. The static compression device and the compaction process of specimens can be seen in **Figure 3-3**. After that, the swelling strains of these two oven dried specimens were measured using the apparatus shown in Figure 3 under 7.9 kPa and were calculated by dividing the swelling displacement by the initial specimen height. The displacement metre's precision is 0.002 mm and all tests were conducted at room temperature (22 °C). For details about specimen making and the swelling strain apparatus, please refer to Ito and Komine (2020). For other mudstones including black mudstone and Terashima mudstone, only remodeled specimens were used in swelling strain tests.



**Figure 3-1 (a) Photo and (b) schematic diagram of equipments for swelling strain test**



**Figure 3-2 Preparation of natural and remodeled mudstone**



**Figure 3-3 Static compression device**

**Table 3-2 Specimen details for swelling strain test**

Specimen	Target dry density (g/cm <sup>3</sup> )	Initial water content (%)	Size (Hight× Diameter)	Wetting duration (h)
Black mudstone	1.8; 2.0	3.2%	~10mm×28	24
Terashima mudstone	1.7; 1.8; 1.9	0%	mm	

Natural Akita mudstone	1.18	0% (dried by the oven)		
Remodeled Akita mudstone	0.9; 1.0; 1.1; 1.18	0% (dried by the oven)		

For the swelling strain tests, three kinds of mudstones used in this study are shown in **Table 3-2**. The dry densities of black mudstone specimens are 1.8 and 2.0 g/cm<sup>3</sup>. For the Terashima mudstone, three different dry densities (1.7; 1.8 and 1.9 g/cm<sup>3</sup>) were used. For the Akita mudstone, in addition to the undisturbed and remolded samples with a dry density of 1.18 g/cm<sup>3</sup>, three different density (0.9; 1.0 and 1.1 g/cm<sup>3</sup>) remolded specimens were also used in the experiment to investigate the effect of dry density on the swelling strain. It is noteworthy that in all the experiments, the specimens were saturated using distilled water, and a vertical confining stress of 7.9 kPa was applied during the testing process.

**Table 3-3 Akita mudstone specimen details for swelling strain test with different concentration of NaCl solution under vertical confining stress**

Specimen	Target dry density (g/cm <sup>3</sup> )	Stress (kPa)	Different concentration of NaCl solution	Initial water content (%)
Akita mudstone	0.9	7.95	0%;5%; 10%; 15%	0% (dried by the oven)
		15.9	0%;5%; 10%; 15%	
		33.4	0%;5%; 10%; 15%	
	1.0	7.95	0%;5%; 10%; 15%	



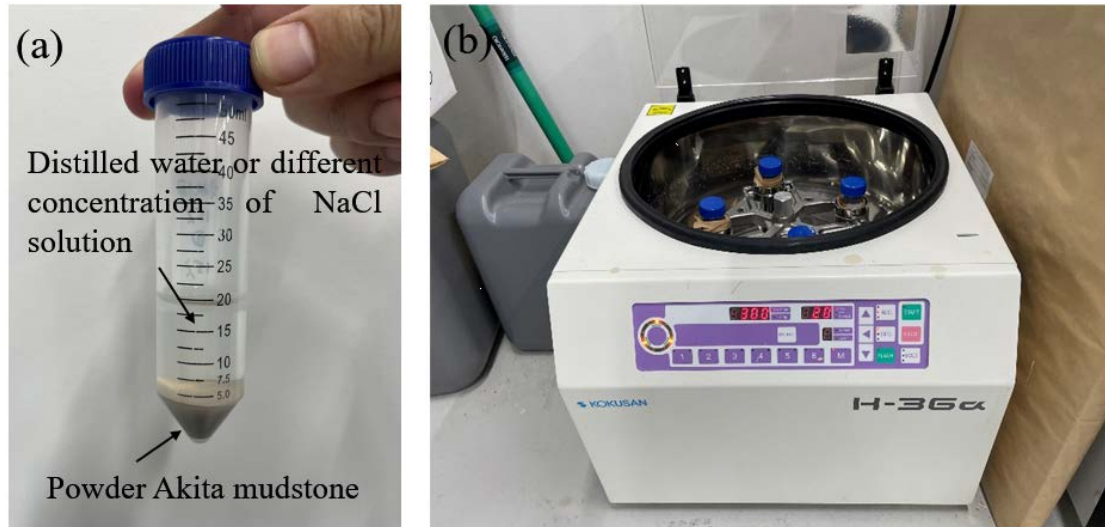
		15.9	0%;5%; 10%; 15%
		33.4	0%;5%; 10%; 15%
	1.1	7.95	0%;5%; 10%; 15%
		15.9	0%;5%; 10%; 15%
		33.4	0%;5%; 10%; 15%

The Akita mudstone powder was compacted into specimens with 10 mm high and 28 mm in diameter for swelling strain tests. The swelling strains of these specimens with different dry density range from 0.9 - 1.1 g/cm<sup>3</sup> were also measured using the apparatus shown in **Figure 3-1** under different vertical confining stress (7.95; 15.90 and 33.40kPa). Except for distilled water, different concentrations (5%; 10% and 15%) of sodium chloride solutions was also used in this study to explore the influence of Na<sup>+</sup> on swelling behavior of Akita mudstone. The swelling strain was calculated by dividing the swelling displacement by the initial specimen height. The details of testing program can be seen in **Table 3-3**.

### 3.1.3 Leaching testing of Akita mudstone with distilled water or NaCl solutions

To investigate the chemical reaction of sodium chloride solution with Akita mudstone, the concentration of Ca<sup>+</sup> and Mg<sup>+</sup> of leach liquor from Akita mudstone with different concentration of sodium chloride solution were measured. 10g of Akita mudstone powder was mixed with 20ml of distilled water or different concentration of sodium chloride solution (5%; 10% and 15%). The details of specimen can be seen in **Figure 3-4a**. And after 24 hours of standing and 10min of centrifugation (see **Figure 3-4b**),

some ion concentration of the supernatant was measured using ion analyzer (IA-300) as shown in **Figure 3-5**.



**Figure 3-4 (a) Mixture of Akita mudstone with distilled water and different concentration of NaCl solution and (b) centrifugation device**

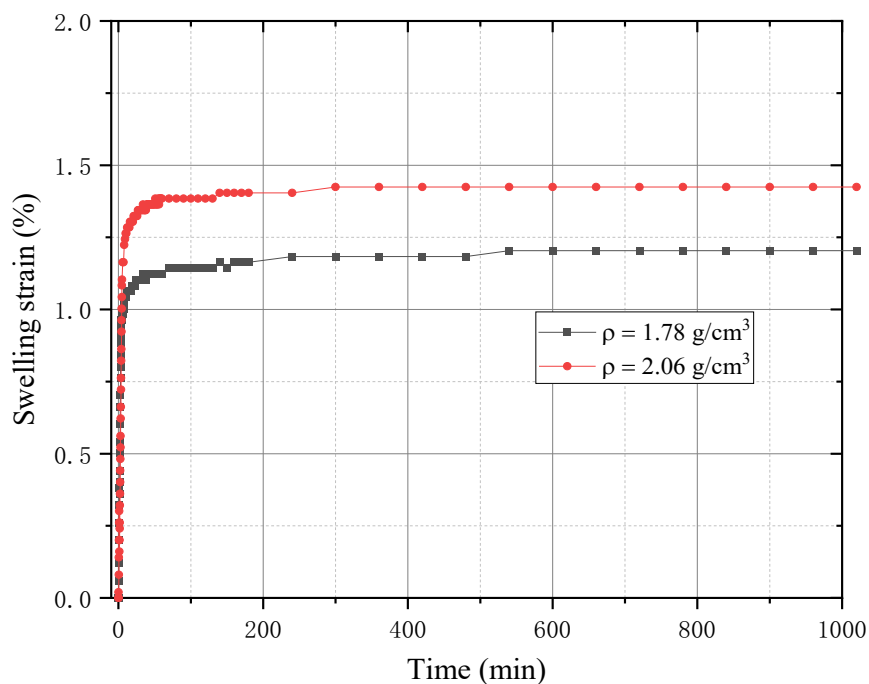


**Figure 3-5 Ion analyzer (IA-300)**

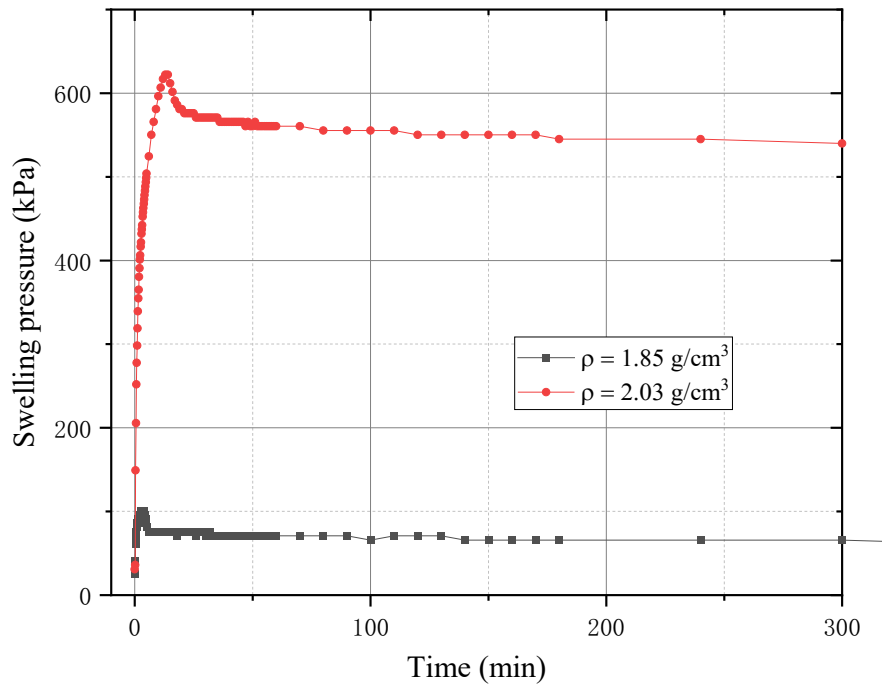
## 3.2 Results and discussion

### 3.2.1 Swelling pressure and strain of black mudstone

**Figure 3-6** presents the changes of swelling strains with saturation time for the black mudstone with dry densities of 1.78 and 2.06 g/cm<sup>3</sup>. With 7.9kPa of vertical confine stress, the swelling strain increases from 1.2% to 1.4% as the dry density increases from 1.78 to 2.06 g/cm<sup>3</sup>. However, the swelling strain of the black shale remains relatively low, within 1.5%. Therefore, in terms of swelling strain, the black mudstone has almost no swelling property. On the other hand, the evolution of swelling pressure with the dry density can be seen in **Figure 3-7**. As the dry density increases from 1.85 to 2.03 g/cm<sup>3</sup>, the swelling pressure of the black mudstone also increases sharply, rising from 80 kPa to 570 kPa. This indicates that the increase in dry density can significantly enhance the swelling pressure of the black mudstone. In general, the increase in dry density can significantly enhance the swelling pressure of black mudstone, while having little effect on the swelling strain of black mudstone.

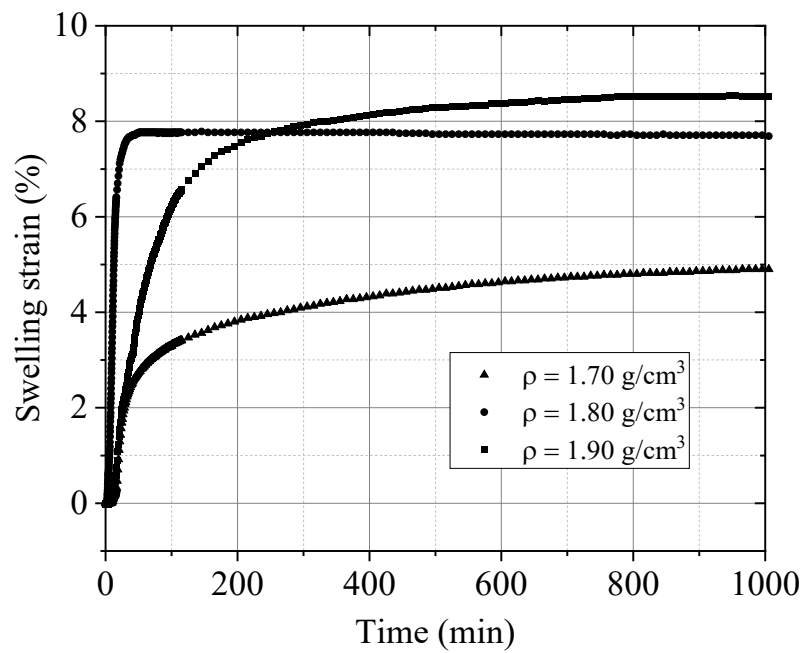


**Figure 3-6 Swelling strain evolution curves of remodeled black mudstones with different dry densities**



**Figure 3-7 Swelling pressure evolution curves of remodeled black mudstone with different dry densities**

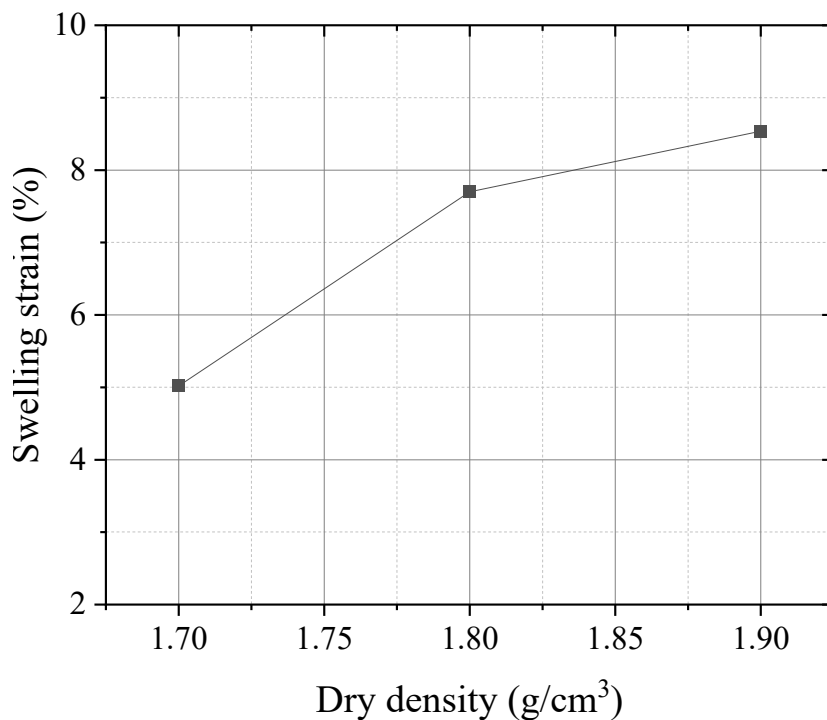
3.2.2 Swelling strain of Terashima mudstone



**Figure 3-8 Swelling strain evolution curves of remodeled Terashima mudstones**

**with different dry densities**

**Figure 3-8** presents the changes of swelling strains with saturation time for the Terashima mudstone with dry densities from 1.70 to 1.90 g/cm<sup>3</sup>. As the dry density increases from 1.70 to 1.80 g/cm<sup>3</sup> and further to 1.90 g/cm<sup>3</sup>, the swelling strain of the Terashima mudstone also increases, rising from 4.9% to 7.7% and finally reaching 8.5% at a dry density of 1.90 g/cm<sup>3</sup>. This indicates that the increase in dry density can significantly enhance the swelling strain of the Terashima mudstone. In terms of swelling strain, the Terashima mudstone exhibits some swelling characteristics. And the swelling strains range from 4-9% in this study.



**Figure 3-9 The evolution of final swelling strains with dry densities**

The relationship between final swelling strain and dry density is shown in **Figure 3-9**, which indicates that the swelling strain increases with increasing dry density (from 1.70 to 1.80 g/cm<sup>3</sup>). However, as the dry density continues to increase, the increase in swelling strain becomes smaller, increasing by less than 1%. This may be due to the

higher dry density resulting in the soil more compact, thus restraining the swelling strain.

### 3.2.3 Swelling strain and pressure of Akita mudstone

Swelling strain evolution curves of remodeled Akita mudstones are shown in **Figure 3-10**. As the dry density increased from 0.88 to 0.97 g/cm<sup>3</sup>, and then to 1.11 g/cm<sup>3</sup>, the swelling rate of Akita mudstone also increased, from 2.05% to 4.96%, and eventually reached 10.99% at a dry density of 1.11 g/cm<sup>3</sup>. This indicates that an increase in dry density can increase the swelling rate of Akita mudstone. From the perspective of swelling rate, Akita mudstone exhibits certain swelling characteristics. And furthermore, the swelling strain reached a stable stage and remained constant within a short period of time (approximately 200 minutes). In order to investigate the relationship between the dry density and final swelling strain of the Akita mudstone, the final swelling strains of Akita mudstone with different dry densities were collected and summarized in **Figure 3-11**. It can be observed that the swelling strain increases continuously with the increase in dry density. Furthermore, there exists a linear relationship between dry density and final swelling strain, as shown by the dashed line in **Figure 3-11**.

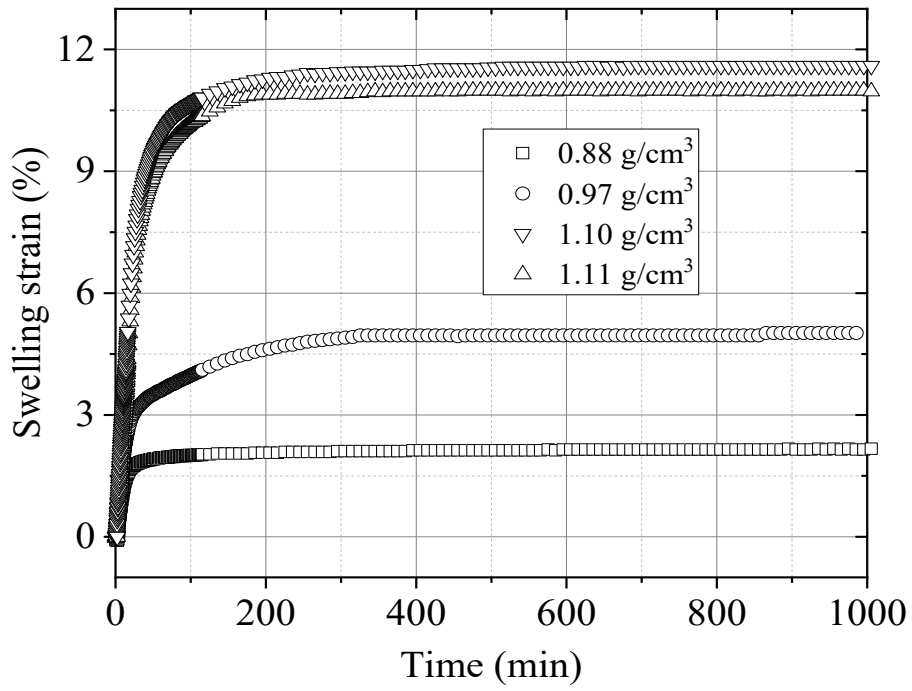


Figure 3-10 Swelling strain evolution curves of remodeled Akita mudstones with different dry densities

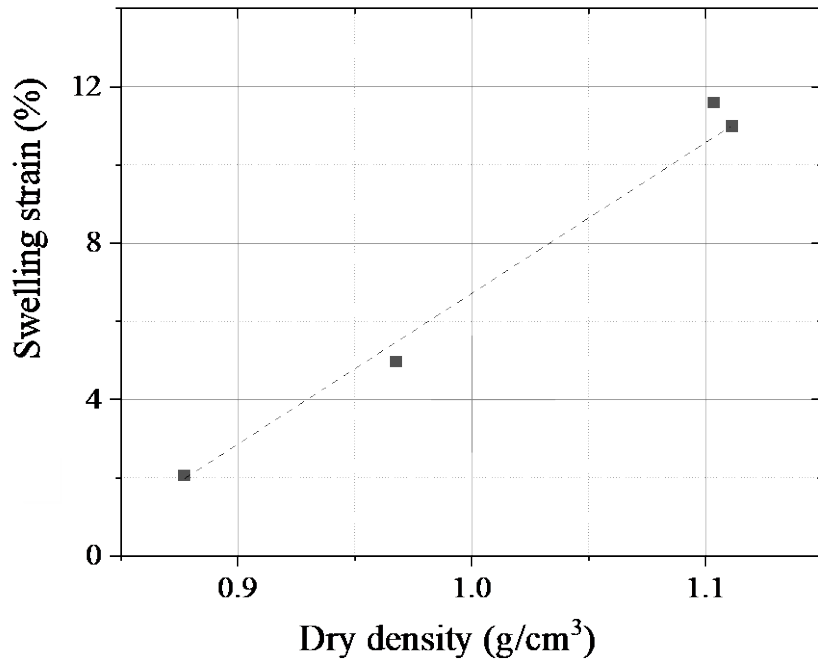
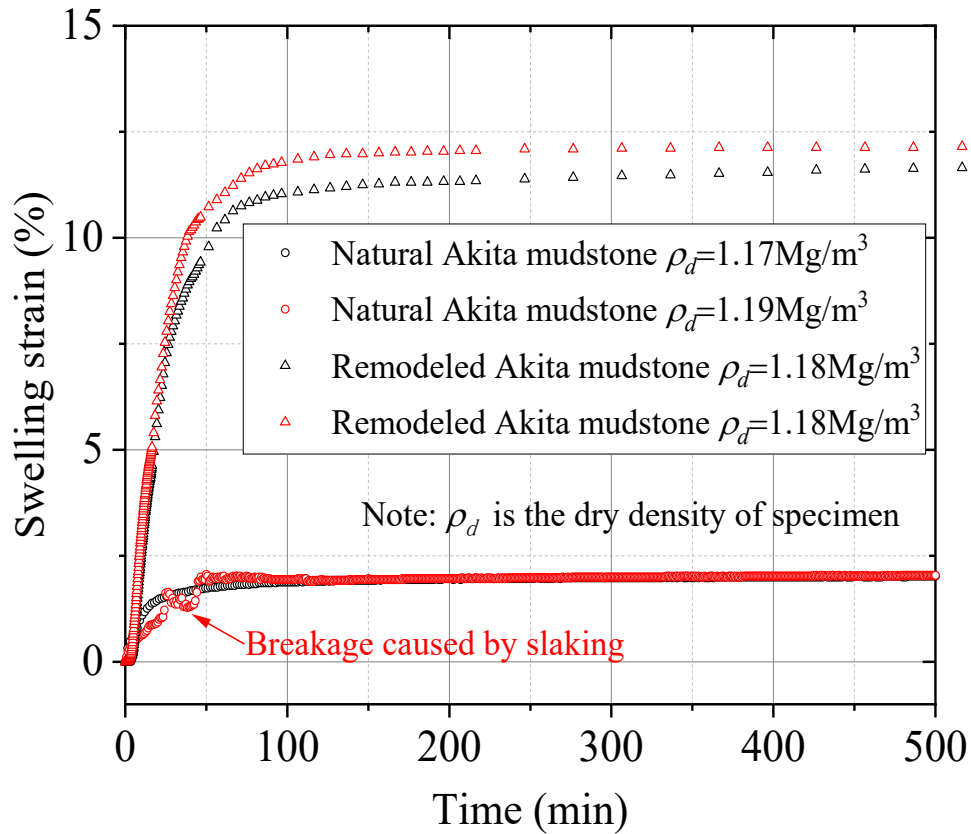


Figure 3-11 The evolution of final swelling strains with dry densities



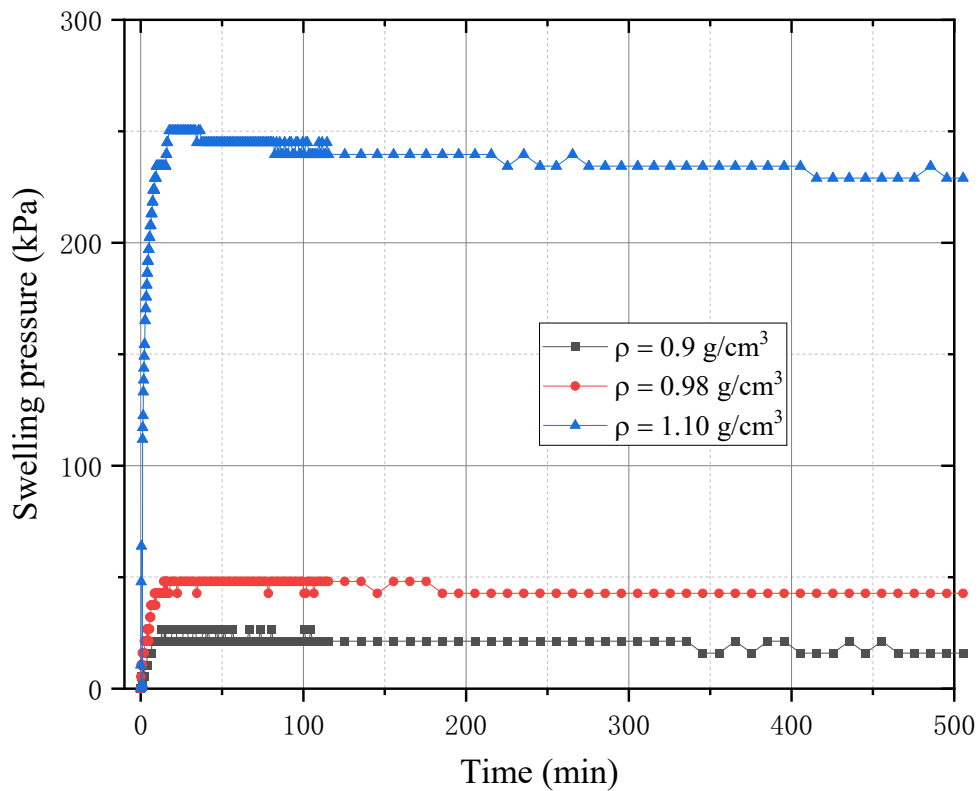
**Figure 3-12 Swelling strains of natural and remolded Akita mudstone**

The swelling strain tests were conducted on natural Akita mudstone and remolded under 7.9 kPa; **Figure 3-12** shows the results. The swelling strains of natural and remolded Akita mudstone increase and maintain a constant value in the wetting process. The final swelling strains of natural mudstone with dry densities of 1.17 Mg/m<sup>3</sup> and 1.19 Mg/m<sup>3</sup> are approximately 2%. Due to the slaking behavior, the swelling curve of natural Akita mudstone (1.19 Mg/m<sup>3</sup>) fluctuates during the increase. The breakage of specimen due to the slaking slightly decreases the curve. However, the other natural mudstone shows no slaking behavior, resulting in a constant increase during the wetting process. The swelling strains of remolded Akita mudstone (1.18 Mg/m<sup>3</sup>) are higher than those of natural ones and reach approximately 12%.

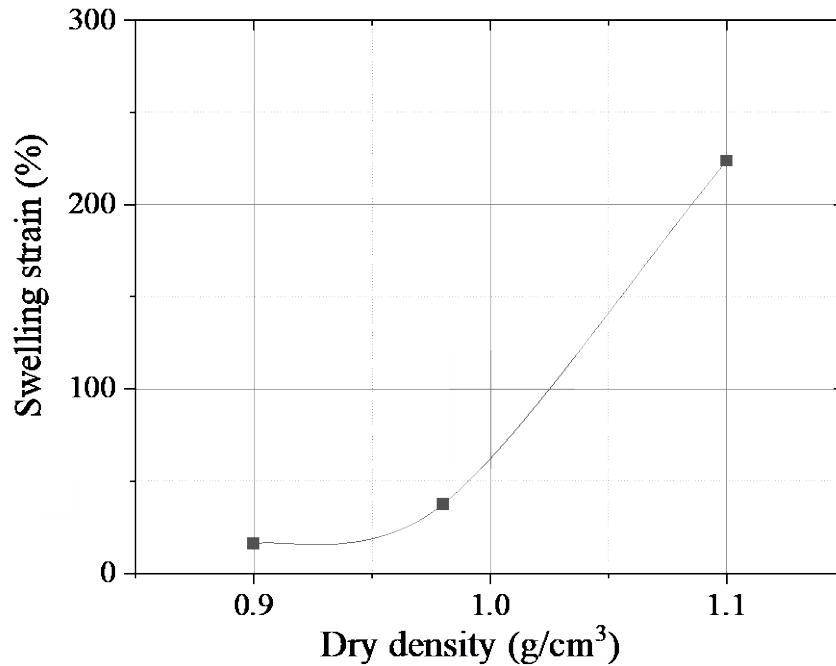
As mentioned in the introduction section, there are three reasons for slaking: (1) the air-breakage phenomenon, (2) differential swelling and (3) the dissolution of cement agents.



The swelling behavior of mudstone might cause the slaking behavior. **Figure 3-12** indicates that the structure of natural mudstone confines the soil's swelling behavior, resulting in a lower swelling strain in the natural Akita mudstone. During cyclic drying and wetting, the repeated swelling stress might destroy the natural mudstone's structure, resulting in slaking behavior. This conclusion will support the analysis in chapter 5.



**Figure 3-13 Swelling pressure evolution curves of remodeled Akita mudstones with different dry densities**

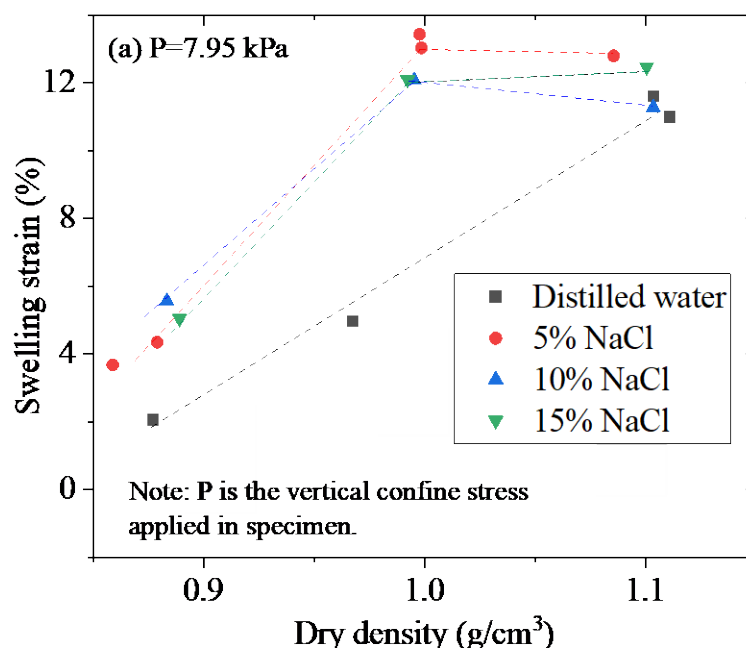


**Figure 3-14** The evolution of final swelling pressures of Akita mudstone with dry densities

Swelling pressure evolution curves of remodeled Akita mudstones are shown in **Figure 3-13**. As the dry density increased from 0.90 to 0.98 and then to 1.10, the swelling pressure also increased from 16 kPa to 37 kPa, and finally reached 224 kPa at a dry density of 1.10. From **Figure 3-14**, it can be observed that the swelling pressure increases continuously with the increase in dry density. This indicates that an increase in dry density can significantly increase the swelling pressure of Akita mudstone, with a greater increase in swelling pressure observed at higher dry density levels. However, the swelling pressure of Akita mudstone remained low, below 300 kPa, regardless of the dry density.

### 3.2.4 Swelling strain of Akita mudstone with different concentration of NaCl solution and different pressure

The evolution of final swelling strain with dry densities under different vertical confine stress is shown in Figure 3-15. Under the vertical confine stress of 7.95 kPa, the swelling strain of the sample increased with increasing dry density. However, for the specimens saturated with sodium chloride solution, the swelling strain reached 12% at a dry density of 1.0 g/cm<sup>3</sup> and remained constant thereafter as the dry density increased (see **Figure 3-15a**). However, as the vertical confinement stress increased (15.9 kPa and 33.4 kPa), the swelling strain decreased relative to the low-stress condition. As the dry density increased from 0.9 to 1.1 g/cm<sup>3</sup>, the swelling strain increased from 1.5% and -0.6% to 8.0% and 5.0%, respectively. This indicates that the swelling strain gradually decreases with the increase of vertical stress. In addition, except for the case of low vertical stress (7.95 kPa) and saturated samples with distilled water, the swelling strain in other experimental results increases linearly with the increase of dry density.



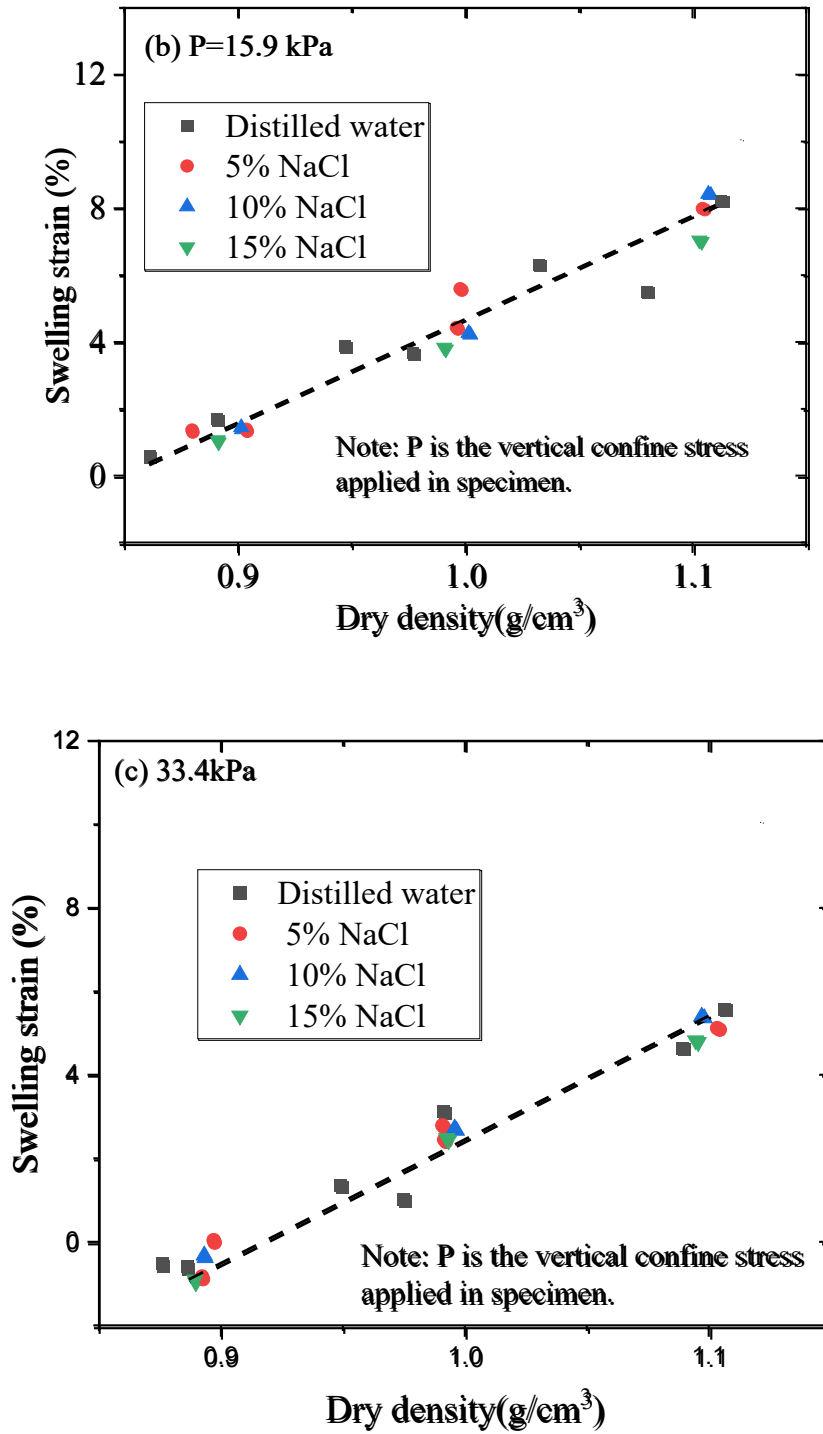
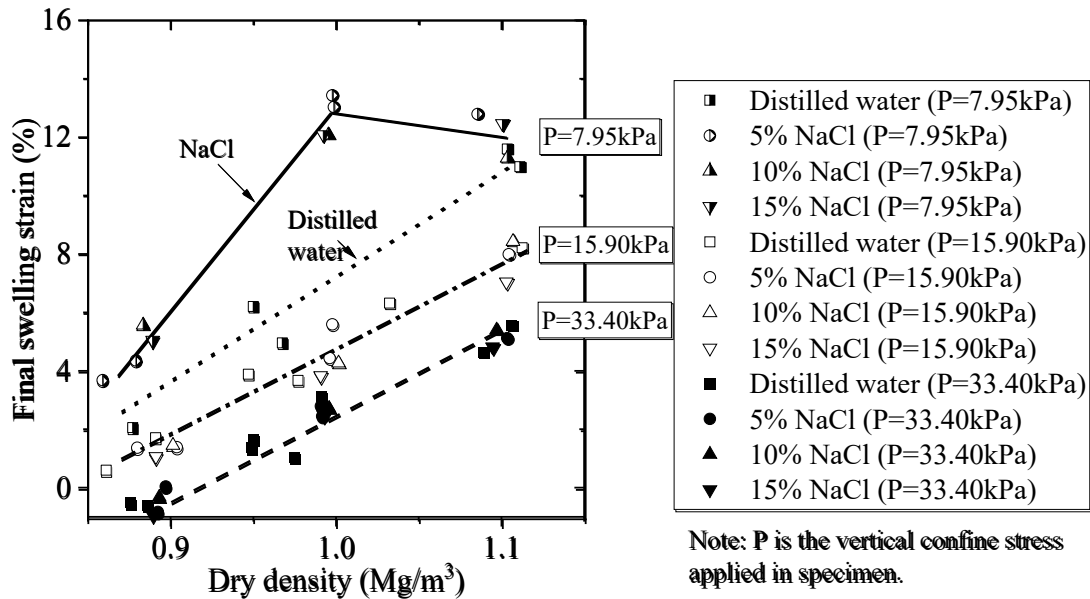


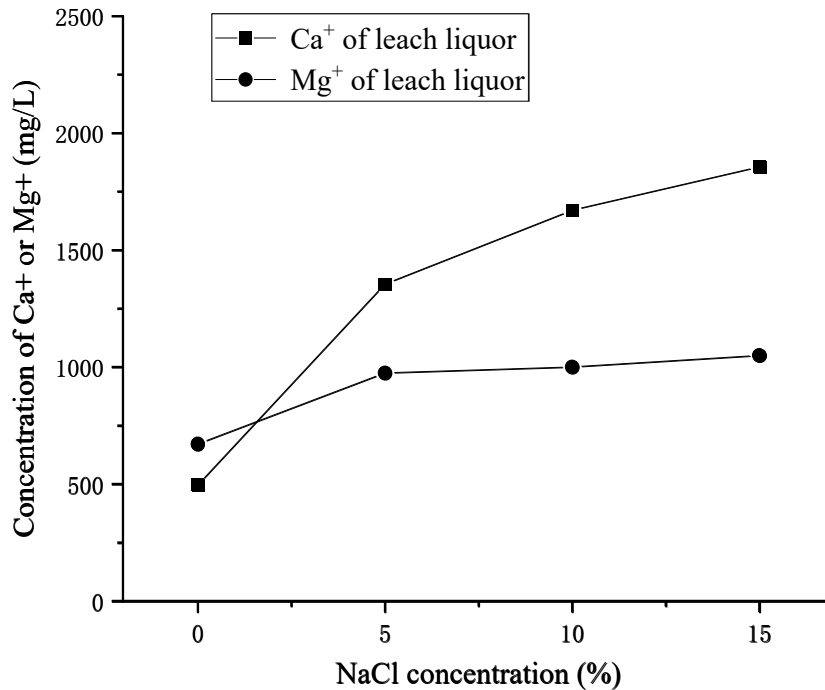
Figure 3-15 The evolution of final swelling strain with dry densities under different vertical confine stress



**Figure 3-16 Swelling strain of Akita mudstone with different concentration of NaCl solution and different vertical confine stresses**

The results of swelling strain of Akita mudstone with different concentration of NaCl solution and different vertical confining stress were summarized in **Figure 3-16**. It is worth noting that in order to facilitate the comparison of the swelling strains under different vertical confining stress and Na<sup>+</sup> concentrations, **Figure 3-16** only shows the final swelling strains of Akita mudstone. In general, the swelling strains increase with increasing dry density. Meanwhile, the swelling strains gradually decrease with increasing vertical confining stress from 7.95kPa to 33.40kPa. For the stress of 7.95kPa, the swelling strains of specimens in distilled water is lower than that in sodium chloride solution, especially when the dry density is around 1.0 g/cm<sup>3</sup>. However, for larger stress (15.90kPa and 33.40kPa), the difference of swelling strains of specimens in distilled water and sodium chloride solution is invisible.

### 3.2.5 Swelling strain and pressure of Akita mudstone



**Figure 3-17 The leached Ca<sup>+</sup> and Mg<sup>+</sup> concentration from supernatants**

The leaching testing results, when Akita powder was mixed with distilled water or NaCl solutions, were summarized in **Figure 3-17**. As the concentration of sodium ions increases, the concentrations of leached calcium and magnesium ions in the supernatant gradually increase from 496 to 1856mg/L and 671 to 1050mg/L respectively, indicating that the Ca<sup>+</sup> and Mg<sup>+</sup> ions in mudstone were exchanged by Na<sup>+</sup> ions in the solution. These two testing results indicate that, under vertical confining stress of 7.95 kPa, the final swelling strain of the specimens wetted by NaCl solutions can be larger than that of distilled water because of relative larger swelling potential of Na type montmorillonite than Ca type. However, this difference may be eliminated by applying larger confining

stress (15.90kPa and 33.40kPa) and larger dry density, since the swelling potential can be counterbalanced by the confining or inter friction.

#### Conclusion

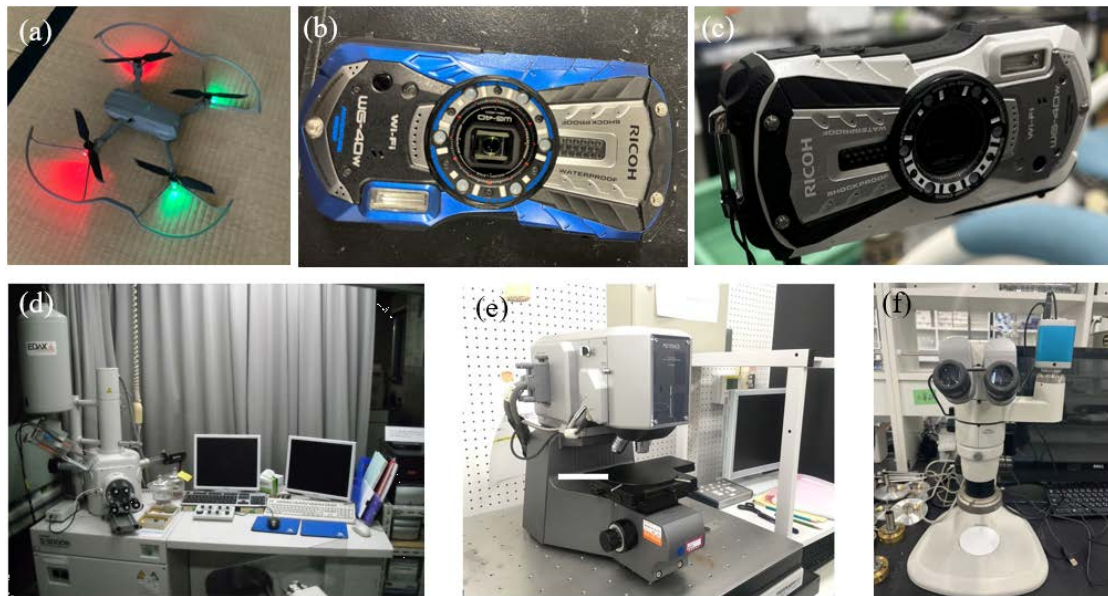
The swelling strain and pressure of black mudstone are both within a relatively low range, which may be attributed to its low content of montmorillonite. On the other hand, although Terashima mudstone also has low content of montmorillonite, its swelling strain is much greater than that of black mudstone. This suggests that there may be other minerals in Terashima mudstone that contribute to its larger swelling strain. Swelling strains of Akita mudstone decrease with the increase of vertical stress and increase with the increase of dry density. With different concentration of sodium chloride solution, the swelling strains increase due to the conversion of some calcium-based montmorillonite into sodium-based montmorillonite under low stress and this increase can be compacted by applying stress. On the other hand, the  $\text{Ca}^+$  and  $\text{Mg}^+$  ions in Akita mudstone were leached out by  $\text{Na}^+$  ions in the solution, which support the conclusion.

**Chapter 4. THE IMPROVEMENT AND  
APPLICATION OF MUTI-VIEW APPROACH**




## 4.1 Testing overview

The devices used in this chapter can be seen in **Figure 4-1**. And configuration features of devices can be seen in **Table 4-1**. For large scale (Teishi island), the videos of the island were taken by a drone (**Figure 4-1a**) and the images of island from different perspectives were extracted from the videos. These images were used for multi-view approach. For medium scale (Akita mudstone specimen), two methods were used to obtaining the 3D models for comparing with each other. One is multi-view approach by camera and the other method is CT test. Cameras (see **Figure 4-1b** and c) with two common resolutions (3024×4032 pixels and 1920×1080 pixels) were also used in a standard Cuboid (14.90×63.67×123.72 mm) for investigating the influence of image resolutions in the results. For small scale (Akita mudstone particles and Mikawa sand V7), one optical microscope (**Figure 4-1f**) and was used for Akita mudstone particles to obtain 3D models by multi-view approach. Meanwhile, Scanning Electron Microscope (**Figure 4-1d**) was used to obtain the images for multi-view approach from one Mikawa sand and laser scanning microscope (**Figure 4-1e**) was also used in the Mikawa sand to obtain the surface area to compare the result obtained from multi-view approach.



**Figure 4-1 Devices used in this study: (a) Drone; (b) High resolution Camera; (c) Low resolution Camera; (d) Scanning Electron Microscope; (e) Laser scanning microscope; (f) Optical microscope**

**Table 4-1 Configuration features of devices used in this study**

Area or specimen	Devices name	Features	Details
 Teishi island	Drone	Place of origin	China
		Type of device	DJI Mavic Air 2
		Max Flight Time	34 minutes
		Max Flight Distance	18.5km
		Camera	1/2" CMOS; 48MP
		ISO Range	100-6400
		Video Resolution	4K/60fps
		Max Video Bitrate	120Mbps
	Computed Tomography	Place of origin	Japan
		Type of device	NAOMI-CT 3D-L
		Tube voltage	50 - 100kV



Akita mudstone specimen

Tube current	2 - 10mA
Resolution of image	2208 × 1792 pixels
Pixel size	120um
Minimum scanning interval	0.166mm



Cuboid

Low resolution Camera	Place of origin	Japan
	Type of device	RICOH WG-40W
	Iso	125 - 6400
	Focal length	28 - 140mm
	Maximum aperture	F3.5
	Resolution of image	1920 × 1080 pixels

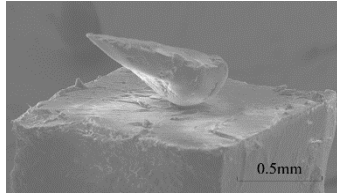
High resolution Camera	Place of origin	Japan
	Type of device	RICOH WG-40W
	Iso	125 - 6400kV
	Focal length	28 - 140mm
	Maximum aperture	F3.5
	Resolution of image	3840 x 2160 pixels



Akita mudstone particles

Optical microscope	Place of origin	Japan
	Type of device	Nikon SMZ800
	Eyepieces	10x C-W A/22
	Zoom Range:	1.0 - 6.3
	Total Magnification	10 - 63
	Resolution of image	1920 × 1080 pixels

Place of origin	Japan
-----------------	-------



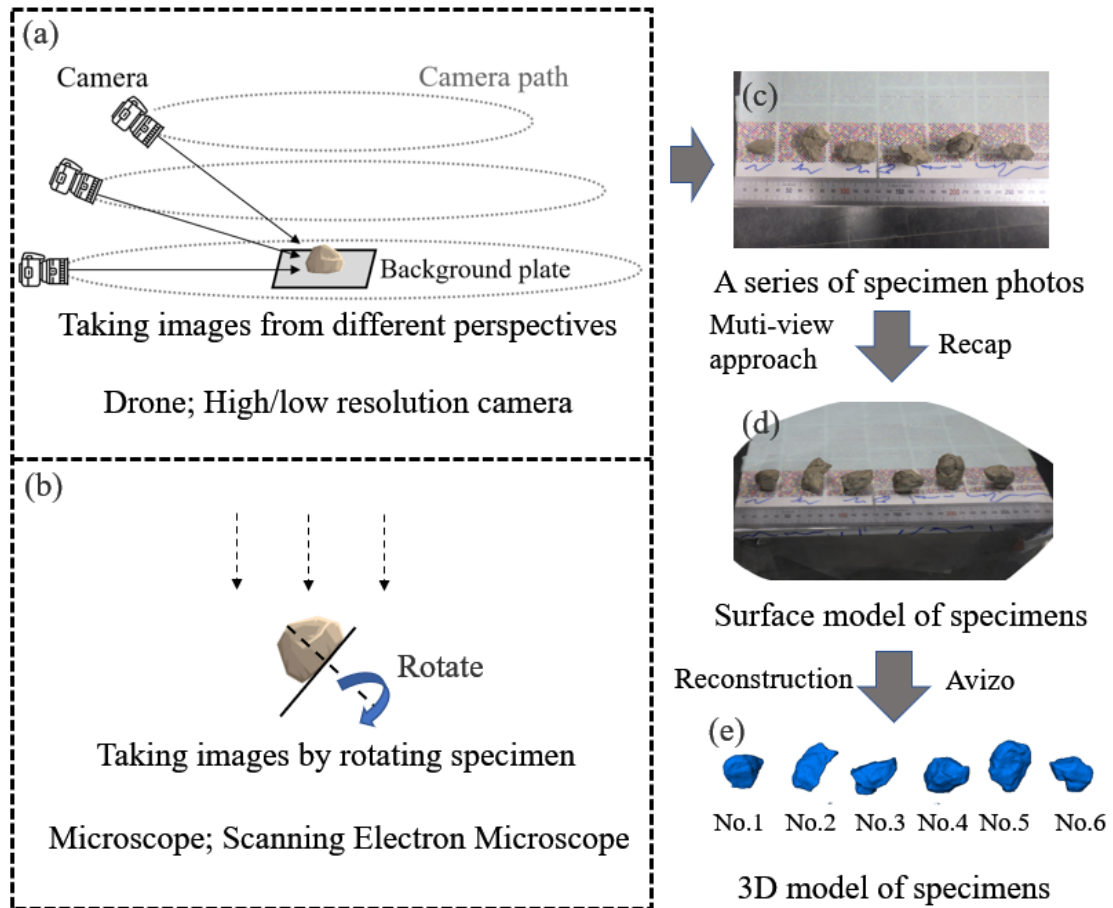
Mikawa sand V7

Laser scanning Microscope	Type of device	KEYENCE VK9510
	Objective Magnification	10, 20, 50, 150
	Height measurement	7mm
	Laser source	
	Wavelength	408nm
	Maximum power	0.9mW
	Horizontal resolution	0.13um
Scanning Electron Microscope	Place of origin	Japan
	Type of device	S3000N
	Magnification	20 - 30000
	Acceleration voltage	0.5 - 30kV
	Vacuum	
	high vacuum	≤1Pa
	low vacuum	6 - 270Pa
	Resolution of image	1280 × 960 pixels

NOTE: CMOS: Complementary Metal Oxide Semiconductor

The process of multi-view approach is shown in **Figure 4-2**. The specimens are placed on background plate with different colored blocks (**Figure 4-2c**). These color blocks are helpful in the process of point-matching during image process, which can improve the accuracy and success rate of synthesizing 3D models. And the improvement of background plate in multi-view approach will be discussed in section 4.2.2. Specimens are fixed on the background plate by tapes. It is worth noting that the obtained 3D model is a whole of specimens and background plate. In later image process, the model will be cut in the joint area to separate specimens and background plate. Thus, there are two

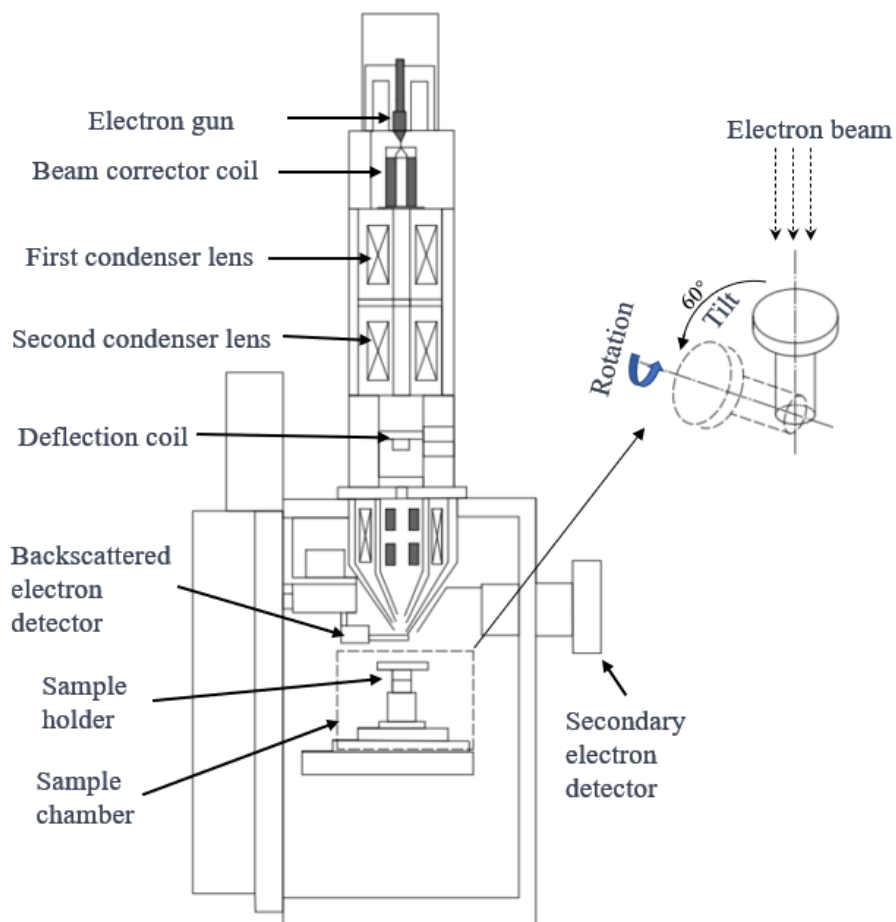
principles for reduce the influence of joint area when fixing the specimens by tapes: (1) The plane part of the specimens is used as the contact surface with the background plate; (2) Using the sharp part of the specimens to contact the background plate to reduce the area of joint area.



**Figure 4-2 Multi-view approach process**

In order to obtain a 3D model, a series of 2D images should be obtained by taking photos of the specimens from different perspectives by camera or microscope. During the photo taking process, the camera takes photos along the camera path as shown in **Figure 4-2a** and 80-100 images were obtained. These images were synthesized into a 3D surface model by Recap - one software for synthesizing 3D surface model by multi-

view approach. However, volume cannot be measured from surface models directly. Thus, surface models are filled by voxels to establish 3D model by 3D analysis software - Avizo. After that, some key shape parameters including surface area and volume are calculated by the 3D model of specimens. On the other hand, the method of obtaining specimen photos from different perspectives by moving the lens is impossible in microscopes and SEM tests. Therefore, for small-scale specimens, we use the method shown in **Figure 4-2b**, which rotates the sample to achieve different angle shots. As for the details of taking photos using SEM, shown in **Figure 4-3**, the sample holder is rotated and tilted to obtain photos for the multi-view approach.




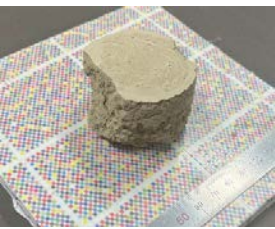
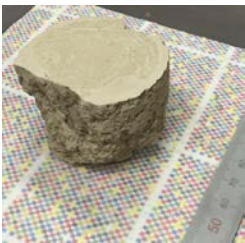
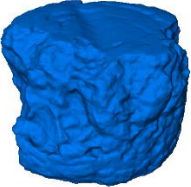


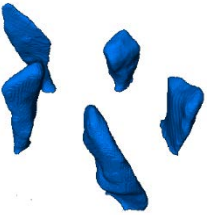
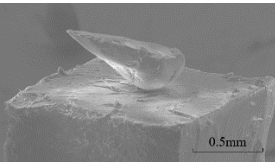
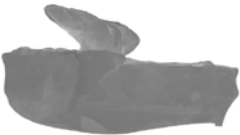
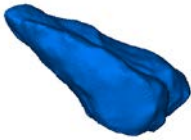


**Figure 4-3 Images obtained from SEM for multi-view approach**

## 4.2 Results and discussion

### 4.2.1 Application of multi-view approach on different scales

**Table 4-2 Results of multi-view approach in different scales**

Specimens	Original images	Surface model (Recap)	3D model (Avizo)
Teishi island (scale: 100m)			
Akita mudstone specimen (scale: 0.1m)			
Akita mudstone particles (scale: 1mm)			
Mikawa sand V7 (scale: 100 um)			

Results of multi-view approach in different scales are shown in **Table 4-2**. The multi-view method is widely used for large-scale models, as demonstrated in this study where the details of Teishi Island (scale: 100m) are fully displayed. However, vegetation on the island is connected to the main body, which is also observed in other study (Vanneschi *et al.*, 2019). In other scale ranges (from 0.1 m to 100 um), models obtained by using cameras, microscopes, and scanning electron microscopes to take photos can also present the shape of the specimens. This

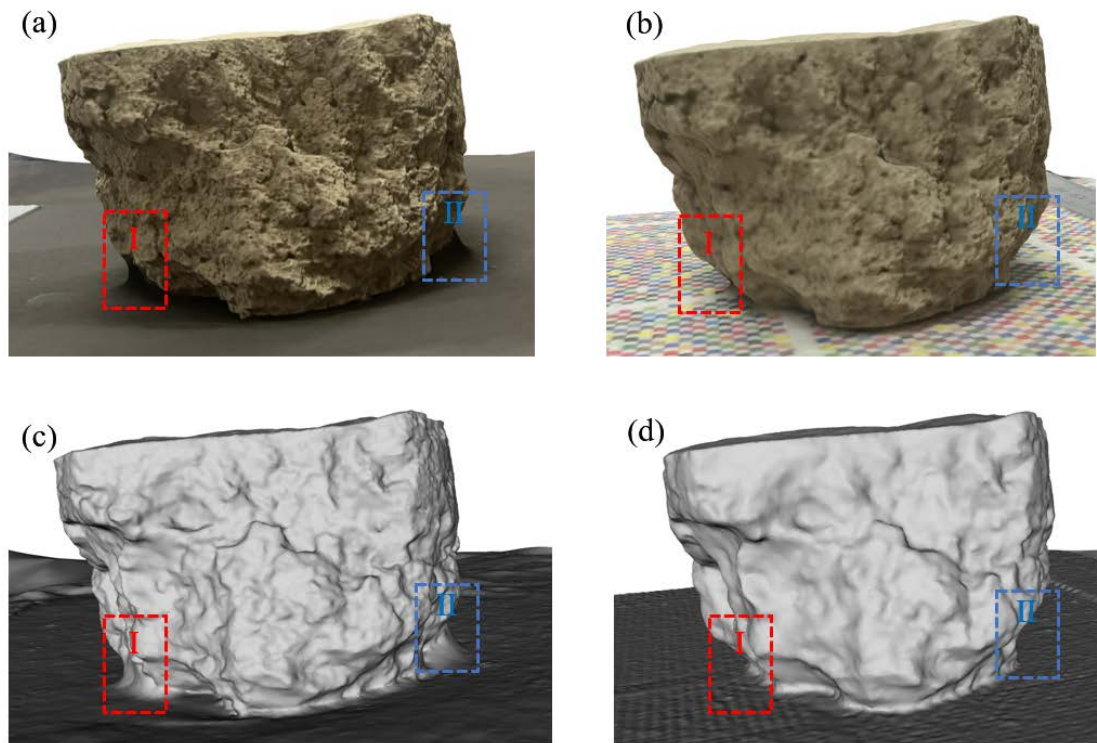
demonstrates the feasibility of this method at different scales: according to the principle of the multi-view method, as long as photos from different perspectives of the object can be obtained, the surface model can be reconstructed, and then the shape parameters of the object, including volume, surface area, and surface roughness, can be extracted by the model.

#### 4.2.2 Improvement of multi-view approach

As mentioned in section 4.1, the background plate can improve the results obtained from multi-view approach. This is because the background plate with different colored blocks is helpful in the process of point-matching during image process. **Figure 4-4** shows details of 3D structure obtained by multi-view approach with or without background plate. **Figure 4-4a** is the 3D model of the specimens without the background plate. And the connection between the specimen and black plate has a prominent black area (area I and II in **Figure 4-4a**). However, for the specimen on the colored plate, the structure details of connection between the specimen and black plate are pretty good (area I and II in **Figure 4-4b**). Moreover, the surface models in **Figure 4-4c** and **d** can show this difference of details more clearly. The results indicated that using colored plates significantly improves the accuracy of the model, especially at the connection between the specimen and the plate. There are some unrealistic protrusions



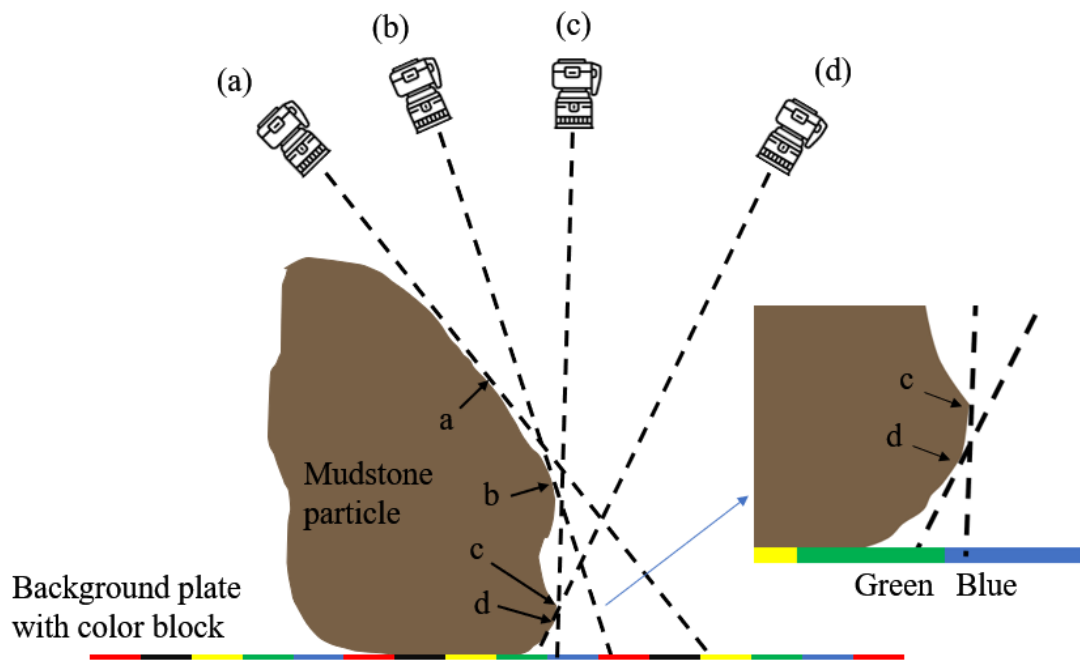
without colored plates. However, colored plates can better represent the shape of the specimen in this connection area.



**Figure 4-4 3D structure obtained by multi-view approach with or without background plate**

The mechanism of improvement of multi-view approach using colored plate is illustrated in **Figure 4-5**. Generally, based on the principle of multi-view method, the concave parts of an object's surface are difficult to accurately monitor due to the lack of sufficient reference points to determine their depth (Tafti *et al.*, 2015). However, in the case of using a colored plate, the concave portions of the region in contact with the plate and the specimen can be accurately marked by the different color blocks on the chart. As shown in **Figure 4-5**, when the camera is positioned at points c and d, the points c and d on the surface of the sample can be located by the different color blocks

(green and blue) in the image, thereby obtaining detailed surface information of the concave portion in the contact area between the sample and the plate. This ultimately leads to the ability to reveal the details of the concave portions of the specimen using a color chart, as demonstrated in **Figure 4-4b** and **d**.

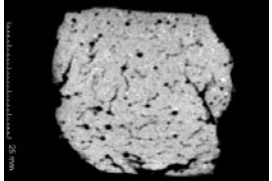
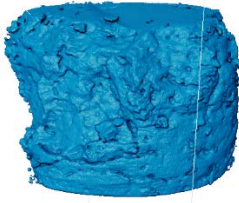



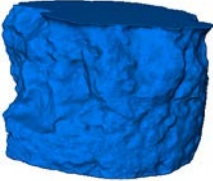
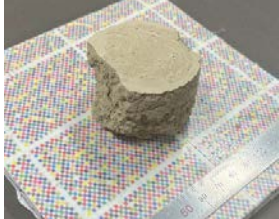
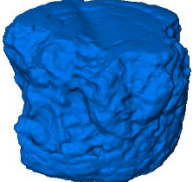
**Figure 4-5 The improvement of multi-view approach using colored plate**

To validate the improvement, the results obtained using multi-view stereo with and without a color chart were summarized in **Table 4-3** and compared with the results obtained using CT. It is worth noting that, in order to compare the results, a low-resolution camera (1920×1080) will be used in multi-view approach, regardless of whether the model has a color palette or not. Compared to the multi-view method, CT image is able to show internal cracks and pores of the specimen. In order to make a comparison with the multi-view method, the 3D model of the CT result shown in the table is the result obtained after filling in the internal cracks and pores. And the apparent

volume of the CT result was obtained with the internal pores filled. Comparing the results of the apparent volume and surface area extracted from different methods (multi-view approach and CT method) reveals that the differences between the results are small, but the CT model contains more details. In this study, it is assumed that the CT results are accurate, and therefore, the volume error and surface area error are calculated by dividing the difference between the parameters obtained from two methods by the parameters obtained by the CT method. The volume and surface area calculated without a colored plate are larger than those calculated by the model with a colored plate. The contact area between the specimen and the plate will be misidentified without using a color plate, resulting in an overestimation of the volume due to the extra volume caused by the misidentified area, which leads to a larger volume without a colored plate compared to the volume with a colored plate. It can be observed that after using the color chart, the error of surface area decreased from 4.7% to 2.1%. Although there is almost no change in volume error after using the color chart, undoubtedly, the volume obtained after using the color chart is more accurate according to the details shown in **Figure 4-4**.

**Table 4-3 Results of using multi-view approach with or without colored plate and CT scanner**

Specimen	Method	3D model	Volume	Surface area
Akita mudstone specimen (scale: 0.1m)	 CT method		12617 mm <sup>3</sup>	63855 mm <sup>3</sup>

 <p>Muti-view approach without background plate</p>		<p>12972 mm<sup>3</sup> (error: 2.8%)</p>	<p>66845 mm<sup>2</sup> (error: 4.7%)</p>
 <p>Muti-view approach with background plate</p>		<p>12295 mm<sup>3</sup> (error: 2.6%)</p>	<p>65194 mm<sup>2</sup> (error: 2.1%)</p>






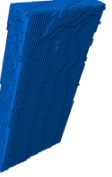
#### 4.2.3 The accuracy of the muti-view approach

In the process of reconstruction (see **Figure 4-2d** and **e**), the amount of voxels is necessary for filling the surface model should be determined. In theory, the more voxels lead to better accurate 3D model. However, a large number of voxels cause the model file size to grow dramatically. Thus, a balance between accuracy and model file size must be determined in this study. The shape parameter results of cuboid obtained from software with different resolution and the actual parameter calculated by measuring are shown in **Table 4-4**. The error is calculated by dividing the absolute value of the difference between the parameters obtained from the 3D model and the actual parameters. As can be seen from **Table 4-4**, the volume and surface area error are 0.02%~0.05% and 3.32%~4.24% in the case of high-resolution camera (3024×4032 pixels). The error ranges of volume and surface area are within 0.03% and 0.92% respectively under different reconstruction resolution. For low-resolution camera (1920×1080

pixels), the volume error is 0.14%~0.16%, which is larger than the high-resolution one. This is because the accuracy of the 3D model depends on the resolution of the 2D images: The higher the resolution of the 2D images, the more accurate the 3D model. The volume error by low-resolution camera changes in 0.02% under different reconstruction resolution. The surface error for low-resolution camera is similar to that for high-resolution cameras, between 3.41% and 4.16%. It is worth noting that the surface area of both high-precision and low-precision cameras decreases with the reduction of reconstruction resolution. This is because the low-resolution reconstruction cannot restore the rough surface enough (see **Figure 4-6**), which ultimately leads to the reduction of surface area. Overall, higher camera resolution and higher reconstruction resolution can slightly improve the accuracy of 3d models, with all error of results within 5%.

**Table 4-4 Results of parameters extracted from cuboid model with different camera resolution and reconstruction resolutions**

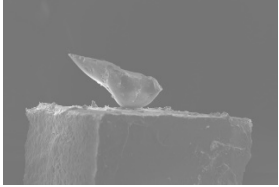

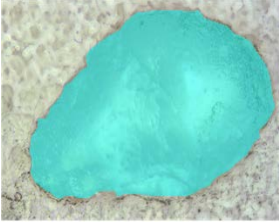
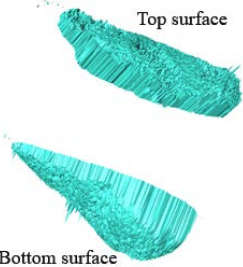
Reconstruction resolution	Camera resolution: 3024×4032 pixels		Camera resolution: 1920×1080 pixels	
	Volume (mm <sup>3</sup> )	Surface area (mm <sup>2</sup> )	Volume (mm <sup>3</sup> )	Surface area (mm <sup>2</sup> )
0.1mm	117427.2	20629.8	117203.3	20610.8
0.5mm	117443.1	20575.6	117185.8	20539.1
1mm	117352.2	20433.2	117205.1	20450.0
Actual parameter	117371.1	21338.7	117371.1	21338.7
Error	0.02%~0.05%	3.32%~4.24%	0.14%~0.16%	3.41%~4.16%

3D model						
Reconstruction resolution:	0.1mm	0.5mm	1mm	0.1mm	0.5mm	1mm
Camera resolution:	High-resolution camera (3024×4032 pixels)			low-resolution camera (1920×1080 pixels)		

**Figure 4-6 3D models of cuboid with different reconstruction resolutions and different camera resolutions**

Results of multi-view approach and laser microscope for one Mikawa V7 sand are shown in **Table 4-5**. The three-dimensional models and parameters obtained from scanning electron microscopy (SEM) and laser scanning microscopy (LSM) are summarized in Table 4. SEM images of the sample from different angles were obtained and then synthesized into a three-dimensional model using a multi-angle approach. LSM was used to obtain both the surface models and surface area of the sand. It is noteworthy that the surface area of one side of the sample can be directly measured using LSM, and the total surface area is obtained by adding the surface area of two sides. The 3D models obtained from LSM in **Table 4-5** is for reference only. The results show that surface area error of two methods is 16.1%. Comparing the error values in **Table 4-3** and **Table 4-4**, the error value in SEM and LSM is relatively large. However, it should be noted that the method of measuring the surface area by laser scanning microscopy involves scanning both sides of the object, and therefore, its accuracy is not as high as that of CT (**Table 4-3**) or direct calculation (**Table 4-4**) methods. Therefore, the multi-view approach can be applied by SEM images, and the result's accuracy has somewhat reliability.

**Table 4-5 Results of multi-view approach and laser microscope for one sand**

Specimen	Method	3D model	Volume	Surface area
Mikawa sand (V7)	 Multi-view approach		0.1103 mm <sup>3</sup>	1.5449 mm <sup>2</sup>
	 Laser scanning microscope		-	1.7937 mm <sup>3</sup>
Error	-	-	-	16.1%

**Conclusion**

Compared to the CT method, multi-view approach cannot observe the internal structure of the specimen. However, this method can be applied to specimens of different scales, and the accuracy of the obtained model increases with higher resolution of images. Based on the mechanism of the multi-view approach, this chapter proposes an improved multi-view method that can optimize the accuracy of the model at the contact between the specimen and the specimen plate. The results of the measured parameters also confirm this. In addition, the multi-view approach can be applied using SEM images, but its accuracy needs to be further studied.

**Chapter 5. STUDY ON SLAKING**

**MECHANISMS OF A MUDSTONE BY**

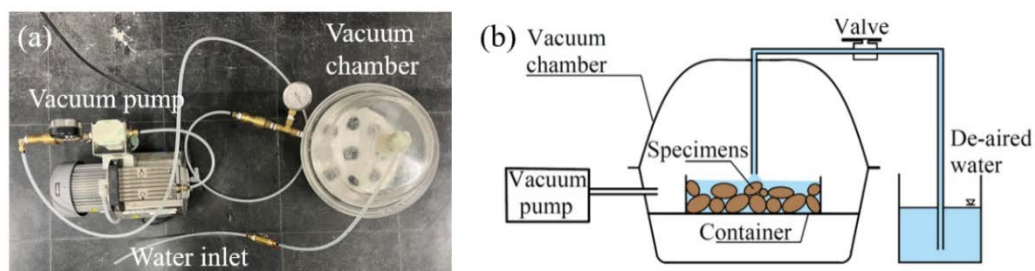
**THREE-DIMENSIONAL SHAPE ANALYSIS**

**USING THE MUTI-VIEW APPROACH**

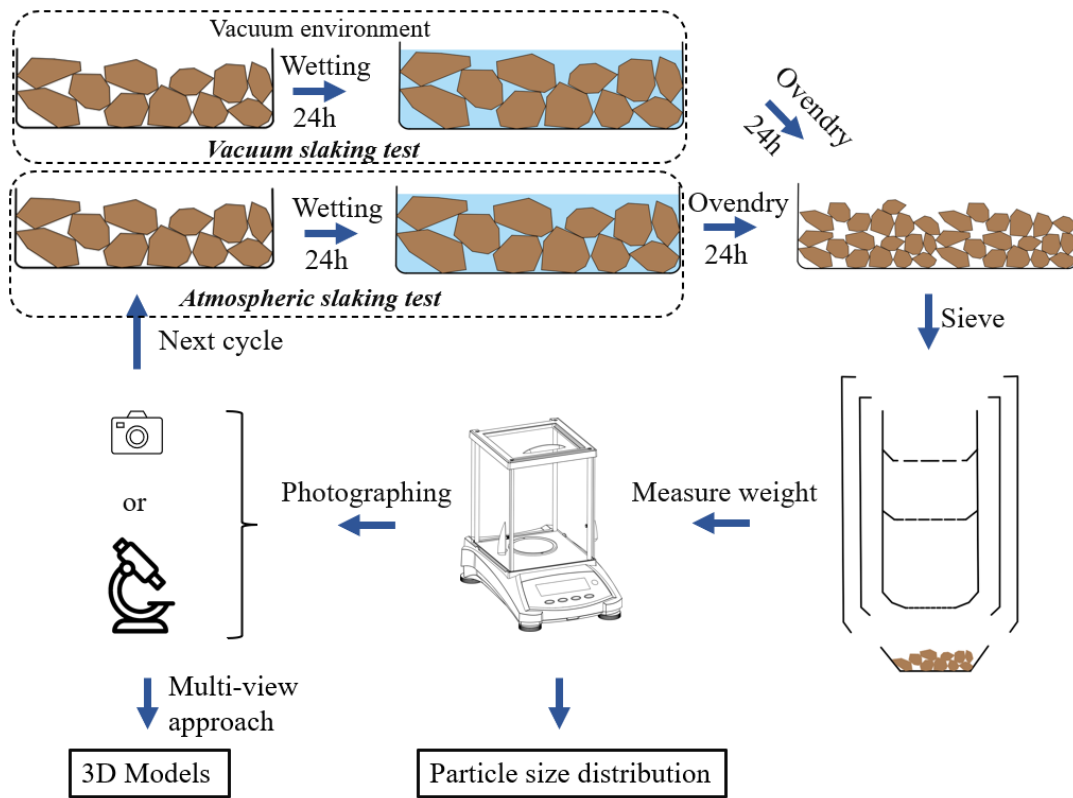


## 5.1 Testing overview

Several dried specimens with a total weight of 740g were used for cyclic drying-wetting tests. These specimens with similar size and shape are divided into two groups of about 370g each, one for atmospheric cyclic drying-wetting test and the other one for vacuum cyclic drying-wetting test. As can be seen in **Figure 5-1**, a vacuum chamber and pump is used to create a vacuum environment during the wetting process of cyclic drying-wetting test. The process of cyclic drying and wetting slaking tests can be seen in **Figure 5-2**. The specimen was first placed in the vacuum chamber and negative pressure of about -98kPa was applied for 10 minutes. Then, the valve was open to inject de-aired water to the specimen container for wetting the process for 24 h at constant room temperature (22°C). Then, the specimen was oven dried at 110°C for another 24 h, after which the specimen was sieved with mesh sizes of 19, 9.5, 4.75, 2.00, 0.85 and 0.25 mm. Different from the vacuum slaking tests, the atmospheric one (Sakai & Nakano, 2019; Su et al., 2020) is wetting in the atmosphere for 24 h at constant room temperature (22°C). And the subsequent experimental procedures were the same with the vacuum one. As the last step of a wetting-drying cycle, photos were taken for particles with different size by the camera (see **Figure 4-1c**) with the resolution of 1920×1080 pixels and Nikon SMZ800 Microscope (see **Figure 4-1f**) with the same resolution. These images are used for obtaining 3D models by multi-view approach.



**Figure 5-1 (a) Photo and (b) diagram of equipment for the vacuum slaking test**



**Figure 5-2 Process of atmospheric and vacuum cyclic drying-wetting test**

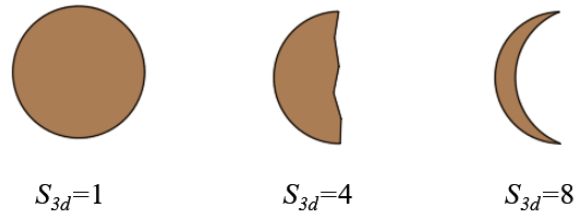
After obtaining the 3D models of specimens by multi-view approach, the key shape parameter called Shape-3d ( $S_{3d}$ ) is calculated by the 3D model of specimens.  $S_{3d}$  is a normalized value indicating the size of surface area of one particle (see **Figure 5-3**). It is calculated by Eqn. 1 and for a sphere, it equals 1.

$$S_{3d} = \frac{A_{3d}^3}{V_{3d}^2} \times \frac{1}{36\pi} \quad (5-1)$$

where  $A_{3d}$  is the surface area of one specimen;  $V_{3d}$  is the volume of the one specimen.

In this study, 80 - 100 images were taken by camera (particle size larger than 0.85mm) and microscope (particle size smaller than 0.85mm) for synthesizing one 3D model (see surface model of specimens in **Figure 4-2d**). It is worth noting that for small size particles, 20 - 40 particles in each size interval were sampled by the method based on

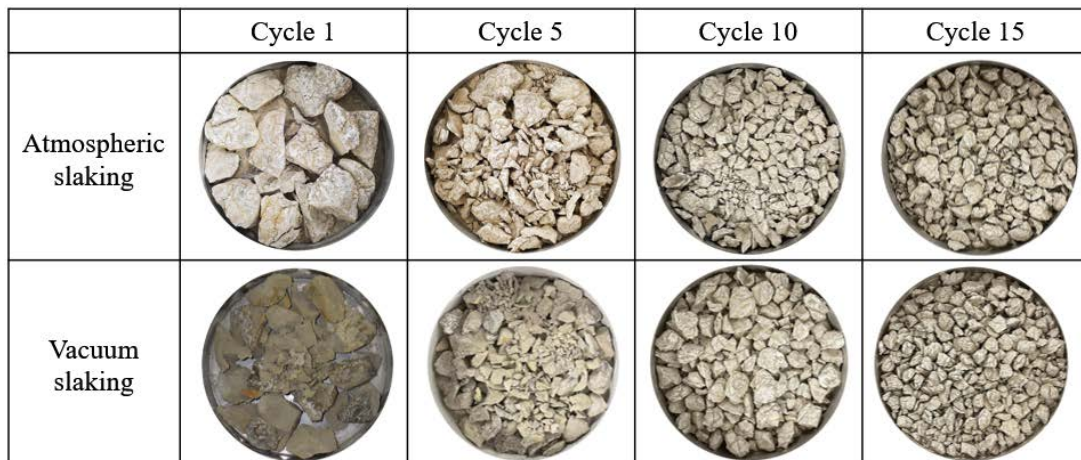
sample quartiles for photographing. Finally, several 3D models of different size particles were reconstructed by filling voxel into the surface models and the Shape-3d ( $S_{3d}$ ) was calculated by the parameter extracted from the 3D models.



**Figure 5-3 Schematic diagram of particles with different Shape-3d ( $S_{3d}$ )**

## 5.2 Results and discussion

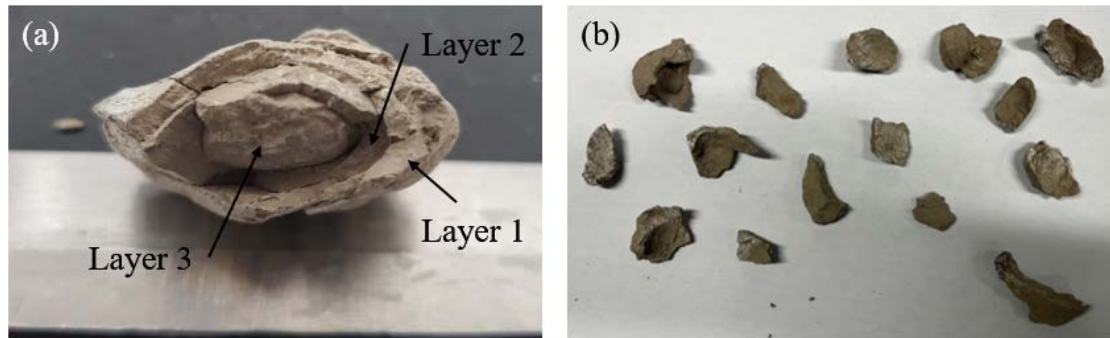
### 5.2.1 General characterization of the slaking process



**Figure 5-4 Specimens during cyclic drying–wetting slaking tests**

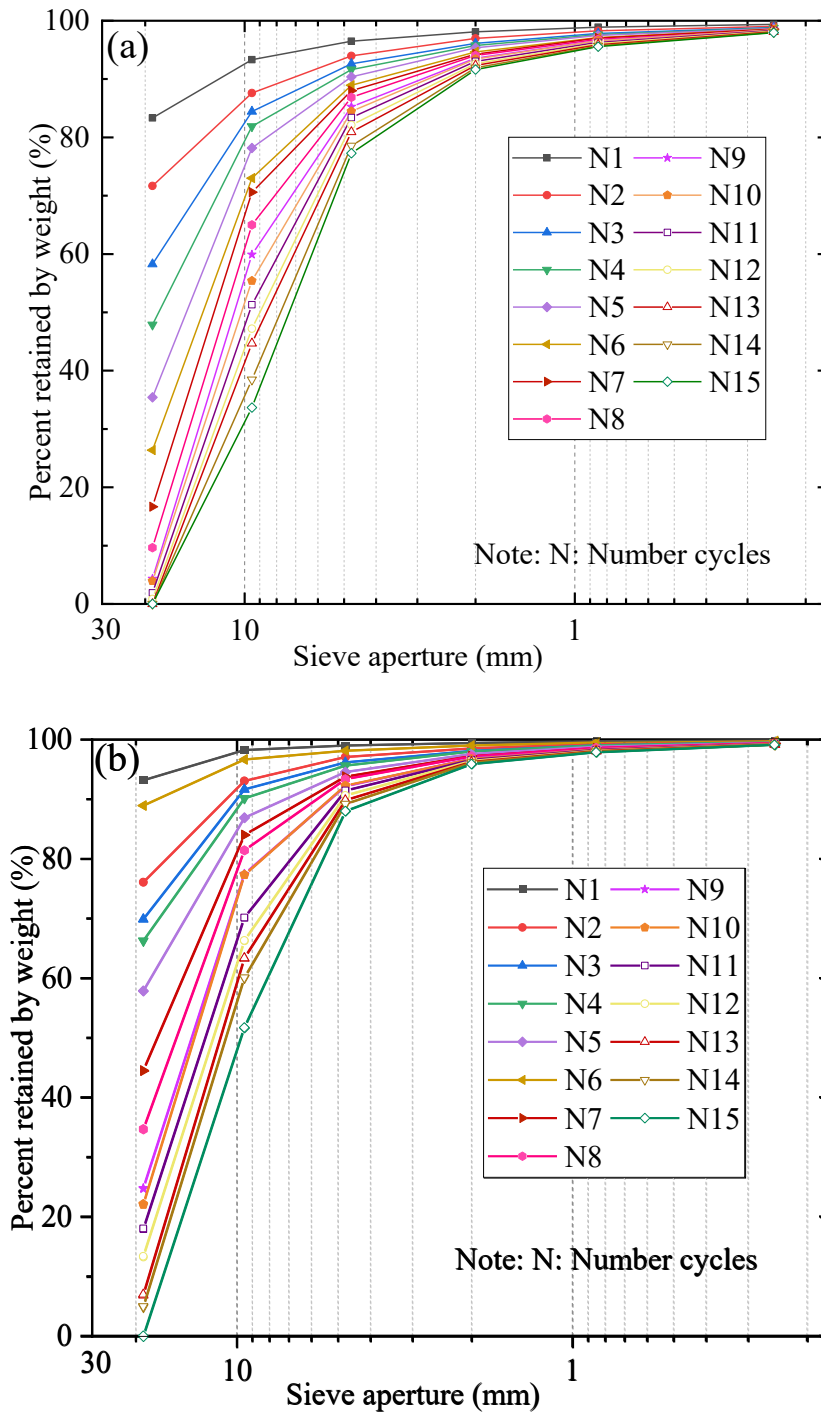
The images of specimen state after cyclic drying-wetting slaking can be seen in **Figure 5-4**. Mudstone specimens are gradually broken into smaller particles in the process of drying and wetting cycles. Comparing pictures of two tests, the slaking rate in vacuum slaking tests seems quicker than the atmospheric one. Moreover, it is interesting that typical particles are widely found as shown in **Figure 5-5**. The structure of large particle,

also named main body particle (>19mm), is layer by layer as shown in **Figure 5-5a**. While medium particle is shell structure, which can be seen in **Figure 5-5b**. These typical structures are caused by the mechanical of mudstone slaking, which will be analyzed later in section 5.2.2.



**Figure 5-5 Some typical particles in the slaking process: (a) primary body particle (b) medium particles**

Because the slaking state are hard to analyze quantitatively via images, the particles size distributions (PSD) of mudstone specimens after drying and wetting cycle were measured by sieves and the results can be seen in **Figure 5-6**. Different from the figure format in standard (JGS 0131-2009), the vertical axis in **Figure 5-6** is present remained by weight and the horizontal axis is arranged from large to small, which is for the convenience of slaking parameter calculation later (Erguler & Shakoor, 2009). The distribution curves of atmospheric and vacuum slaking tests move downwards with the increase of cycle numbers. Furthermore, particle size distribution curves of the atmospheric slaking tests changes quicker than the ones of vacuum slaking tests, which indicated that the slaking characterize of specimens in atmospheric slaking tests is stronger than the one in vacuum slaking tests.



**Figure 5-6 Particle size distribution curves for (a) atmospheric and (b) vacuum cyclic drying–wetting slaking tests**

Each particle size distribution curve corresponds to one slaking state. In order to characterize slaking state by particle size distribution curve, the slaking ratio ( $SL_{ratio}$ ) was proposed by Erguler and Shakoor. 2009. Before tests, the corresponding particle

size distribution curve is c-d line in **Figure 5-7a** because all specimen sizes are larger than 19mm. Thus, the integral of c-d line is the area a-b-c-d for the initial state of specimens. With the process of slaking, the curve changes and blue area in **Figure 5-7a** is the difference area comparing initial state. Based on this, the slaking ratio  $SL_{ratio}$  is calculated by dividing area a-b-c-e by area a-b-c-d, which can be seen in **Figure 5-7a**. The value of  $SL_{ratio}$  corresponds to 0 and 1 for completely non-durable and completely durable, respectively. The relationship between  $SL_{ratio}$  and number of cycles was summarized in **Figure 5-7b**. The values of  $SL_{ratio}$  in atmospheric and vacuum slaking tests decrease from 1 to 0.45 and to 0.56 respectively. In addition, decrease of  $SL_{ratio}$  in atmospheric slaking test gradually slows down. However, the one in vacuum slaking test shows a liner decrease. Thus, the local slope of  $SL_{ratio}$  curves can be calculated for analysis of slaking rate in atmospheric and vacuum slaking tests. As the dash line indicated, the slope of liner evolution of  $SL_{ratio}$  in vacuum slaking test is -0.0295. While three typical slopes of  $SL_{ratio}$  in atmospheric slaking test are calculated, which are -0.0707 in the initial, -0.0295 in medium and -0.0178 in final stage. This trend means that the slaking rate of atmospheric slaking test initially exceeds that of the vacuum slaking test and the slaking rate in these two tests are same in around 8 times of wetting and drying cycles. After that, the slaking rate of atmospheric slaking test is less than that of vacuum slaking test.

The data analysis mentioned above can be explained by the slaking mechanisms. As mentioned in introduction, the mechanisms of slaking can be summarized as: (1) the air-breakage phenomenon, (2) differential swelling, and (3) dissolution of cement agents. Comparing the atmospheric slaking test, the vacuum slaking test eliminates air-breakage phenomenon in the slaking process. Thus, the  $SL_{ratio}$  of vacuum slaking test is smaller than that of atmospheric slaking test as shown in **Figure 5-7b**. For the vacuum

slaking test, the slaking behavior causes by the latter two reason (differential swelling and dissolution of cement agents). Thus, the rate of slaking is stable as shown in **Figure 5-7b**. However, for the atmospheric slaking test, the slaking rate decrease due to two reasons:

1. The slaking mechanism of air-breakage phenomenon is based on cracks of the specimen surface. With the process of slaking, the cracks in the specimens are destroyed by the slaking behavior, which will be explained in detail in section 5.2.3. The rate of slaking decreases due to the disappear of crack.
2. With the same wetting and drying cycle, the size of particles in atmospheric slaking test is smaller than that in vacuum slaking test (see **Figure 5-7**) for the same cycle number. From the perspective of slaking potential, specimens' particles with more small particles are more stable. As a result, reduction of slaking energy results in the decrease of slaking rate.

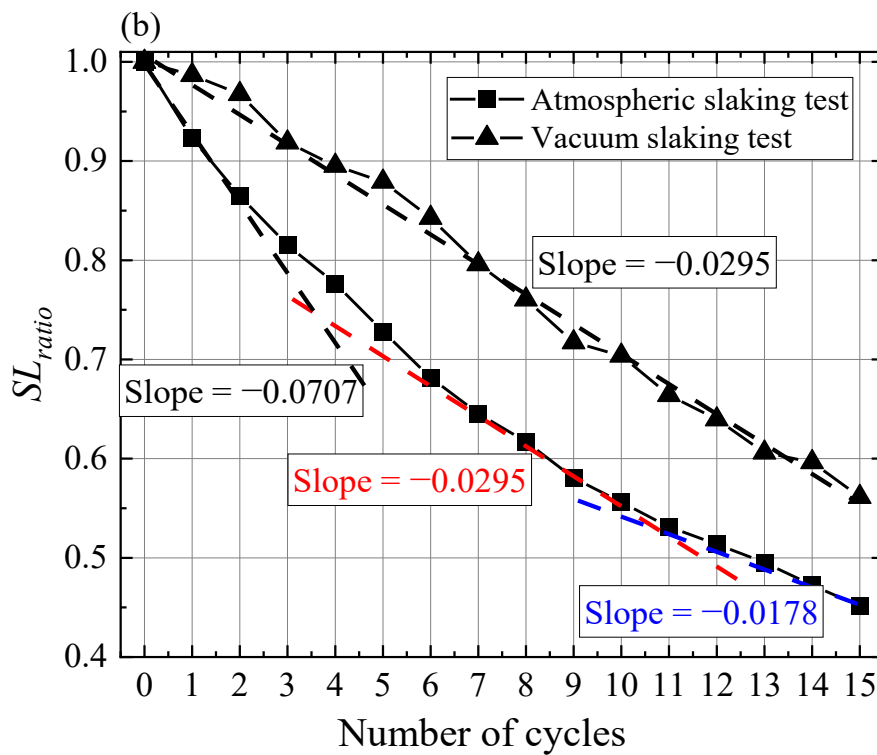
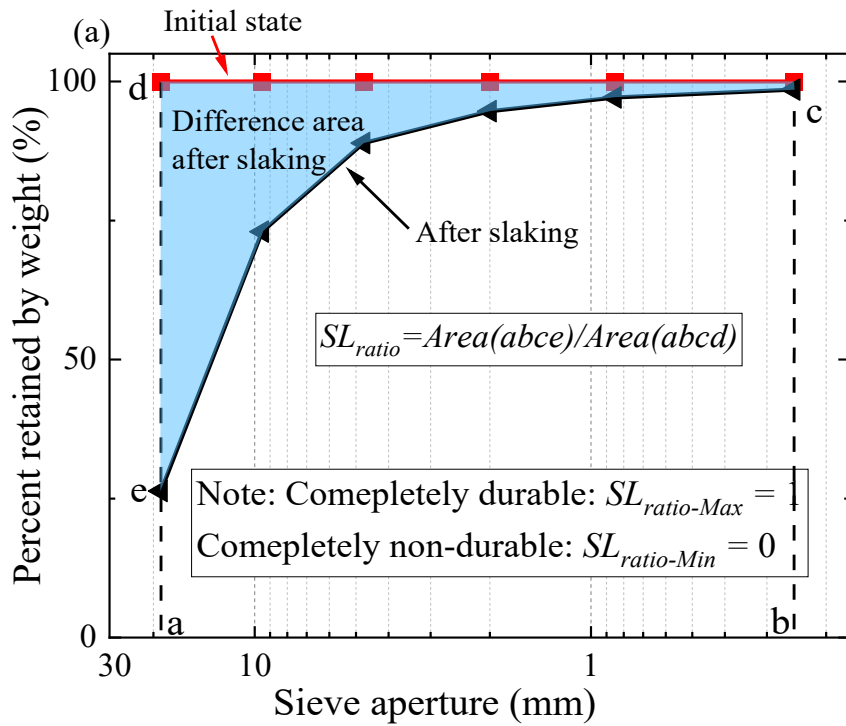


Figure 5-7 (a) Mathematical derivation of the slaking ratio and (b) relationship between  $SL_{ratio}$  and the number of cycles



As mentioned above, there are three mechanisms for slaking phenomenon in atmospheric slaking test. However, there are only two reasons for vacuum slaking test. Thus, the difference of slaking rate between atmospheric slaking test and vacuum slaking test is caused by the air-breakage phenomenon. Finally, proportion of slaking behavior caused by air-breakage phenomenon can be calculated by slaking rates in atmospheric slaking test and vacuum slaking test as the following formula:

$$P_{Air-breakage} = \frac{Slope_{Atmospheric} - Slope_{Vacuum}}{Slope_{Atmospheric}} \quad (5-2)$$

where  $P_{Air-breakage}$  is the proportion of slaking behavior caused by air-breakage phenomenon;  $Slope_{Atmospheric}$  and  $Slope_{Vacuum}$  are the local slopes of  $SL_{ratio}$  curves in atmospheric and vacuum slaking tests as shown in **Figure 5-7b**.

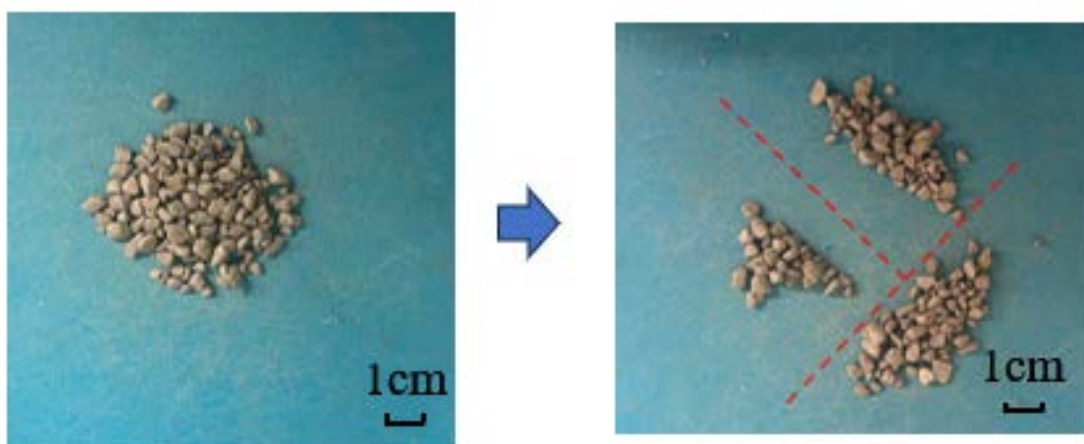
Based on above formula, the  $P_{Air-breakage}$  in the initial state is calculated by the initial slope of  $SL_{ratio}$  curve in atmospheric slaking test and the slope of  $SL_{ratio}$  curve in vacuum slaking test.  $P_{Air-breakage}$  in the initial state is 58.3%, which indicating that in the slaking process of Akita mudstone, the contribution of air-breakage phenomenon is 58.3% in the initial slaking process.

### 5.2.2 Shape evolution of particles

As introduced in Section 2.3, the particles' 3D models can be obtained from the multi-view approach. **Table 5-1** shows the details of the original images, surface models and 3D models. Part of samples were sampled from each group for photographing analysis. The sampling method is based on sample quartiles as shown in **Figure 5-8**. From these pictures and models, medium-sized particles (9.5–4.75 mm) are more irregular and the specific surface area of these medium-sized particles is larger than that of particles with



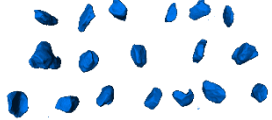
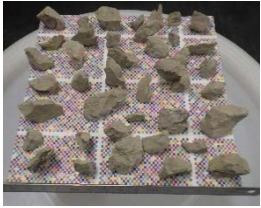
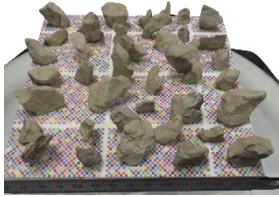
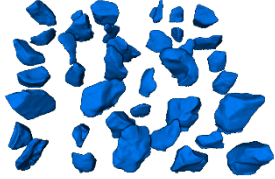











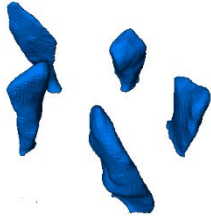
other sizes. **Figure 5-9a** shows the extracted  $S_{3d}$  to study the particle shape evolution quantitatively. Furthermore, the mean values and lower/upper 95% confidence limits are calculated. The lower/upper 95% confidence limit is calculated by the mean value  $\pm 1.96$  times the standard deviation. There are two typical values in the curves: one is the peak value ( $P_v$ ) in the  $S_{3d}$  curve and the other is the primary body's  $S_{3d}$  value ( $R_v$ ) (see **Figure 5-9a**). Original data points were removed to clarify the figure and the figure was transformed into **Figure 5-9b**.

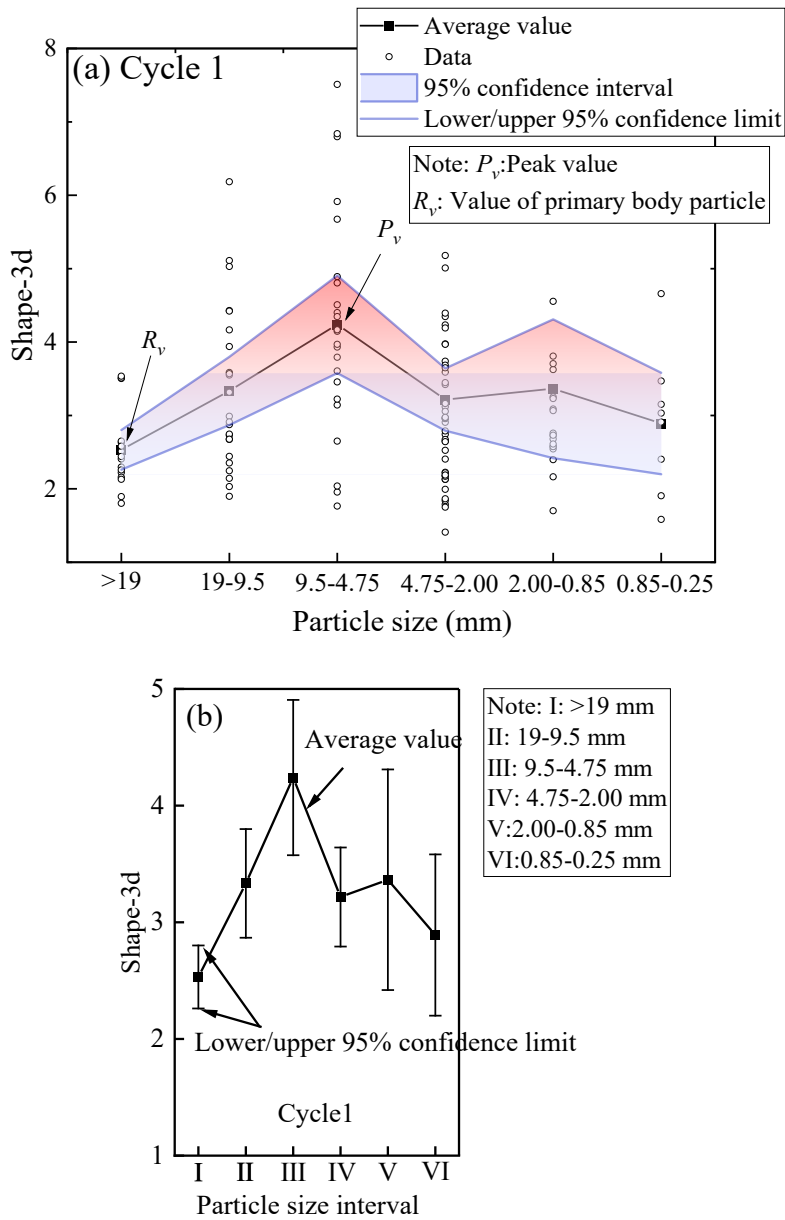
**Figure 5-10** and **Figure 5-11** summarise all shape parameters in the atmospheric and vacuum cyclic drying–wetting slaking tests. For the atmospheric and vacuum slaking tests, the peaks are always in the medium particle size, corresponding to 9.5–4.75 mm. However,  $P_v$  and  $R_v$  decrease with the increase in cycle number. The curves tend to uniform with the slaking process, especially at cycle 15. The difference between the lower and upper 95% confidence limits decrease with the increasing cycle number, indicating that the particles' shapes in the same size range also tend to be uniform. Moreover, the movement of peak positions from II (19–9.5 mm) to III (9.5–4.75 mm) can be seen in cycles 1, 3 and 5 in **Figure 5-11**.



**Figure 5-8 Sampling method**

**Table 5-1 specimens of original images, surface models and 3D models**

	Original pictures	Surface model	3D model
> 19 mm			
19 ~ 9.5 mm			
9.5 ~ 4.75 mm			
4.75 ~ 2.00 mm			
2.00 ~ 0.85 mm			
0.85 ~ 0.25 mm			



**Figure 5-9 (a) Curve of Shape-3d ( $S_{3d}$ ) with original data point and (b) Curve of  $S_{3d}$  after removing original data points**

From the perspective of the slaking mechanism, the shell-like, medium-sized particles cause peaks in the medium-sized particles (**Figure 5-5b**). We hypothesised that the differential swelling might produce these shell-like particles in the slaking process. When water permeates into the specimens, the specimens' surfaces will swell, with no swelling of the inner part of the specimen. Differential swelling pressure breaks mudstone and then produces these shell-like particles. Furthermore, the decrease in

peak values and the movement of peak positions are caused by the further breakage of shell-like particles as the cycle number increases. Furthermore, the water permeates into the sharp parts of the specimens quicker, making the primary body particles' surfaces smoother after the outer layer's desquamate. Finally, this phenomenon decreases  $R_v$  (Figure 5-12) and will be explained in Section 6.2.3.

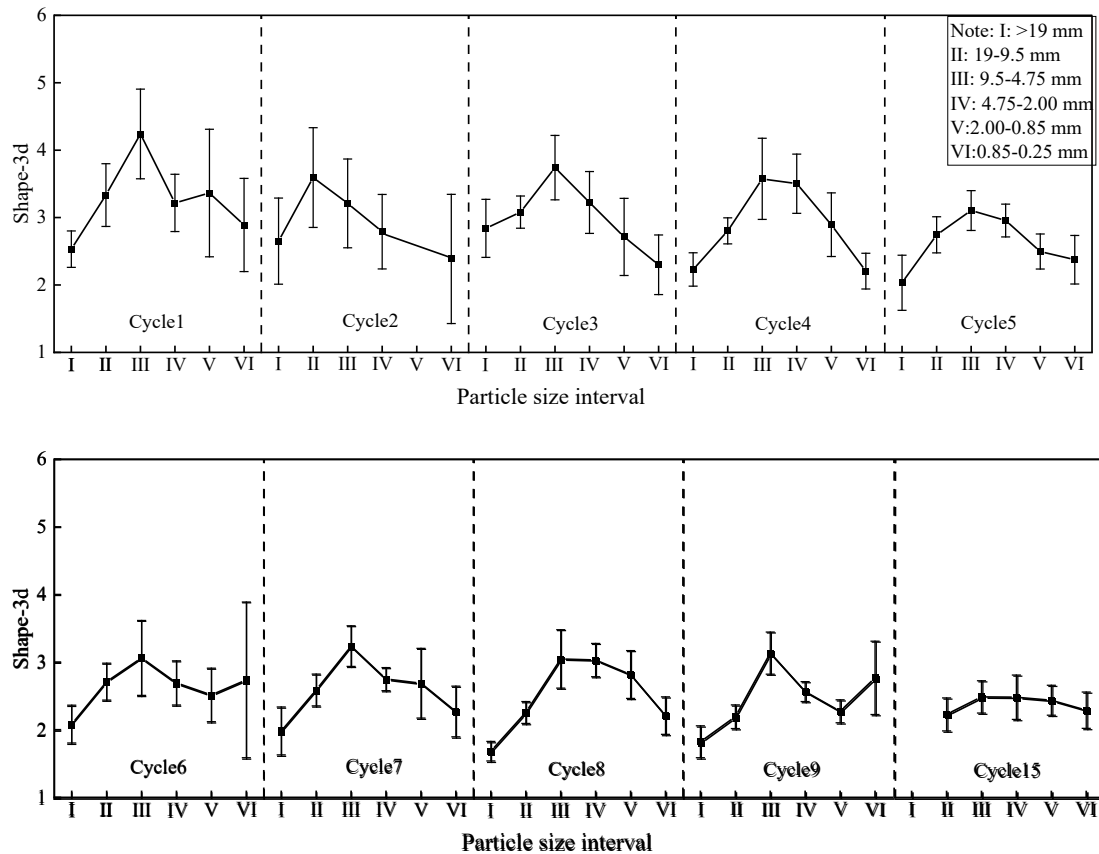
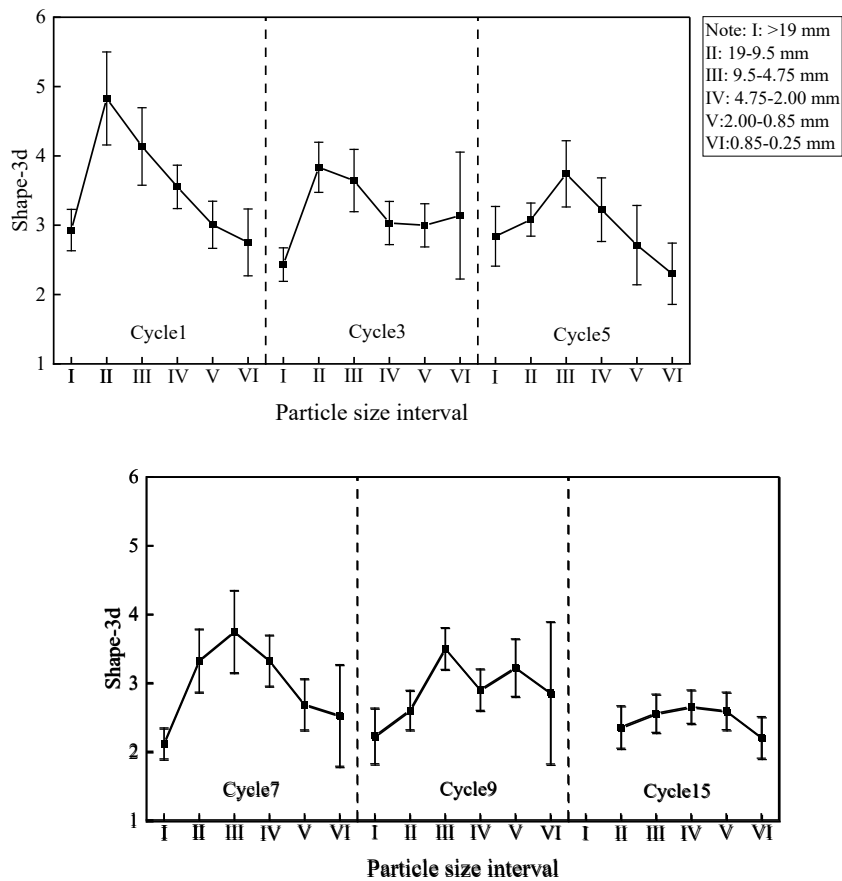


Figure 5-10 Shape-3d ( $S_{3d}$ ) of different particle sizes in atmospheric slaking tests

Figure 5-12 compares the  $P_v$  of the atmospheric and vacuum slaking tests to confirm the above hypothesis. Only large particles existed in the initial state and the  $S_{3d}$  of the atmospheric and vacuum slaking tests are 2.5. After the first cycle, the peak values of the atmospheric and vacuum slaking tests burst to approximately 5 and 4.3, respectively. With further slaking, the peak values in the two tests decrease and finally return to approximately 2.5. In this process, the  $P_v$  in the atmospheric slaking test is always larger

than in the vacuum slaking test. As mentioned above, the air-breakage phenomenon, differential swelling and the dissolution of cement agents contribute to the slaking process in atmospheric slaking tests, while only the latter two mechanisms contribute to the slaking process in vacuum slaking tests. After removing the effect of the air-breakage phenomenon, the proportion of particles caused by differential swelling increases, meaning that the proportion of shell-like particles increases. Thus, the larger  $P_v$  in the vacuum slaking test is caused by a more pronounced differential swelling effect in the vacuum slaking process, proving the hypothesis above.



**Figure 5-11 Shape-3d ( $S_{3d}$ ) of different particle sizes in vacuum slaking tests**

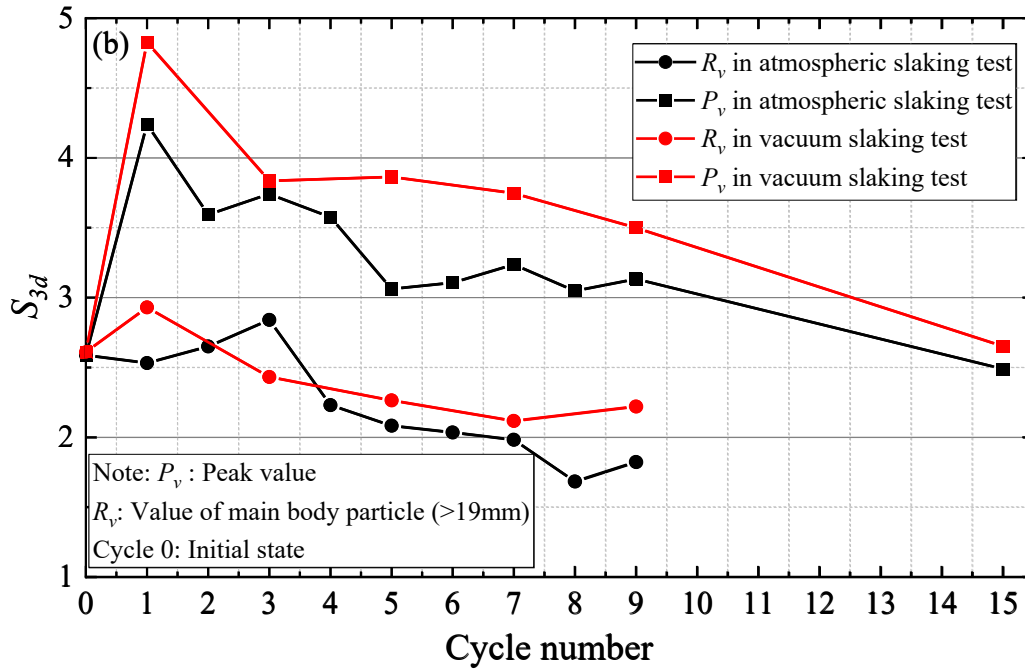


Figure 5-12 Evolution of  $P_v$  and  $R_v$  in cyclic atmospheric and vacuum slaking tests

### 5.2.3 Slaking mechanism of Akita mudstone

In this study, swelling strain tests and atmospheric and vacuum slaking tests are designed to explore the mechanisms of slaking in Akita mudstone. Although studies have proposed the differential swelling mechanism, it is considered to be caused by clay-enriched areas (Liu *et al.*, 2020; Su *et al.*, 2020). This study proposes a new insight into the differential swelling mechanism. The differential swelling mechanism caused by the uneven water distribution during water infiltration results in a typical layered slaking phenomenon.

Figure 5-13 shows two co-existing mechanisms for Akita mudstone slaking. Some pre-existing cracks in the specimens occur in the initial state (Figure 5-13a). After wetting, the water fills these cracks, and the compression of entrapped air develops cracks (Figure 5-13II). Finally, the connection of cracks breaks the specimen. Figure 5-13II

shows some typical specimens broken by the air-breakage phenomenon. The cracks disappear due to the air-breakage phenomenon in the slaking process, decreasing the slaking rate in the atmospheric slaking tests (**Figure 5-7b**). However, the slaking rate of vacuum slaking tests remains the same in 15 wetting and drying cycles because the vacuum removed the air-breakage phenomenon.

However, the differential swelling mechanism also works during slaking. This study has proven that the structure of natural mudstone confines the swelling behavior (**Figure 3-12**). After repeated swelling stress, the swelling behavior break the specimens. Thus, as the water penetrates from the surroundings (**Figure 5-13b**), the mudstone surface swells while the inner drying shows no volume change when the specimens are not saturated totally. Subsequently, the surface part separates from the specimen and a gap between the primary body and slaking particles occurs (**Figure 5-13c**). Finally, the specimen's outer shell-like structure is broken from the primary body specimen (**Figure 5-13d**). The surface in the breakage area is smooth, as shown in the specimen images. Comparing the specimens broken by the air-breakage phenomenon, the specific surface area of the shell-like particle is larger, resulting in the peaks in **Figure 5-10** and **Figure 5-11**. Moreover, the water penetrates the rough parts of the specimen surface easier than the other areas due to the larger contact area with the water (**Figure 5-13l**). Thus, the sharp part in the specimen's surface desquamated from the primary body of specimens, decreasing  $R_v$ .

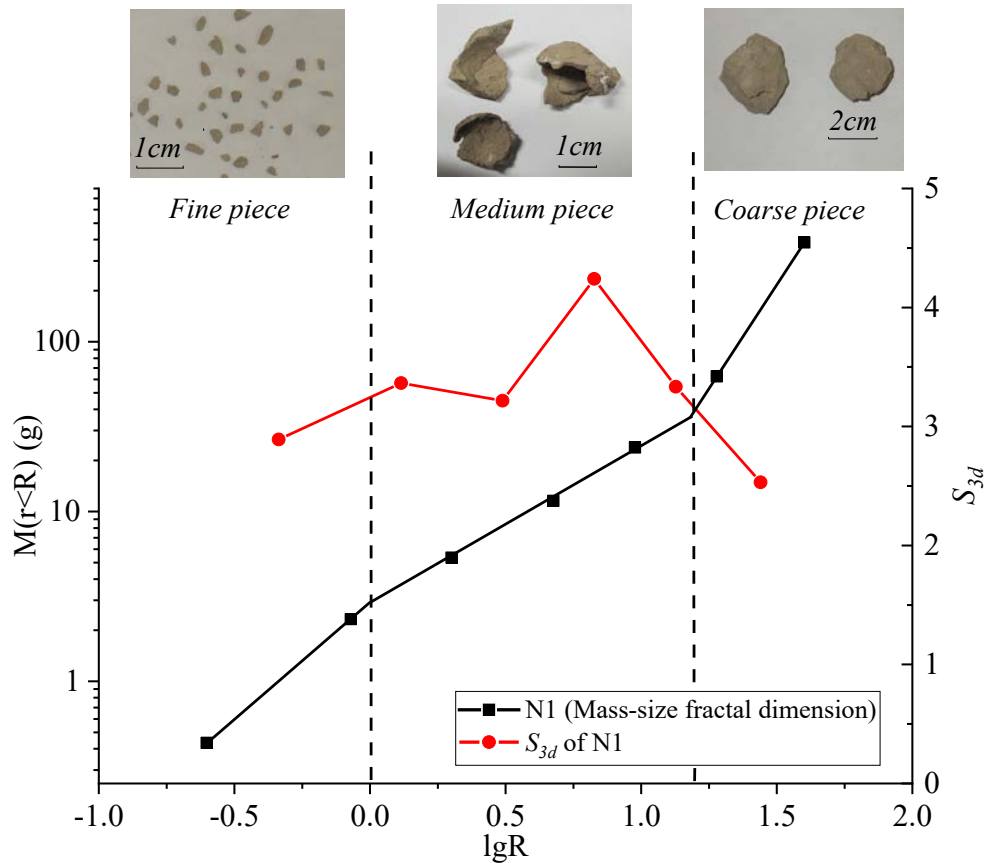




#### 5.2.4 Fractal models of mudstone

The fractal dimension is employed in slaking to describe the degree of mudstone slaking (Tyler and Wheatcraft, 1992; Liu, Zhao and Su, 2006; Su *et al.*, 2020). The existing fractal models are based on number-size, volume-size and mass-size distribution. The fractal model based on mass-size distribution is widely used because the mass value is easy to measure. Recently, the tri-piecewise linear fractal dimension model was proposed (Su *et al.*, 2020), which can better describe particle size distribution during slaking. However, this model assumes that the particles are divided into fine, medium and coarse pieces.

This assumption can be explained by the particle shape analysis in this study. **Figure 5-14** compares the mass-size fractal dimension and  $S_{3d}$  of cycle1 in the atmospheric slaking tests. For the mass-size fractal dimension, the slopes in fine and coarse pieces are larger than in medium pieces, similar to the results in Su *et al.*, 2020. Furthermore, the  $S_{3d}$  of coarse and fine piece is smaller than that of the medium piece, caused by the differential swelling mechanism (Section 5.2.3). The medium piece with a larger  $S_{3d}$  makes the particles harder to pass the sieve mesh. Finally, these medium particles remain in the sieves with larger mesh sizes, resulting in a smaller slope in the medium piece in the mass-size fractal dimension.



**Figure 5-14 Relationship between  $S_{3d}$  and mass-size fractal dimension**

## Conclusions

This study explores the slaking mechanisms by swelling strain tests and comparing atmospheric and vacuum cyclic drying–wetting slaking tests. With similar dry densities, the swelling strain of natural mudstone is much lower than the remolded ones, indicating that the structure of natural mudstone confines the swelling behavior and this repeated swelling stress during cyclic drying–wetting is a reason for slaking. In the cycling drying and wetting slaking tests, the results of particle size distribution indicate that the slaking rate of atmospheric slaking tests decreases because the disappearing of cracks in the slaking process reduces the air-breakage phenomenon. The atmospheric

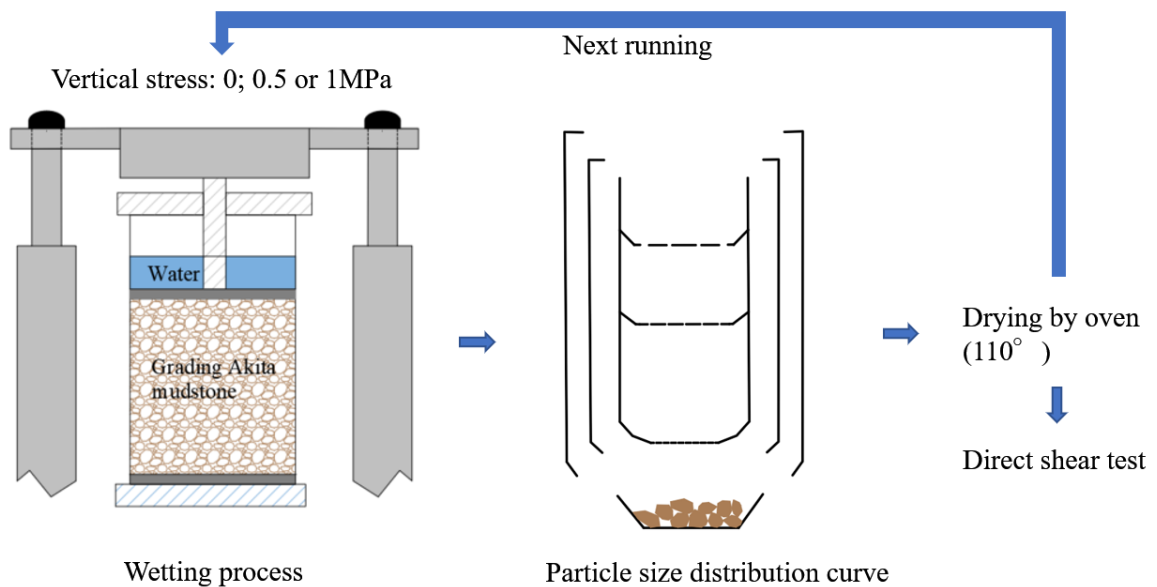
slaking rate is quicker than the vacuum slaking tests and then outpaced by the vacuum slaking rate after 8 times of drying–wetting process. Furthermore, the vacuum slaking rate is constant in 15 wetting and drying cycles due to no air-breakage in the vacuum slaking tests. Furthermore, the proportion of the air-breakage phenomenon in the slaking behavior of Akita mudstone is 58.3% in the initial slaking process.

During the tests, the shape of Akita mudstone during slaking was studied using the multi-view approach. The medium particles typically have a larger specific surface area than particles of other sizes, resulting in peaks in the  $S_{3d}$  curves. These peak values in the vacuum slaking tests are larger than in the atmospheric slaking tests, indicating that the differential swelling mechanism causes the shell-like medium specimens. Finally, two co-existing mechanisms for Akita mudstone slaking were explored and a new insight into the differential swelling mechanism due to the uneven water distribution during slaking behavior was proposed. A typical layer-slaking phenomenon caused by this differential swelling mechanism was observed.

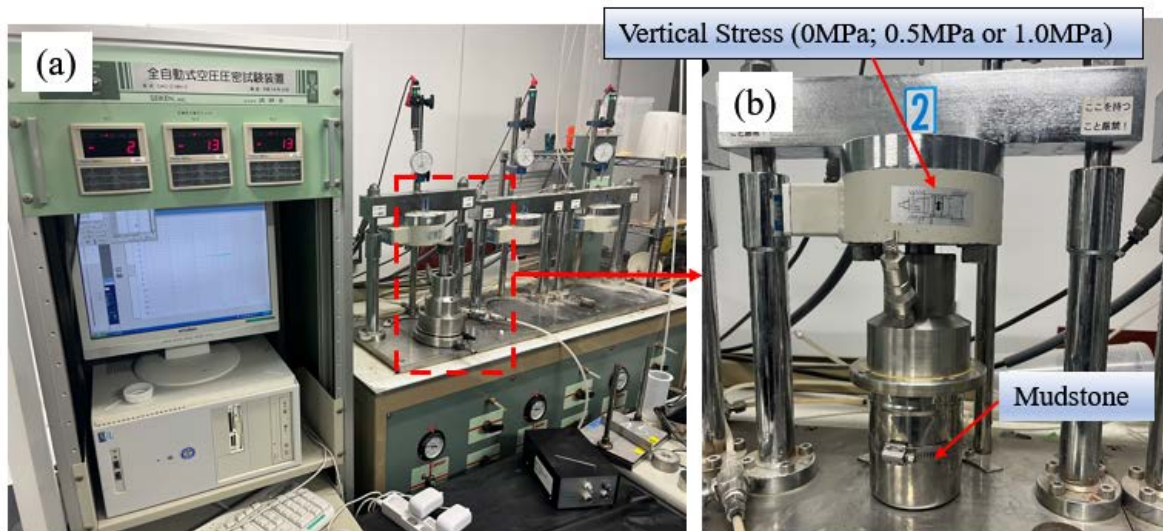
**Chapter 6. SLAKING BEHAVIOR OF  
AKITA MUDSTONE UNDER STRESS AND  
THE SHEAR STRENGTH EVOLUTION  
DURING SLAKING PROCESS**

## 6.1 Testing overview

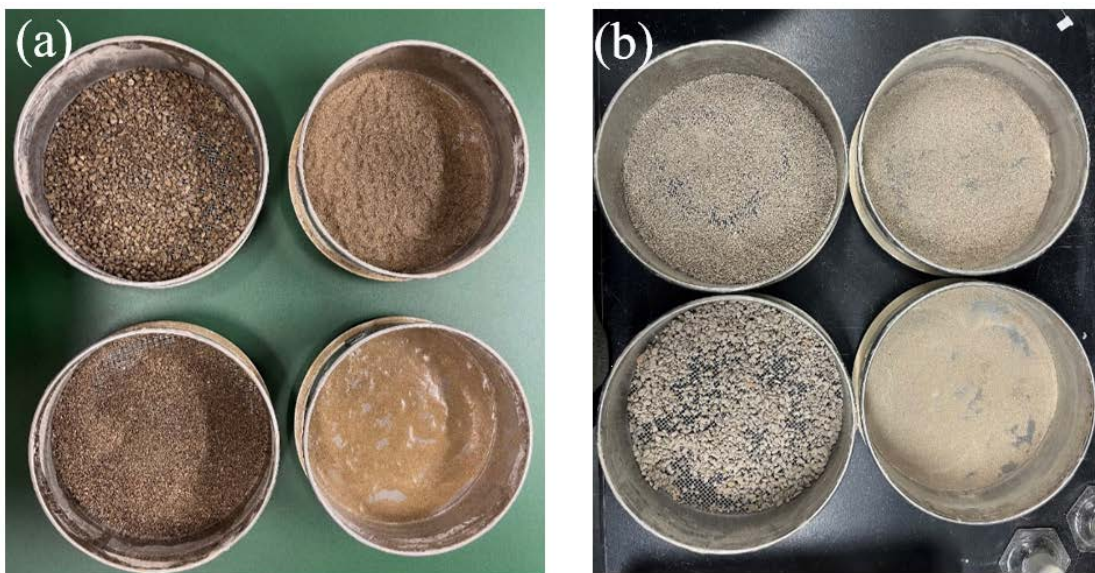
The grading Akita mudstone are used for wetting-drying cycle slaking tests in this chapter. The procedure of the wetting-drying cycle slaking test under vertical stress can be seen in **Figure 6-1**. Specimens are wetted by distilled water and then a vertical stress is applied to the specimen in a steel container by the consolidation apparatus (see **Figure 6-2**). After 24h of wetting, the specimen was sieved with mesh sizes of 2.00, 0.85, 0.25 and 0.106 mm. After sieving, specimens were dried by oven ( $110^{\circ}$ ) for 24h (see **Figure 6-3**) and weighed thereafter. It is worth noting that the sieve process was performed on saturated specimen because it was difficult to be broken after drying. The above procedure is one cycle and specimens after slaking were gathered and mixed for next cycle. Finally, 6 cycles were performed under each vertical stress (i.e. 0MPa; 0.5MPa or 1MPa).



**Figure 6-1 Cycle slaking process under vertical stress**



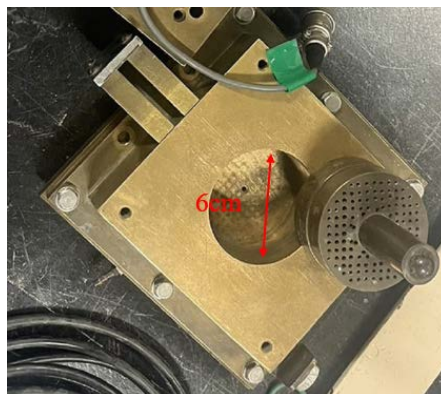
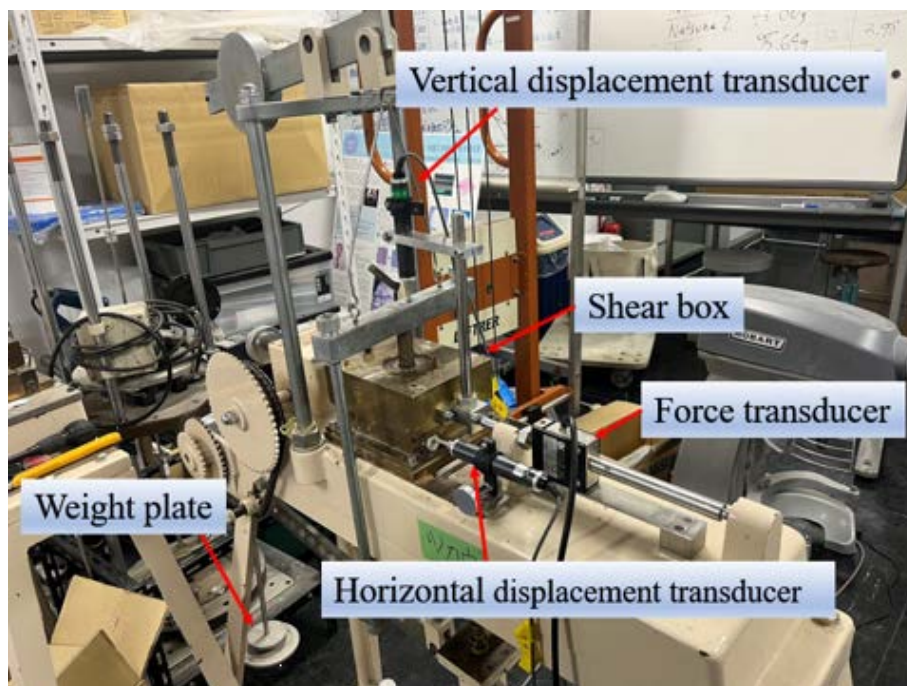
**Figure 6-2** Devices for applying stresses in wetting-drying cycle slaking tests



**Figure 6-3** Drying process: (a)before drying and (b)after drying

In the wetting-drying cycle slaking tests, the particle size distribution (PSD) evolution of grading Akita mudstone were obtained. And after that, the grading Akita mudstone were prepared according to obtained PSD for direct shear tests. Direct shear apparatus is shown in **Figure 6-4**. There are two displacement transducers to measure the horizontal and vertical displacement and one load cell for measuring the shear strength. The shear box diameter is 60mm and a shear rate of 1 mm/min was employed during

tests. The tests were conducted with low normal stresses of 50, 100, or 150 kPa to avoid the breakage of mudstone caused by the normal stress before shear test. During the tests, the normal stress was first applied to the top of the saturated specimens. After the vertical displacement reached equilibrium, a shear force was applied to the lower box, while the normal stress was maintained at a constant level. The grading Akita mudstone with the same PSD of cycle 2, 4 and 6 under different vertical stresses were used for direct shear tests.



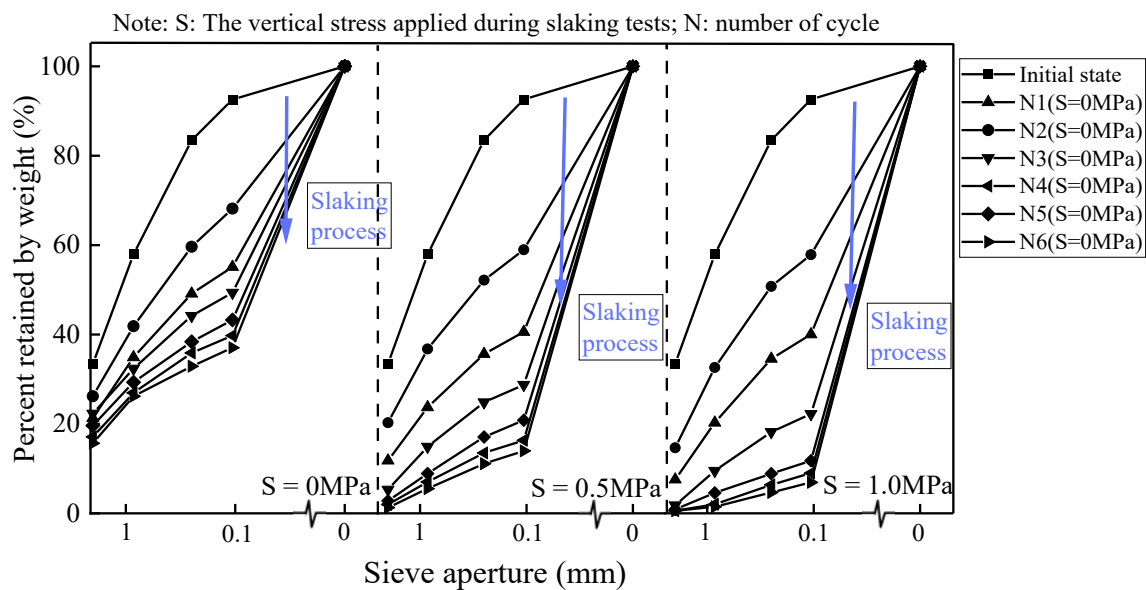
**Figure 6-4 Direct shear instrument used in this study**

## 6.2 Results and discussion



### 6.2.1 Slaking behavior of Akita mudstone under stress

The results of particle size distribution (PSD) curves during slaking test under different vertical stresses are shown in **Figure 6-5**. Note that the vertical axis in **Figure 6-5** is percent retained by weight. As can be seen in **Figure 6-5**, the distribution curves of slaking tests under either confining stress move downward with the increase in cycle numbers. Furthermore, PSD curves of the slaking tests with larger vertical stresses (0.5MPa or 1.0MPa) changes faster than the one without vertical stress (0MPa), which indicated that the slaking phenomenon of specimens slaking under stress is stronger than the one without stress.



**Figure 6-5** Particles size distribution curves during slaking test under different stresses

To characterize slaking state, the slaking ratio ( $SL_{ratio}$ ) proposed by Erguler and Shakoor. (2009) is used herein. It was defined, as shown in **Figure 6-6**, as the ratio of area of a-b-c-e to that of a-b-c-d, where the red line (i.e. c-d line) indicates the original PSD curve

and the c-e line denotes the PSD curve after slaking. The values 0 and 1 of  $SL_{ratio}$  correspond to the completely non-durable (complete slaking) and completely durable condition (no slaking) to slaking, respectively. As can be seen in Fig. 3b, with the increase in cycle number,  $SL_{ratio}$  with different stresses (0MPa, 0.5MPa and 1.0MPa) decreases from 1 to 0.46, 0.14 and 0.08, respectively. This indicates that the vertical stress can accelerate the slaking process.

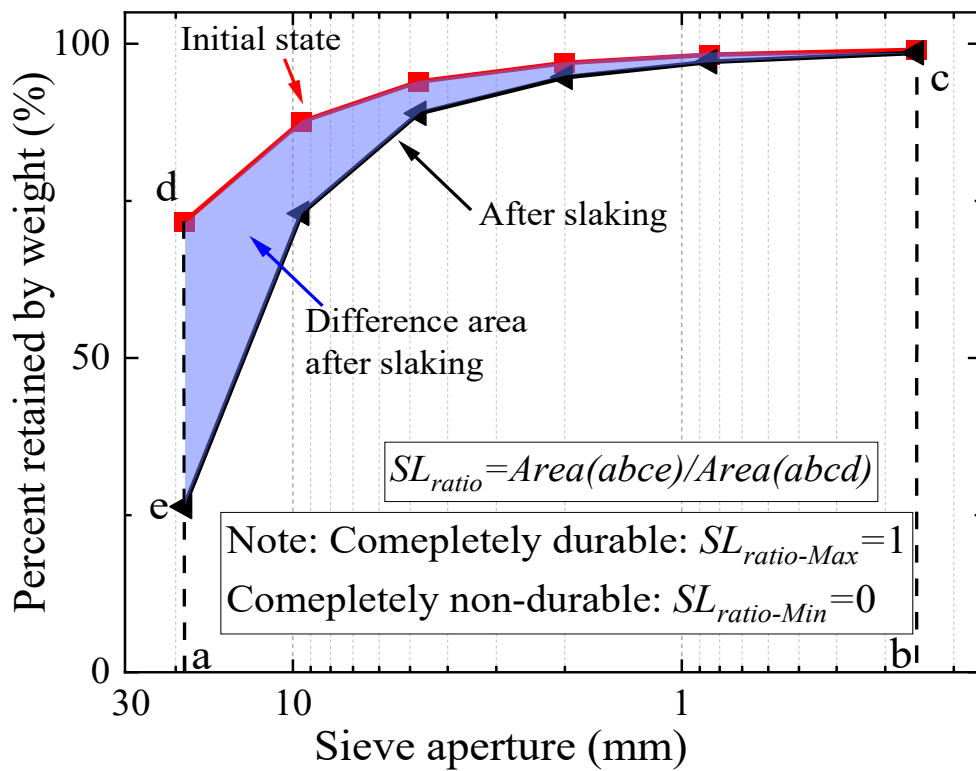


Figure 6-6 Mathematical derivation of the slaking ratio

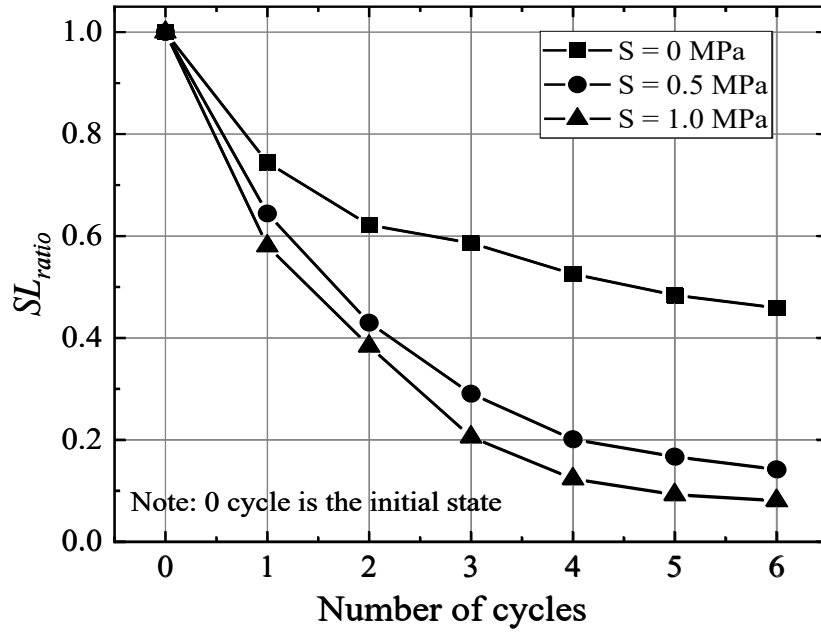


Figure 6-7 Evolution of  $SL_{ratio}$  with slaking process under different vertical stress

6.2.2 Shear strength evolution during slaking process

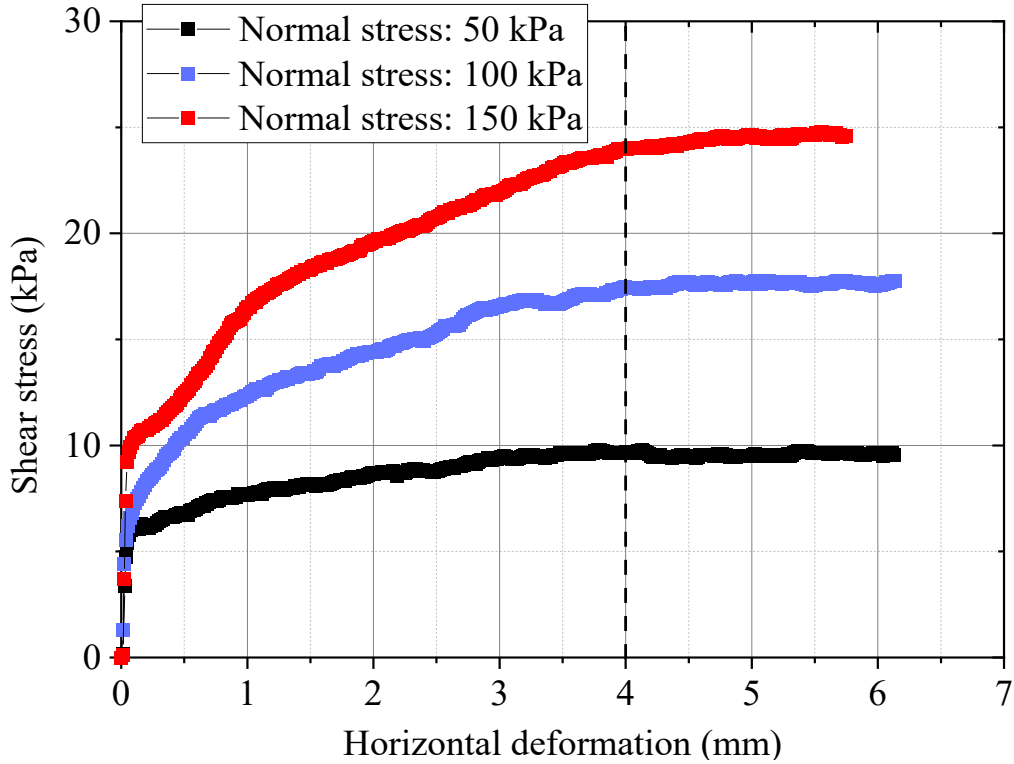
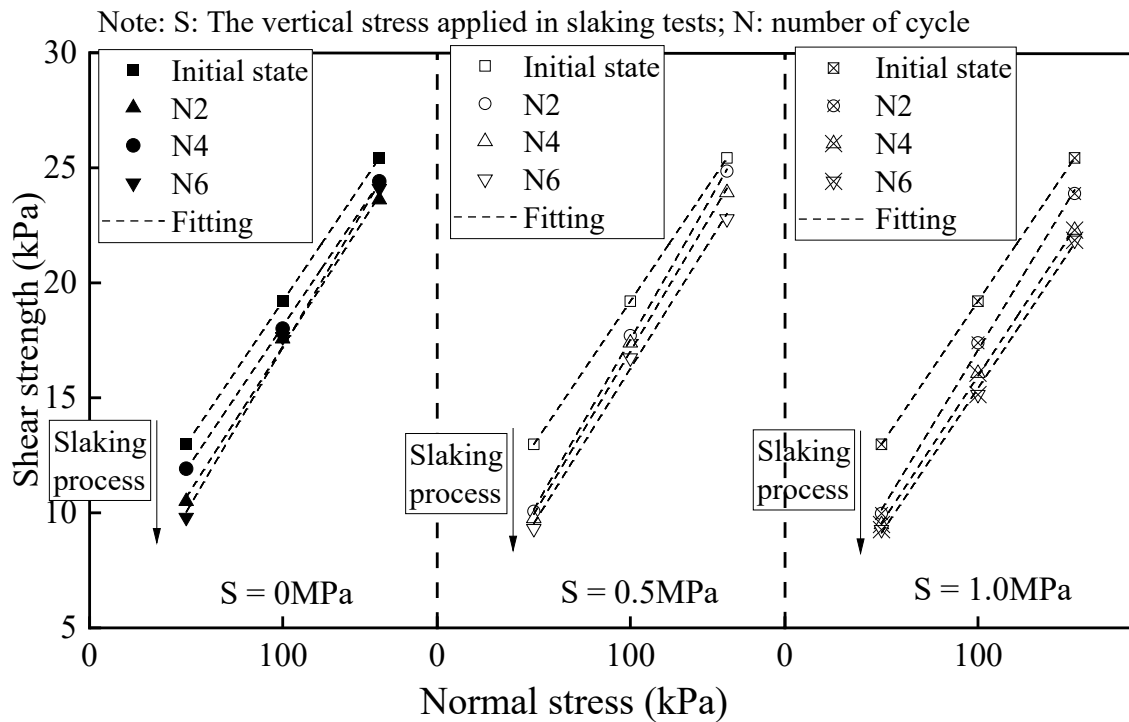


Figure 6-8 An example of relationship between horizontal deformation and shear stress (vertical stress: 0MPa; number of cycle: 6)

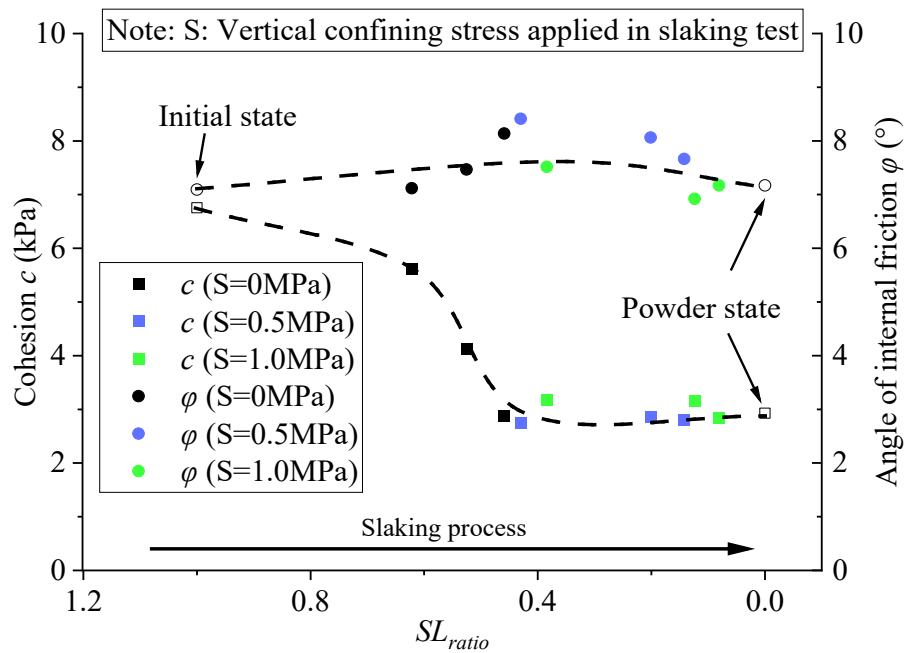
An example of relationship between horizontal deformation and shear stress is shown in **Figure 6-8**. The particle size distribution (PSD) of the sample in the example was prepared based on the PSD of the sample after 6 cycles of slaking under 0MPa vertical pressure. For each direct shear test, the maximum horizontal displacement is around 6mm. As can be seen from the Figure, there is no obvious peak in the shear stress under different normal pressures. Therefore, the shear stress at a shear displacement of 4mm is taken as the maximum shear strength.



**Figure 6-9 Shear strength evolution during the slaking process**

After determining the maximum shear strength, the shear strength evolution during slaking process is summarized in **Figure 6-9**. And these data were linear fitted for obtaining the cohesion ( $c$ ) and angle of internal friction ( $\phi$ ). With the slaking process under different stresses, the maximum shear strength decreases due to the evolution of PSD. The fitting line is move down with the increase of cycle number. Among them,

the fastest change can be seen in the maximum shear strength of cycle slaking test under 1.0MPa. This is because the vertical stress accelerated slaking process of the mudstone, resulting in a faster change in its PSD compared to specimens without vertical stress (see **Figure 6-5** and **Figure 6-7**). The change in PSD of mudstone led to a decrease in the maximum shear strength in **Figure 6-9**.

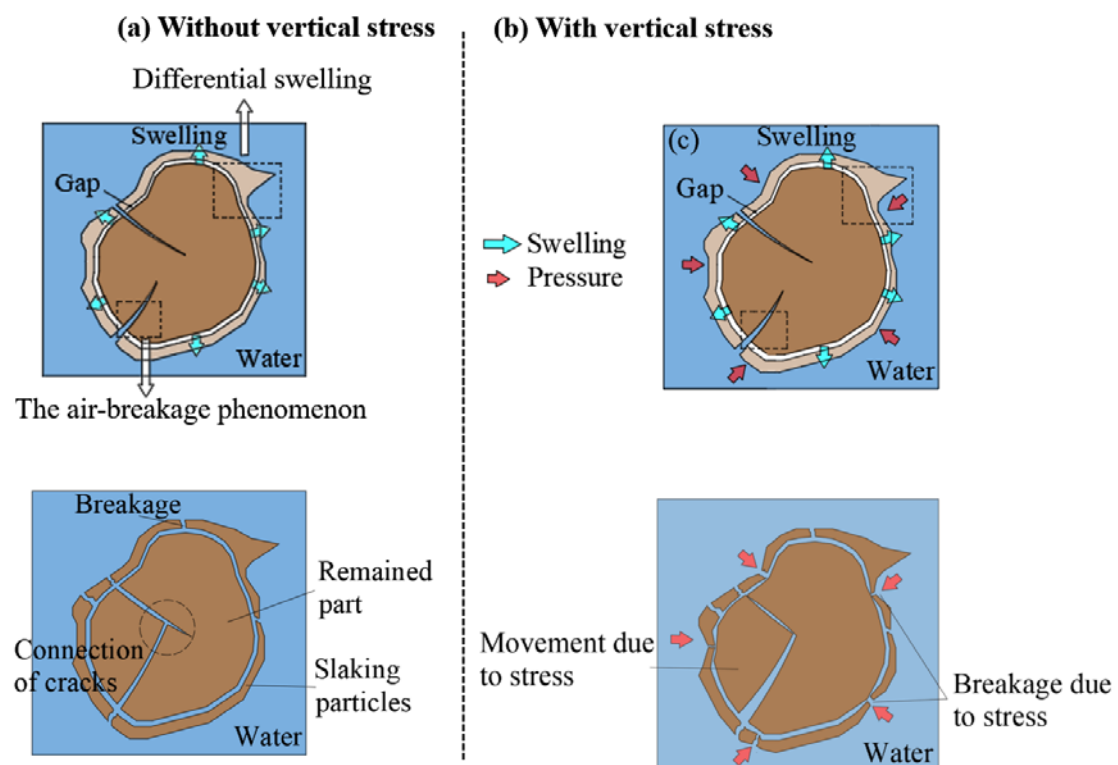


**Figure 6-10 Summarize of  $c$  and  $\phi$  during slaking process**

The evolutions of cohesion ( $c$ ) and angle of internal friction ( $\phi$ ) during slaking process under each vertical stress are summarized in **Figure 6-10**. As can be seen in the figure, with the slaking process, the cohesion ( $c$ ) decreases from 7 kPa to 3 kPa with the decrease of  $SL_{ratio}$  from 1 to 0.4 and it remains almost constant through subsequent slaking process. On the other hand, the value of internal friction ( $\phi$ ) fluctuated slightly between  $7^\circ$  and  $8^\circ$  throughout the slaking, with no significant change. This indicates that with the slaking process, the PSD of specimen changes, and this change results in the decrease of cohesion ( $c$ ) of specimen.

### 6.2.3 Slaking mechanism of Akita mudstone under stress

The mechanism of Akita mudstone has been discussed in chapter 5. As water seeps into the mudstone block, uneven swelling causes separation between the external and internal parts of the specimen and a gap between them appears, as shown in **Figure 6-11**. If stress is applied to the specimen at this point, the shell-like surface layer will be easily broken. Moreover, the stress applied on the specimen also develops the cracks which caused by air-breakage phenomenon. Finally, the movement of part besides the cracks also accelerate the slaking process. In summary, stress exacerbates the differential swelling and air-breakage phenomena that contribute to the breakage of the specimens. And furthermore, intensifying the process of slaking in Akita mudstone.



**Figure 6-11 Mechanism of mudstone slaking (a)without vertical stress or (b)with vertical stress**

## Conclusion

Vertical stress accelerates the slaking process of Akita mudstone. With the increase of vertical stress, the phenomenon of slaking will also be further intensified, which results in larger change in PSD of grading Akita mudstone. And with the PSD change of specimens during slaking process, cohesion value decreases from 7 to 3kPa until the  $SL_{ratio}$  reaches 0.4 and then remain constant. Meanwhile, the change angle of internal friction is not visible during slaking process, fluctuating between 7 and 8°.

**Chapter 7. SHRINKAGE AND CRACKING**  
**EVOLUTION OF AKITA MUDSTONE WITH**  
**DIFFERENT NACL SOLUTION**

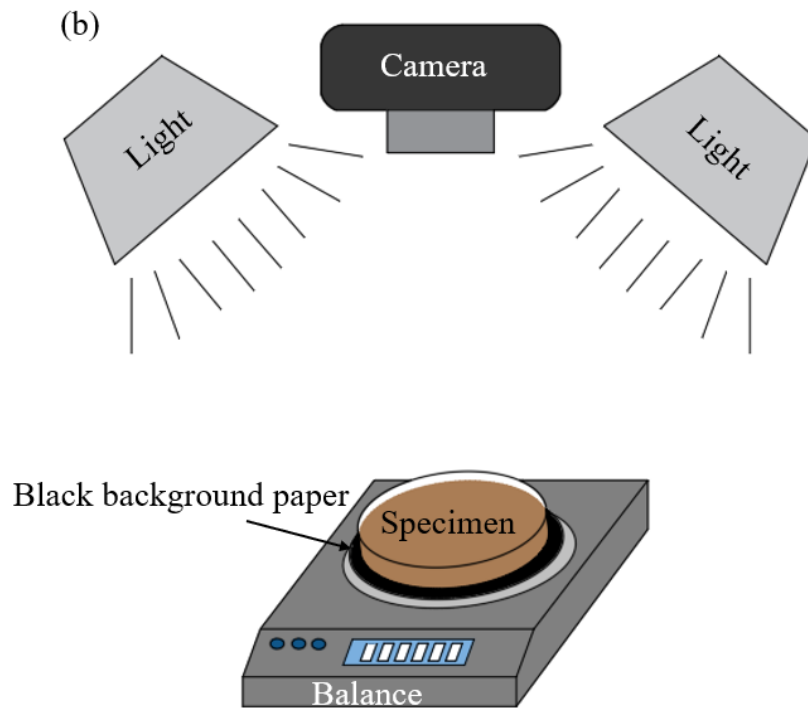
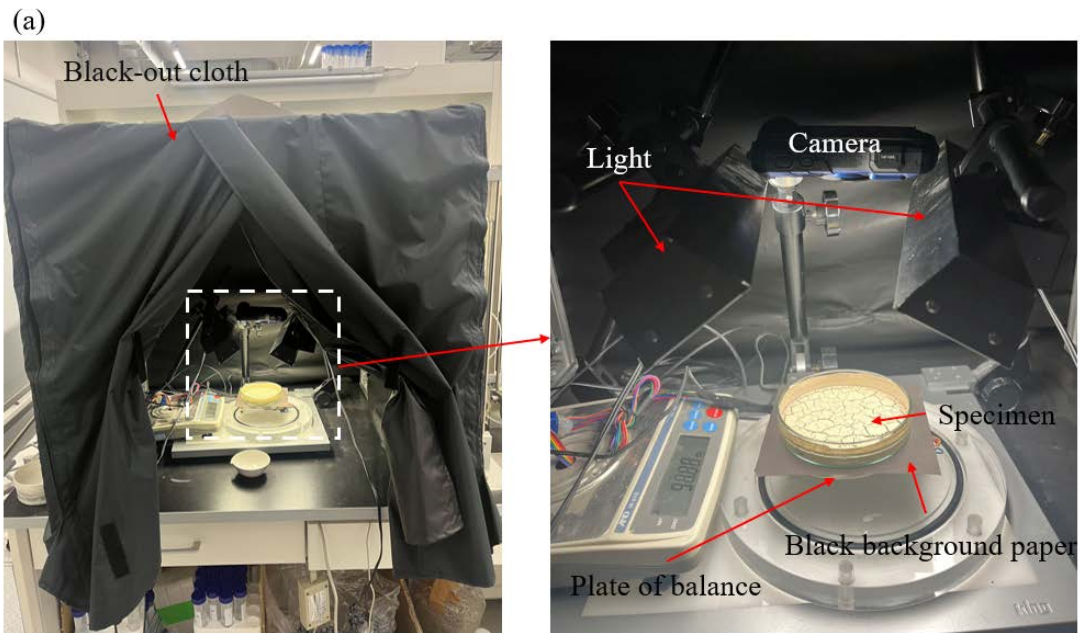


## 7.1 Testing overview

### 7.1.1 Cracking test

**Figure 7-1** shows the photography equipments for cracking tests. As can be seen from the figure, the saturated specimen is placed in a container with diameter of 10cm. Above the container is a camera with a resolution of 3024×4032 pixels. There are two lighting devices next to the camera to ensure that the specimen is always under the same lighting environment during the test. Below the specimen is a black background plate, which allows the color of the cracks to remain black after cracking. Beneath the black background plate is a balance, which can monitor the weight of the specimen and calculate the water content. Finally, high-quality and comparable crack images can be obtained.

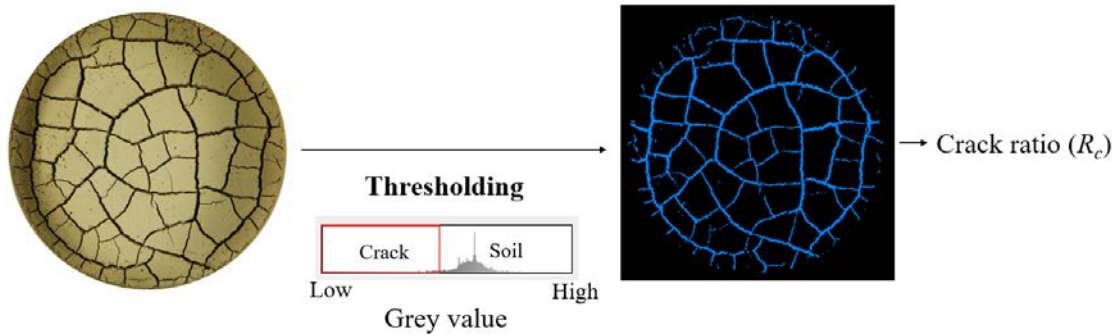
To investigate the effect of NaCl solution on crack evolution, distilled water and four different concentrations of sodium chloride solution (2%; 5%; 10%; 15%) were used to saturate powder Akita mudstone specimens of the same mass (30g). It is worth noting that the water content was calculated by dividing the mass of pure water by the weight of the specimen. Based on this, the specimens were wetted to the same weight moisture content (100%) in each cracking test. After specimen making, the specimen was set on the plate and camera took an image every half hour until the cracks did not change significantly. Moreover, maintaining constant humidity and temperature (20°C) during the cracking process. After that, the sample was dried by a 110°C oven and a picture of the cracks in the completely dried sample was taken after totally drying.



**Figure 7-1 Equipments used for taking pictures in this study**

The procedure of image processing is shown in **Figure 7-2**. After cutting, median filter (denoising), opening and closing, threshold segmentation is applied to the image to extract the crack parts in the image. After this, the crack ratio ( $R_c$ ) can be calculated by dividing the crack area by the total specimen area including soil area and crack area. It

should be noted that the threshold was chosen by visual inspection and the same threshold value was used for all images in this study.



**Figure 7-2 Image process**

### 7.1.2 Soil-water retention curve test

Powder Akita mudstone is mixture by distilled water to obtain the specimens of different moisture content. These specimens are sealed for a week to allow for uniform distribution of moisture throughout the sample. After that, WP4C dewpoint potential meter (see **Figure 7-3**) is used in this study to measure the suction value of specimens and moisture content of specimens was measured. Finally, Soil-water retention curves (SWRC) of Akita mudstone is obtained.



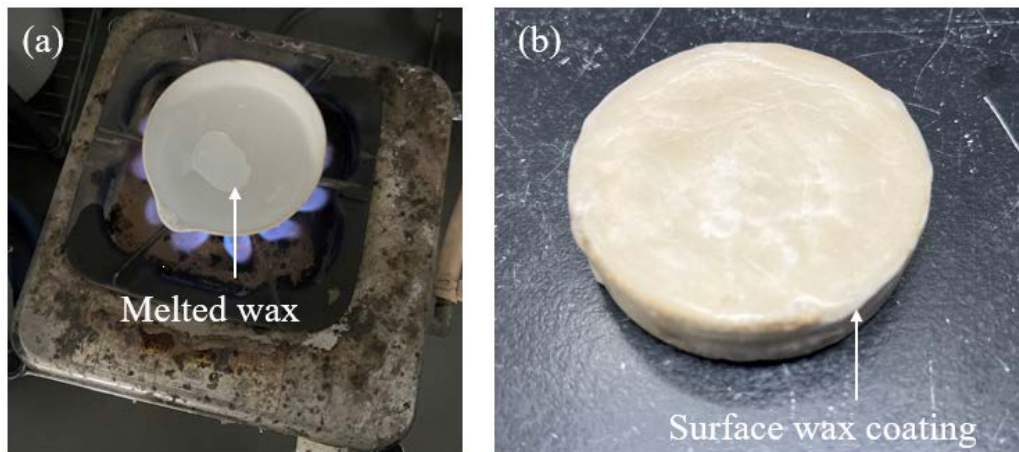
**Figure 7-3 WP4C Dewpoint Potential Meter**

### 7.1.3 Shrinkage test

Powder Akita mudstones are used for shrinkage tests. The powder Akita mudstone saturated by distilled water and four different concentrations of sodium chloride solution (5%; 10% and 15%). Moreover, the initial specimens are also wetted to the same weight moisture content (100%) as in the cracking test. After that, the slurry-like specimens are poured into glass containers with a diameter of 30mm and a height of 10mm, and dried in a 40°C oven before being sealed at a certain water content. It is worth noting that some samples were dried in a 110°C oven to achieve specimens with low water content. As can be seen in **Figure 7-4**, there are no cracks in these specimens because the size of container is smaller than that in cracking test. These specimens can be removed from the glass container easily due to the lubricant on the inner wall of the glass container.

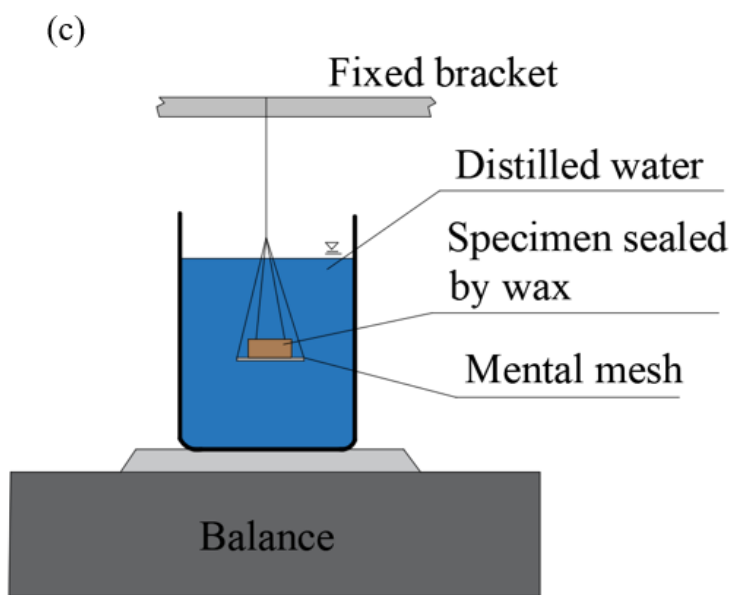
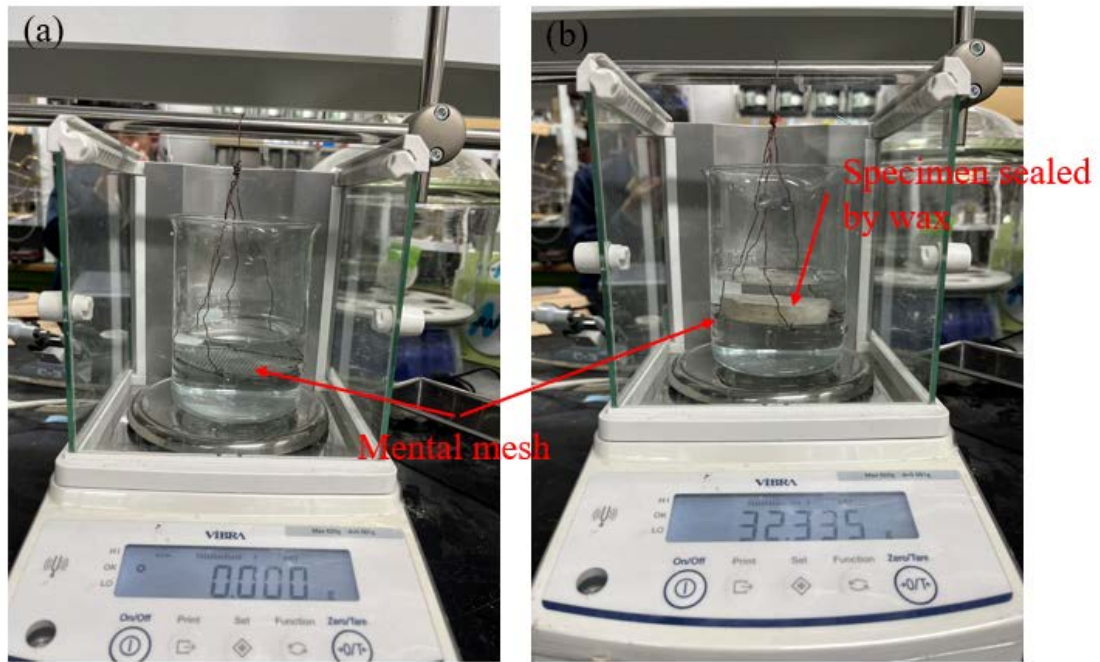


**Figure 7-4** Some specimens for shrinkage test



**Figure 7-5 Wax sealing process**

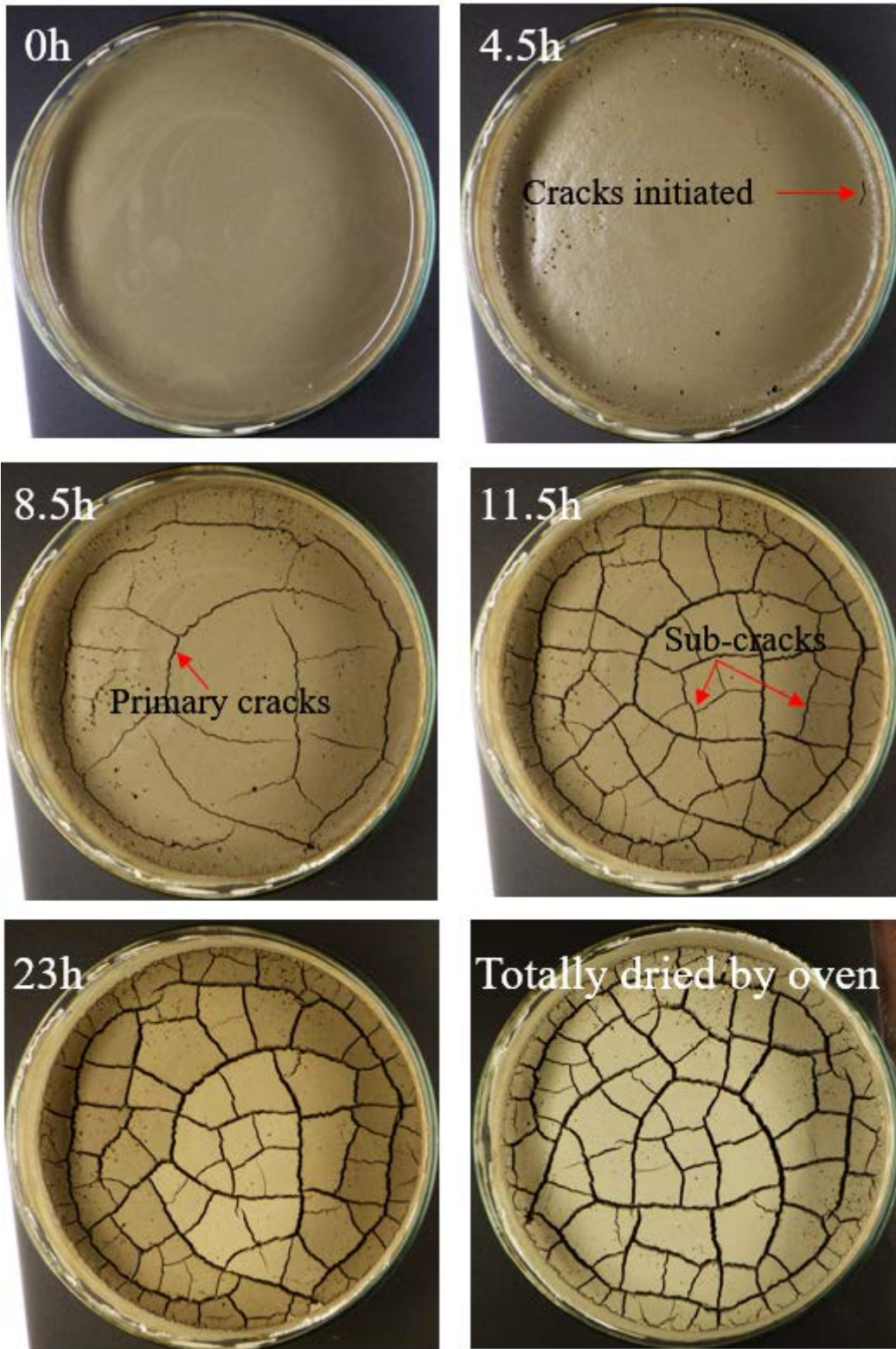
After obtaining specimens with different water content. These specimens are sealed with melted wax as shown in **Figure 7-5b**. After being sealed with wax, the specimens are waterproof, and the volume of specimens can be measured by the equipments shown in **Figure 7-6**. The specimens were immersed in distilled water contained in a beaker and then settled on a mental mesh. The specimen volume is calculated using the balance readings. It should be noted that the volume of the wax was subtracted during the calculation. The measured specimen volume was dried by the oven to determine the water content. Finally, the relationship between water content and specimen volume was obtained, which is also called soil shrinkage characteristic curve (SSCC). This method is following the JGS 0191-2009.



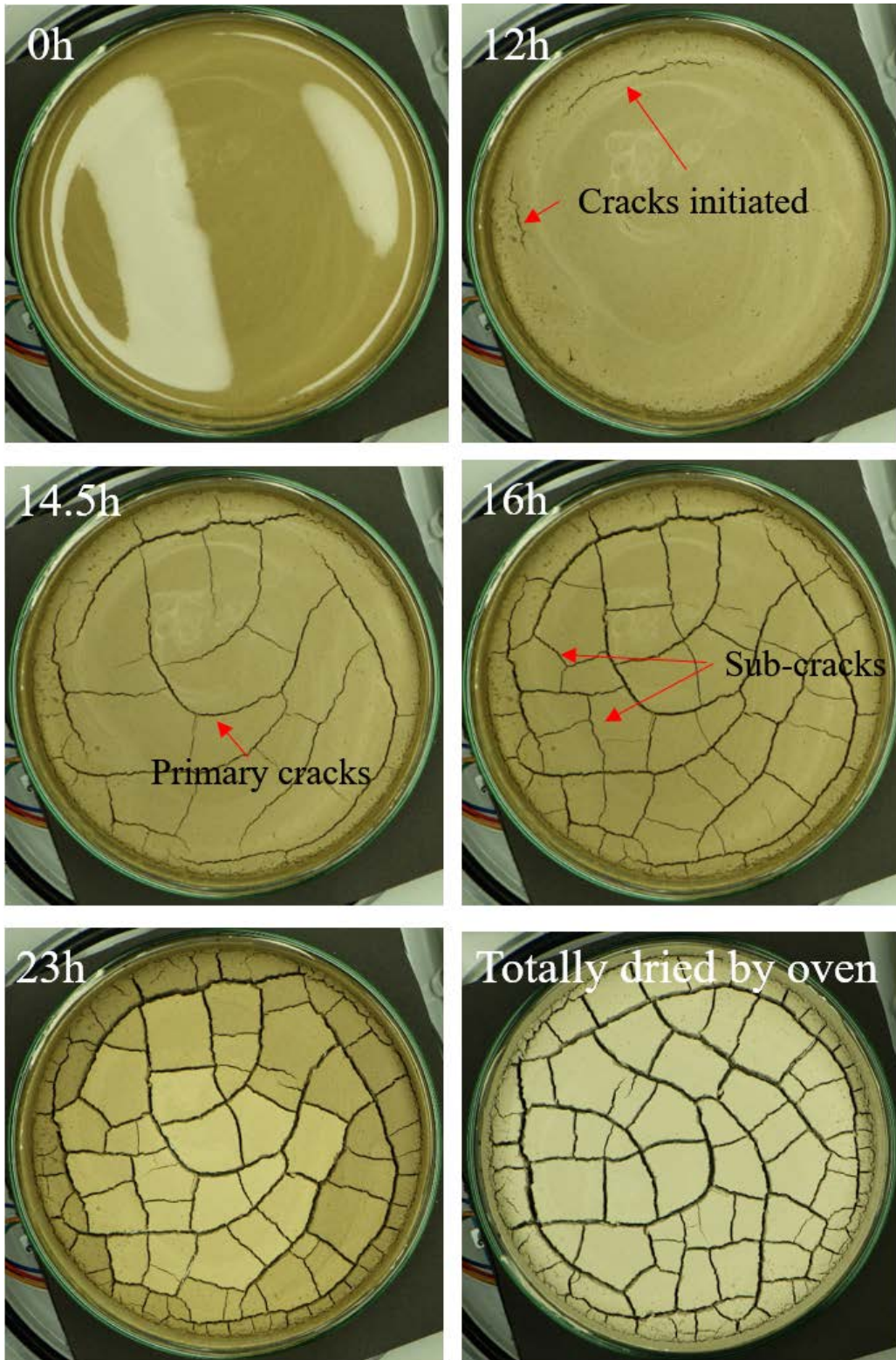
**Figure 7-6 volume measurement equipments**

## 7.2 Results and discussion

### 7.2.1 Cracking evolution of Akita mudstone with different concentration of NaCl solution

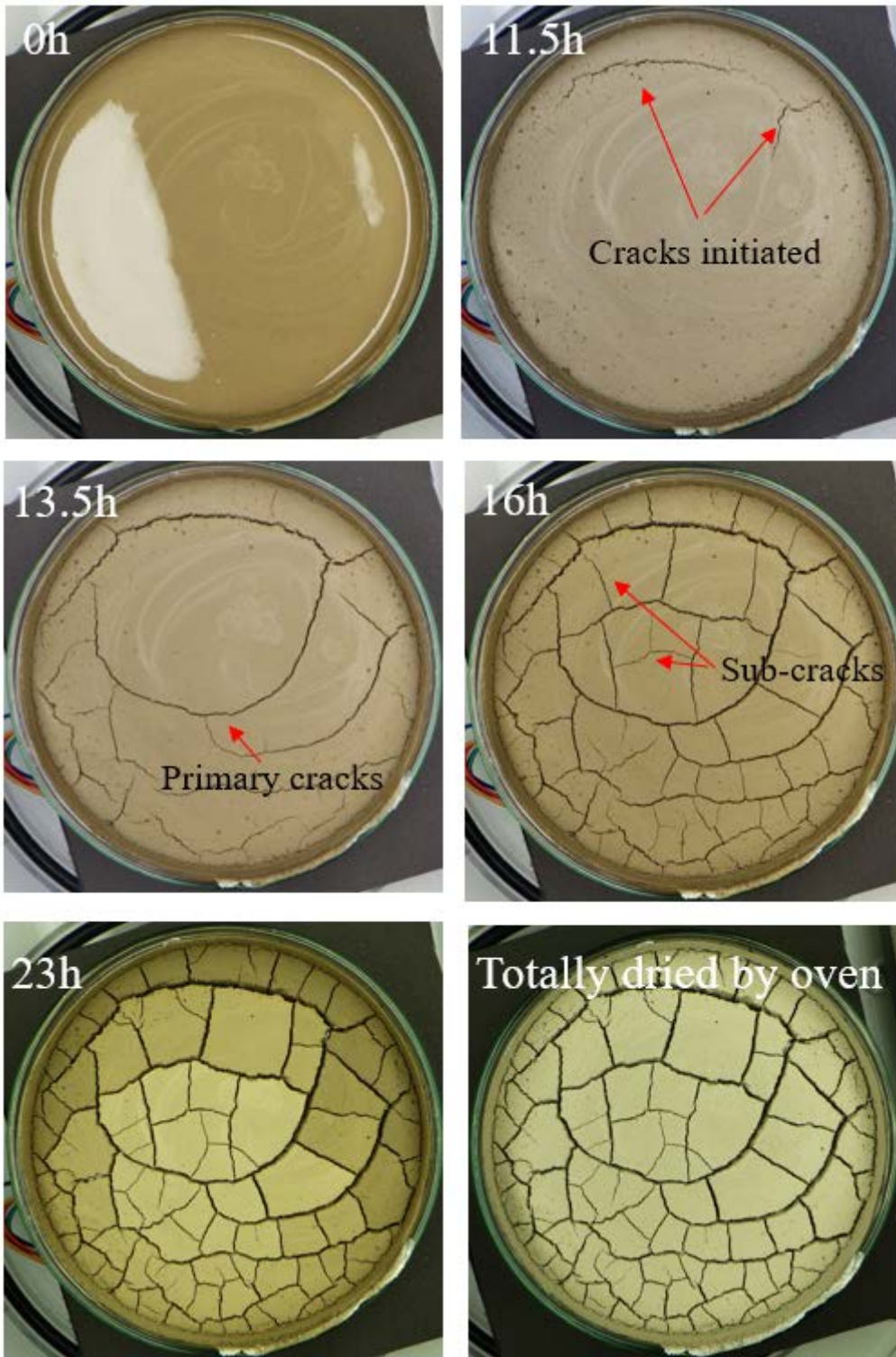


**Figure 7-7 Images for specimen during cracking with distilled water**

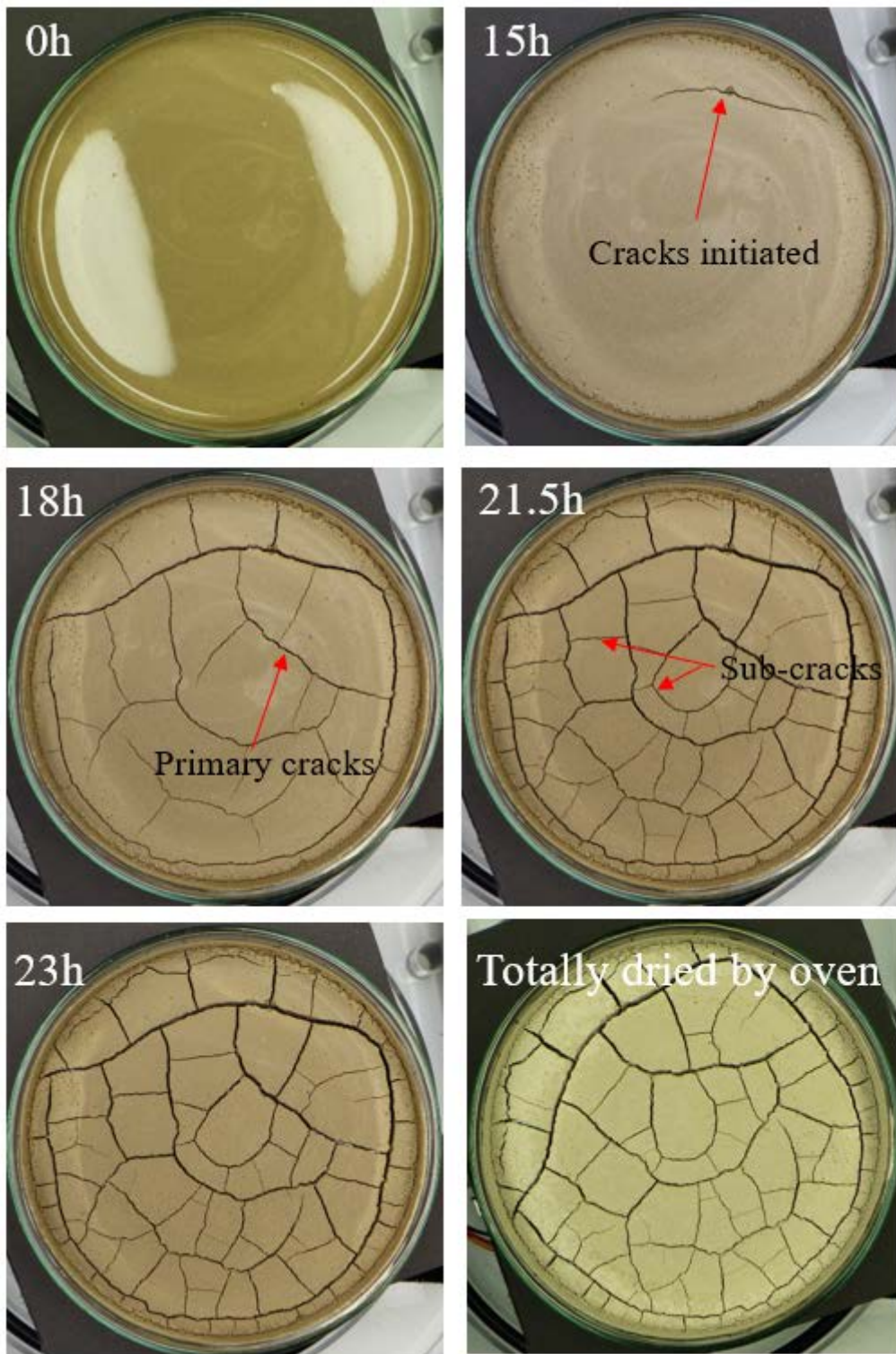


**Figure 7-8 Images for specimen during cracking with 2% NaCl solution**

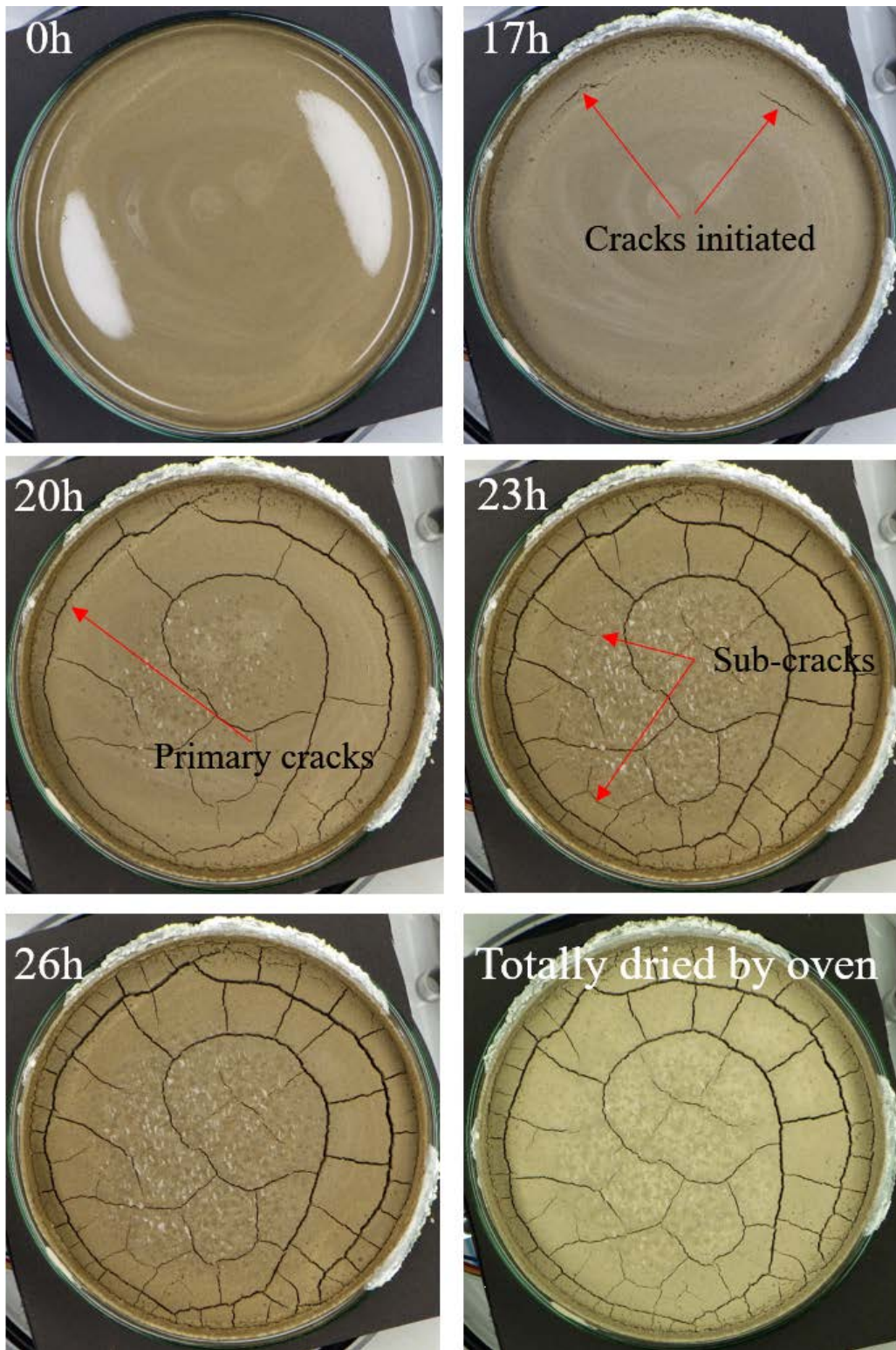




**Figure 7-9 Images for specimen during cracking with 5% NaCl solution**



**Figure 7-10 Images for specimen during cracking with 10% NaCl solution**



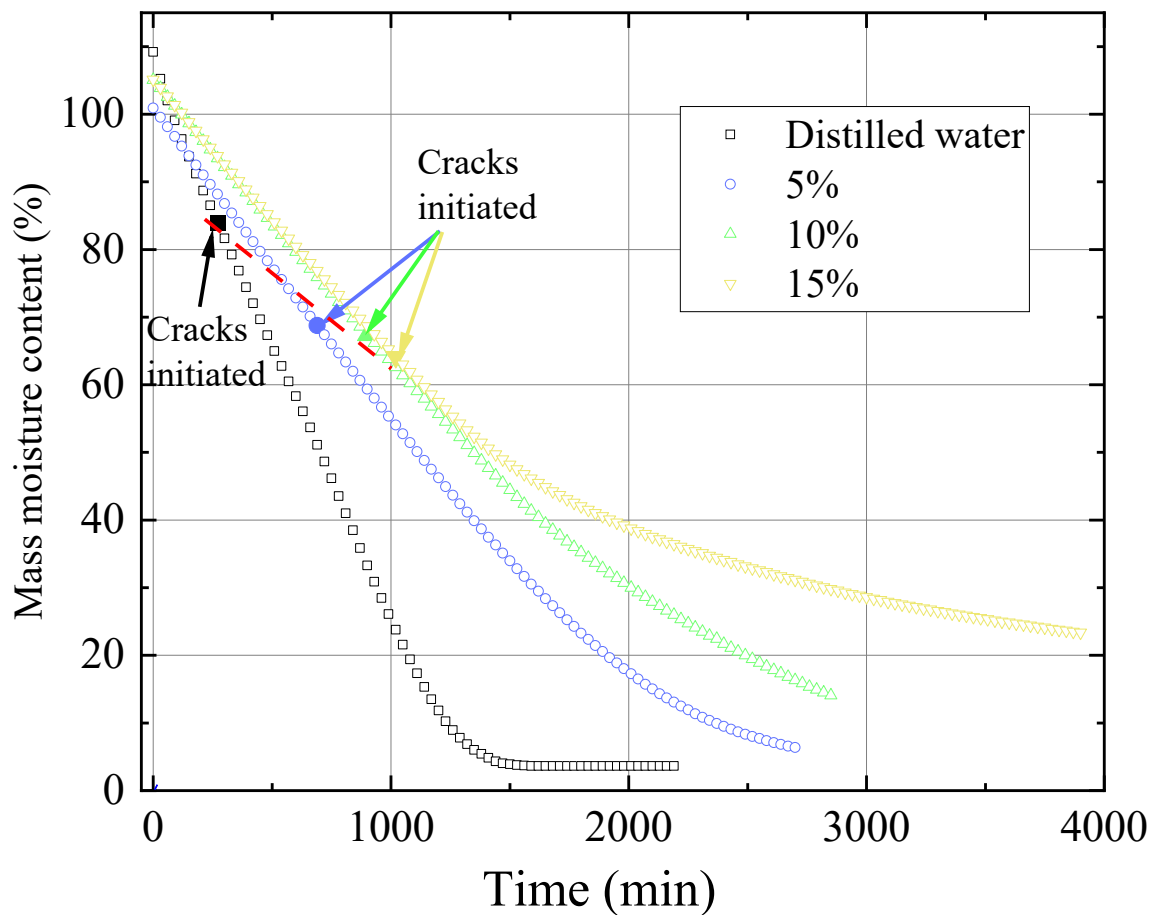
**Figure 7-11 Images for specimen during cracking with 15% NaCl solution**

**Figure 7-7 to Figure 7-11** illustrate the drying process of Akita mudstone specimens in distilled water and sodium chloride solutions of different concentrations. As time

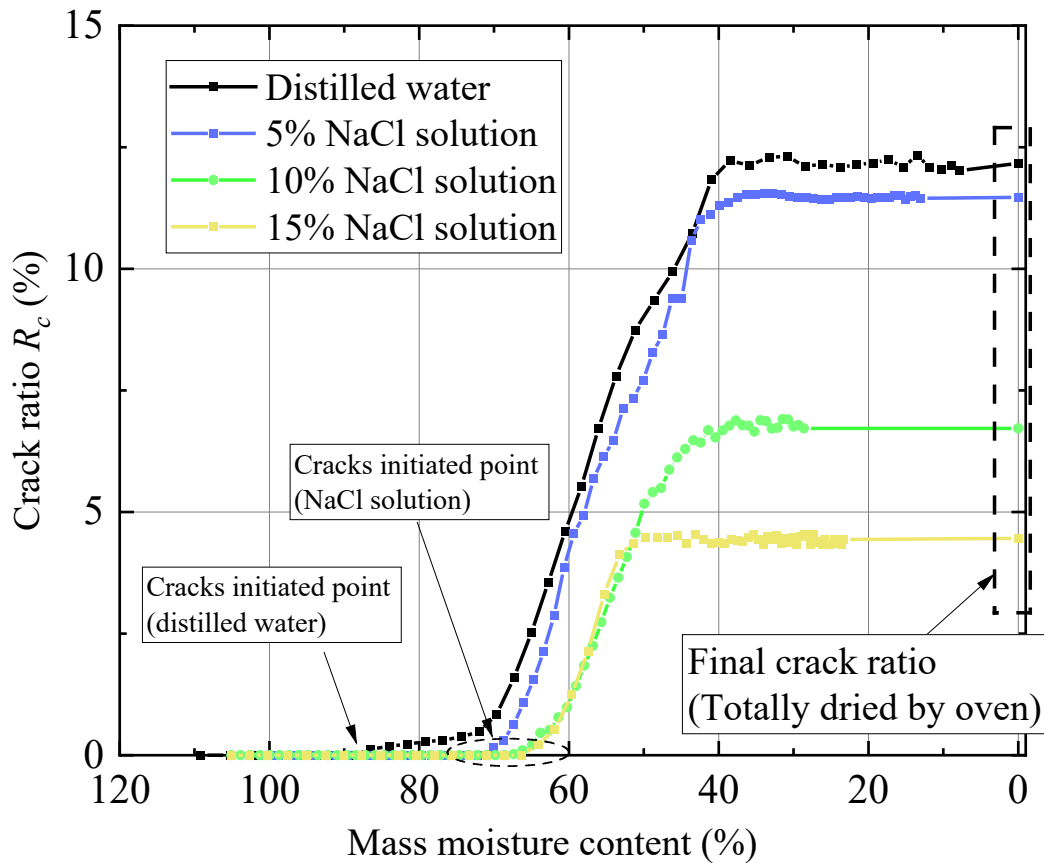
goes by, cracks gradually appear. It can be seen that when the initial cracks first appear, there are usually only one or two of them. As time goes on, the cracks increase in number and form a crack skeleton. These initially appearing larger cracks can be called primary cracks. Sub-cracks then appear, which are based on the initial cracks and rapidly expand to the area between the initial cracks within a short period of time (2-3 hours). After the sub-cracks complete their expansion, the overall crack skeleton of the sample is formed. Afterward, the cracks of the sample become slightly thicker, with almost no new cracks appearing. It is worth noting that the time of initial crack formation is delayed with the increase of salt concentration. For the samples saturated with distilled water, the first crack appears at around 4.5 hours, while for salt concentrations of 2%-5%, this time is delayed to around 12 hours. Finally, in the case of 15% concentration of sodium chloride, the time of appearance of the first crack is 17 hours. One of the reasons is as the salt concentration increases, the rate of water loss from the samples gradually decreases (**Figure 7-12**), eventually leading to a delayed appearance of initial cracks in high salt concentration samples.

The water loss rate of the samples under distilled water and different concentrations of sodium chloride is shown in **Figure 7-12**. It can be observed that for the specimen saturated with distilled water, the water loss process has already been completed at 1500 minutes. As the concentration of sodium chloride increases from 5% to 15%, the water loss rate gradually decreases. According to Raoult's law, this trend is due to the osmotic pressure gradient caused by the concentration difference between the pore water and the salt solution, which inhibits water loss from the sample. The reason for the slower water evaporation rate in salt solutions is due to the presence of dissolved ions, which increase the boiling point of the solution and decrease its vapor pressure. This means that it requires more energy to evaporate water from a salt solution compared to pure

water, and there are fewer water molecules available to escape into the air as vapor. The cracks-initiated points are marked in **Figure 7-12**. As the concentration of sodium chloride increased from 0% to 15%, the corresponding moisture content at the appearance of the first crack gradually decreased from 84% to 69%, then to 67%, and finally to 64%. This indicates that the sodium chloride solution has an inhibitory effect on the initiation of cracks.



**Figure 7-12** The water loss rate of the samples under distilled water and different concentrations of sodium chloride

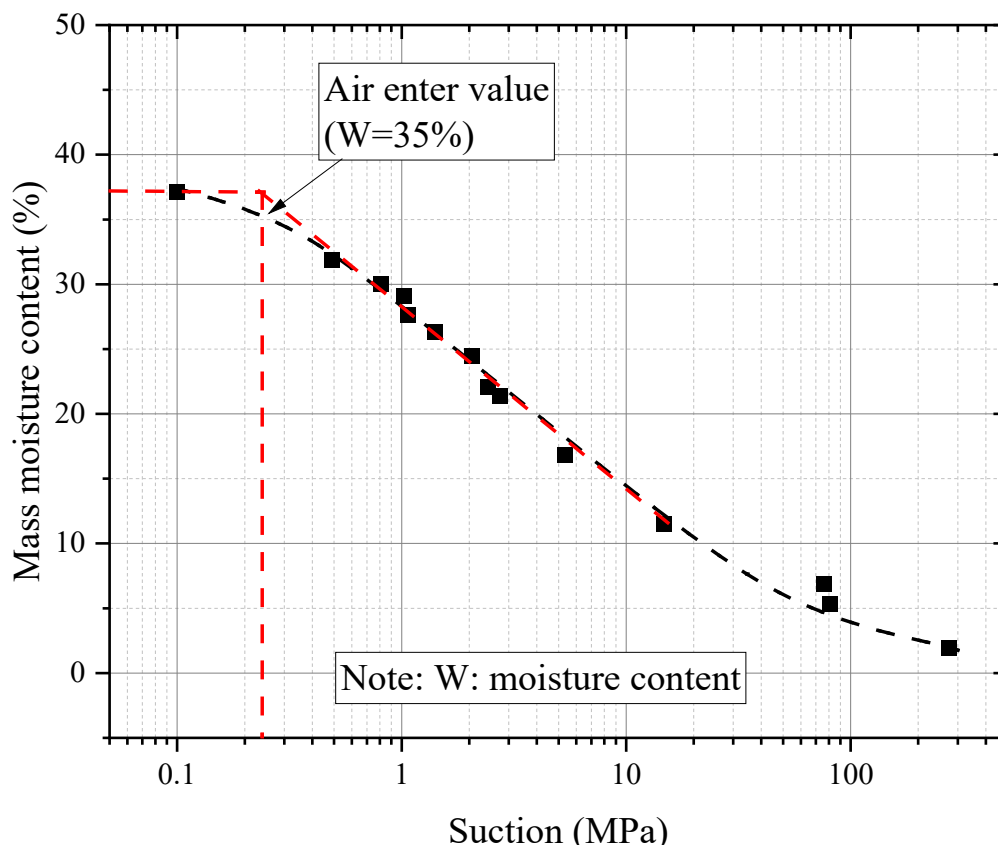


**Figure 7-13 Relationship between moisture content and crack ratios**

The relationship between crack ratio ( $R_c$ ) and moisture content at different sodium chloride concentrations is summarized in **Figure 7-13**. As mentioned earlier, as the salt concentration increases, the water content corresponding to the cracks-initiated point gradually decreases. In addition, it can be seen that for specimens with the same water content but different concentrations of sodium chloride, those with higher concentrations of sodium chloride have a lower crack ratio. The same pattern is observed for the final crack ratio when the specimen is totally dried: the higher the concentration of sodium chloride solution, the lower the final crack ratio. As the concentration of sodium chloride increased from 0% to 15%, the final crack density decreased from 12.2% to 11.5%, then to 6.7%, and finally reached its minimum value (4.5%) at a concentration of 15% sodium chloride.

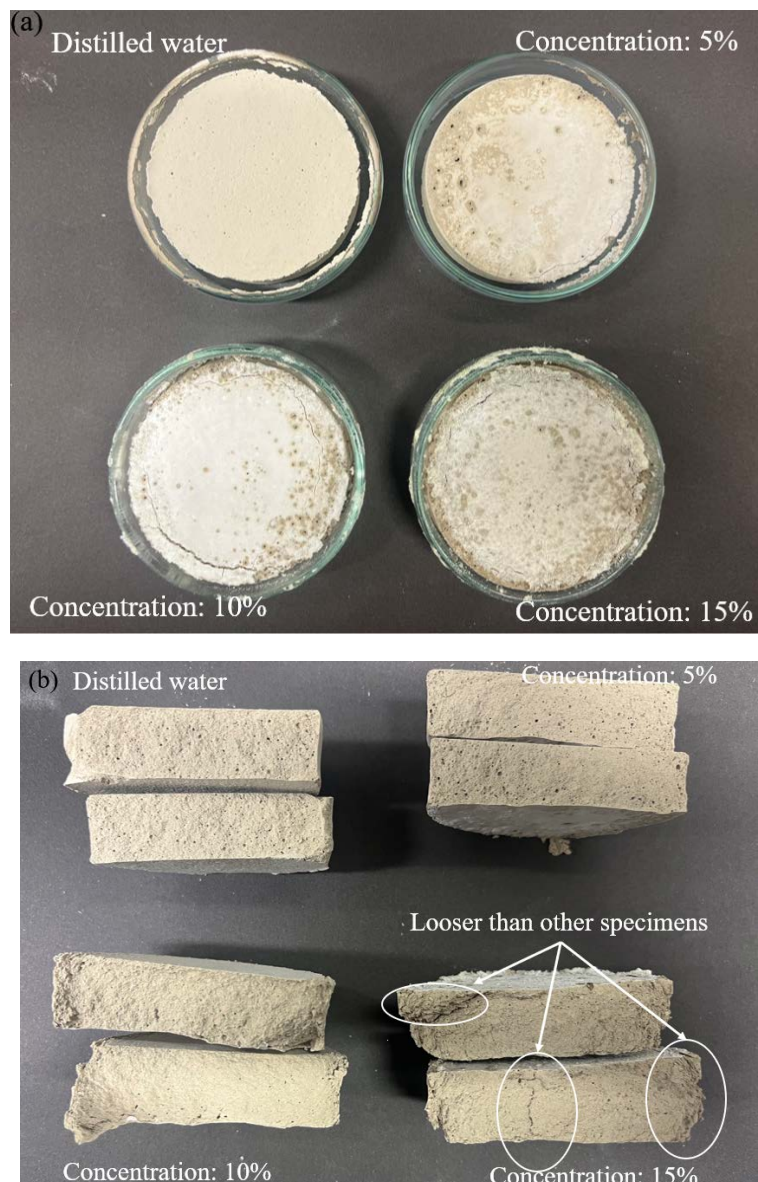
### 7.2.2 Shrinkage behavior of Akita mudstone with different concentration of NaCl

Soil-water retention curves (SWRC) of Akita mudstone can be seen in **Figure 7-14**. From the graph, it can be seen that the moisture characteristic curve shows an S-shape. As the moisture content decreases, the suction continuously increases. The air entry value (AEV) of Akita mudstone can be determined from the graph, and it is approximately 0.22 MPa (corresponding to a moisture content of 35%). Previous studies have indicated a correlation between crack evolution and air-entry value (C.-S. Tang *et al.*, 2019; Danxi *et al.*, 2023), therefore the air-entry value will be used for subsequent crack analysis.



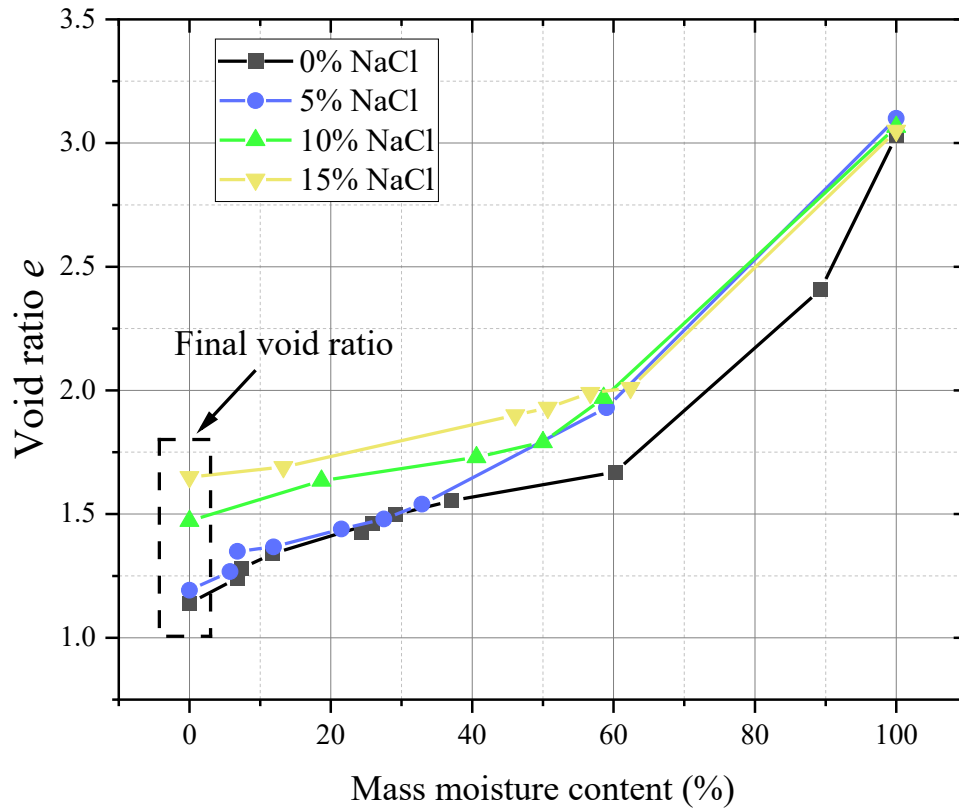
**Figure 7-14 Soil-water retention curves (SWRC) of Akita mudstone**

Pictures of totally dried specimens saturated by different concentration of sodium chloride solution for SWRC tests are shown in **Figure 7-15**. As can be seen in **Figure 7-15a**, with the increase of sodium chloride solution concentration from 0% to 15%, the spaces between the specimens and the container wall become smaller and smaller, which means that the shrinkage performance of the specimen decrease with the increase of sodium chloride concentration. Additionally, it can be in **Figure 7-15b** observed that as the concentration of sodium chloride solution increases, the structure of the sample gradually becomes looser.





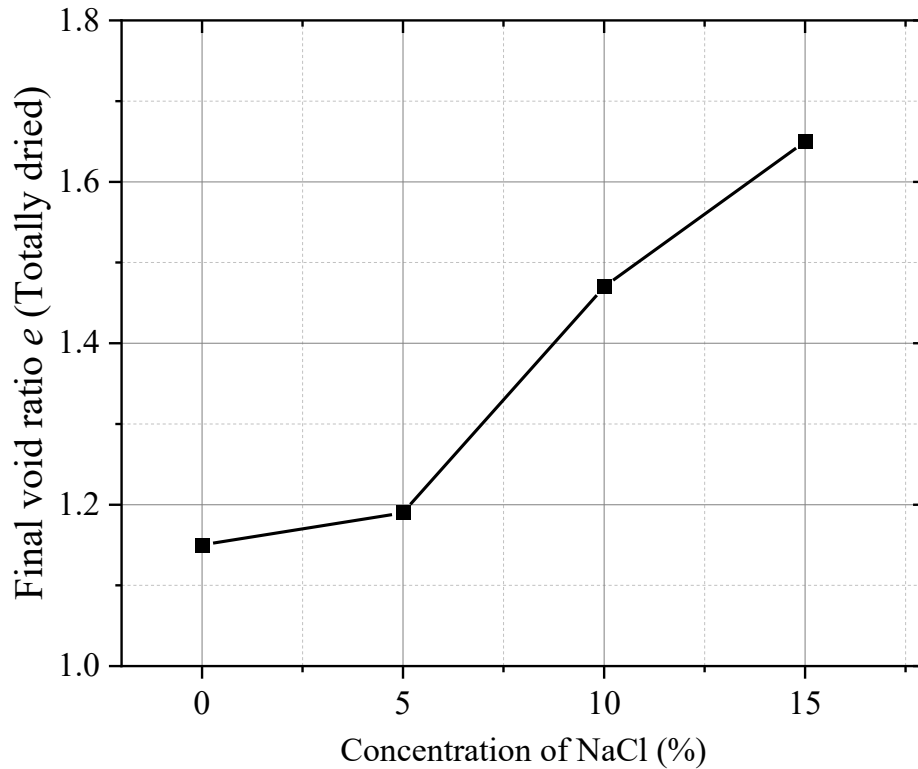
**Figure 7-15 Pictures of totally dried specimens for SSCC tests**



**Figure 7-16 Soil-water retention curves of specimens saturated by different concentration of sodium chloride solution**

**Figure 7-16** shows the Soil-water retention curves (SWRC) of specimens saturated by different concentration of sodium chloride solution. In the high moisture content range (60-100%), the void ratio ( $e$ ) of the specimen decreases rapidly as the water content decreases. In the case of low water content (0-60%), the rate of decrease in void ratio ( $e$ ) slows down as the specimen dries. In addition, with the increase of sodium chloride concentration, the shrinkage performance of the specimen gradually decreases. At the same moisture content, the void ratio of the specimen increases with the increase of sodium chloride concentration. Similarly, as the sodium chloride concentration increases from 0% to 15%, the final void ratio increases from 1.15 to 1.19, then to 1.47, and finally reaches 1.65 at a sodium chloride concentration of 15% (see **Figure 7-17**).

Cracks form due to the shear stress developing and exceeding the tensile strength of the soil during the drying process (Danxi *et al.*, 2023). This indicates that the shrinkage behavior is related to the cracking evolution, and these SSCC will be used for subsequent crack analysis.



**Figure 7-17** The relationship between final void ratio and concentration of NaCl

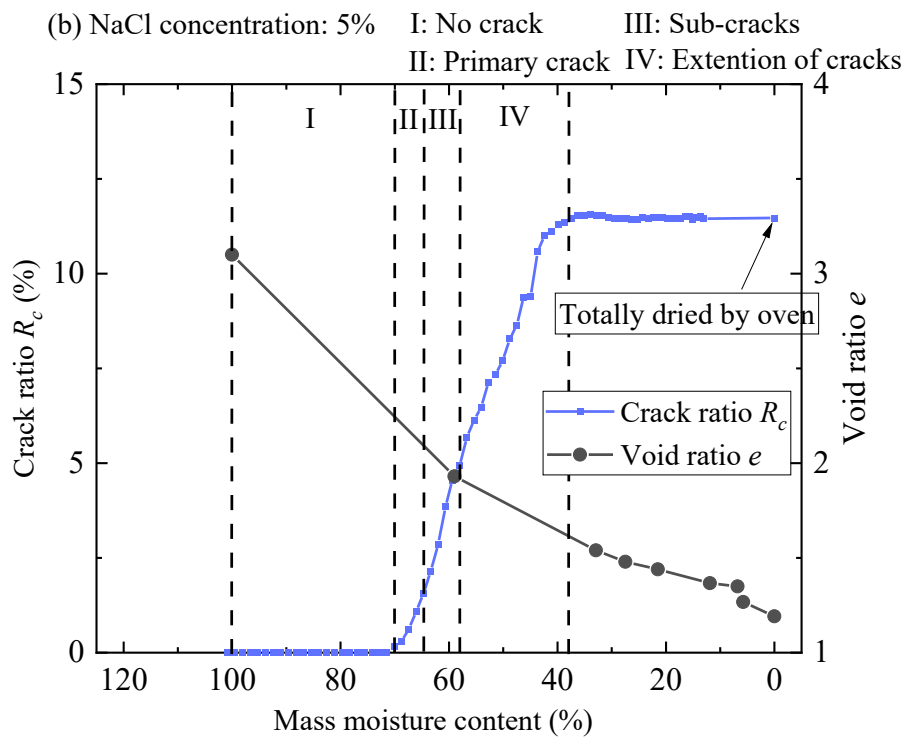
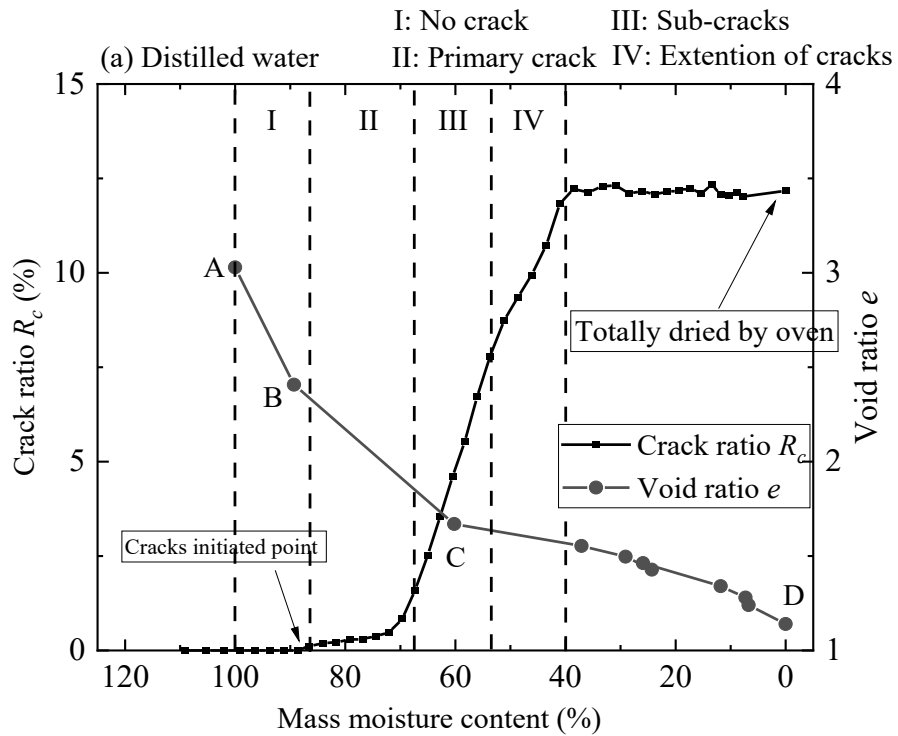
### 7.2.3 Relationship between cracking evolution and shrinkage behavior of Akita mudstone with different concentration of NaCl

The relationship between cracking evolution and shrinkage behavior are shown in **Figure 7-18**. Regardless of the concentration of sodium chloride, the initiation point of cracks often occurs in the high-water content stage where the specimen volume changes dramatically. According to the observations of the crack stages in Figure 7-7 to Figure 7-11, the cracking process can be divided into four stages: I - No crack stage; II - Primary crack stage; III - Sub-crack stage; and IV - Crack extension stage. These stages

are marked in Figure 18. It can be seen that there are significant differences in crack rate changes in these four stages. First, in the no crack stage, the crack ratio ( $R_c$ ) is 0% and the volume of specimen shrinks drastically (see Line A-B in **Figure 7-18a**). As the shrinkage behavior slows down, primary cracks are generated. During the extension of the primary cracks, the growth rate of the crack ratio gradually increases, and the shrinkage rate slightly decreases comparing with the stage I (see Line B-C in **Figure 7-18a**). Then, cracking process enters the sub-crack development stage, where the growth of the crack rate is the fastest. Subsequently, in the fourth stage (crack extension stage), there is an obvious inflection point in the growth rate of the crack rate compared to the sub-crack development stage, and the growth rate of the crack ratio slows down. Similar trends also can be seen in **Figure 7-18b, c and d**. Finally, when the cracks stop expanding, the crack ratio no longer changes. In stage III and IV, the shrinkage behavior of the specimen enters a steady shrinking stage as shown as Line C-D in **Figure 7-18a**. The air enter value (AEV) has been determined in **Figure 7-14**. However, the corresponding moisture content for AEV is approximately 35%, which is in the stage that no change in crack ratio ( $R_c$ ). In **Figure 7-18b, c and d**, it can be seen that the stages of II and III in the drying process for the saturated specimens with sodium chloride solution are significantly shorter than those for the distilled water-saturated specimens. However, the stage I is longer than that in distilled water-saturated specimens. As can be seen in **Figure 7-18d**, the sample saturated with 15% sodium chloride concentration did not show the extension of crack (stage IV). This is consistent with **Figure 7-11**, where there is no crack propagation observed after the completion of sub-crack development.

Based on previous study, cracks begin to develop before the AEV point (C. S. Tang *et al.*, 2019; Danxi *et al.*, 2023). However, in this study, the AEV occurred after the crack

evolution stage. Therefore, the AEV does not provide any meaningful information for the crack evolution in this study.



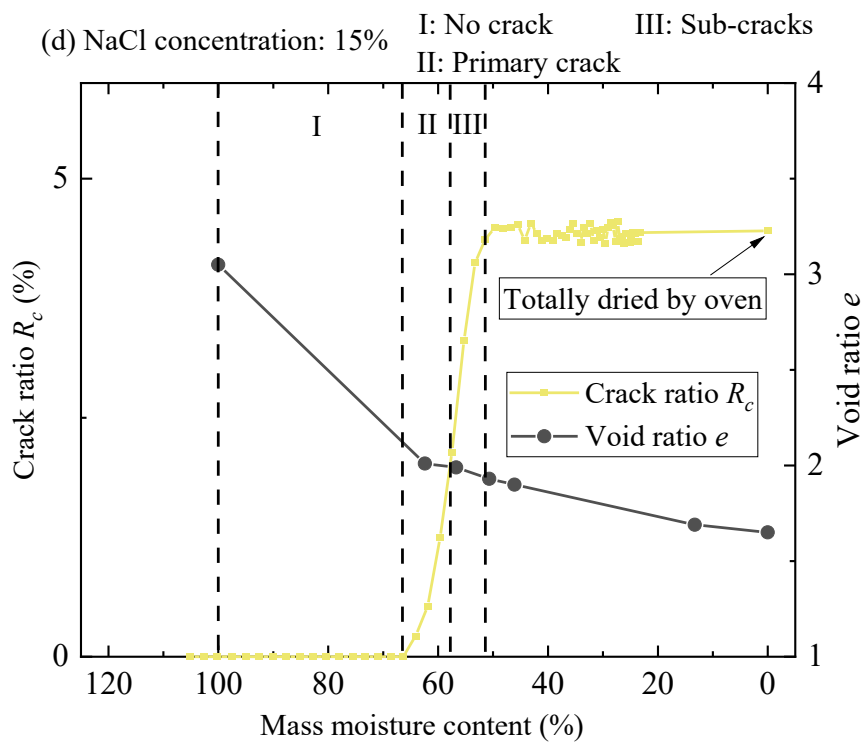
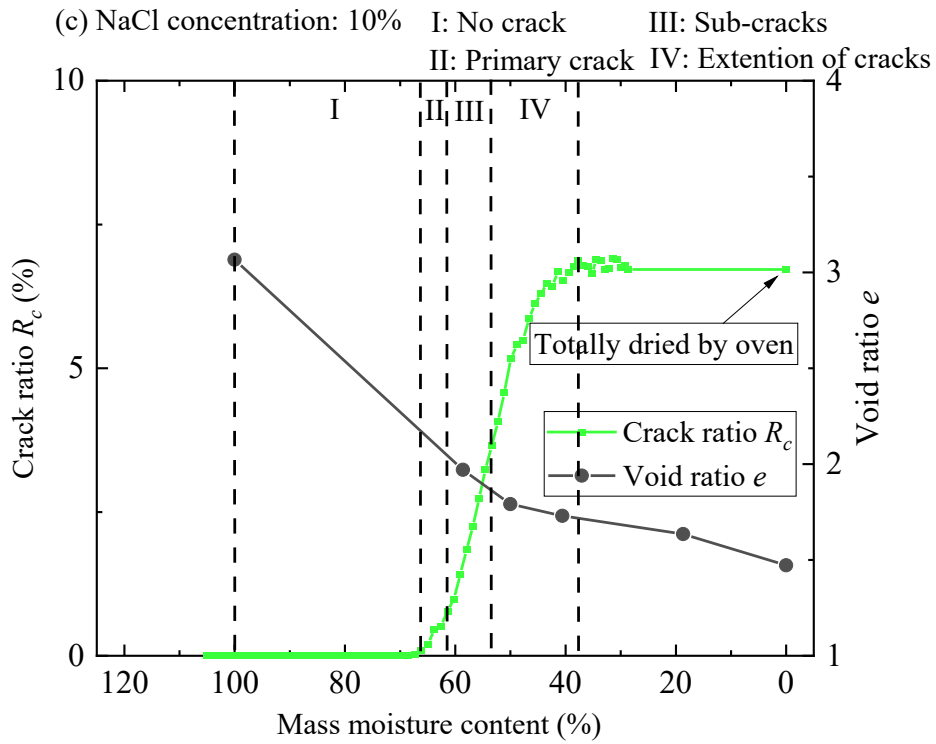
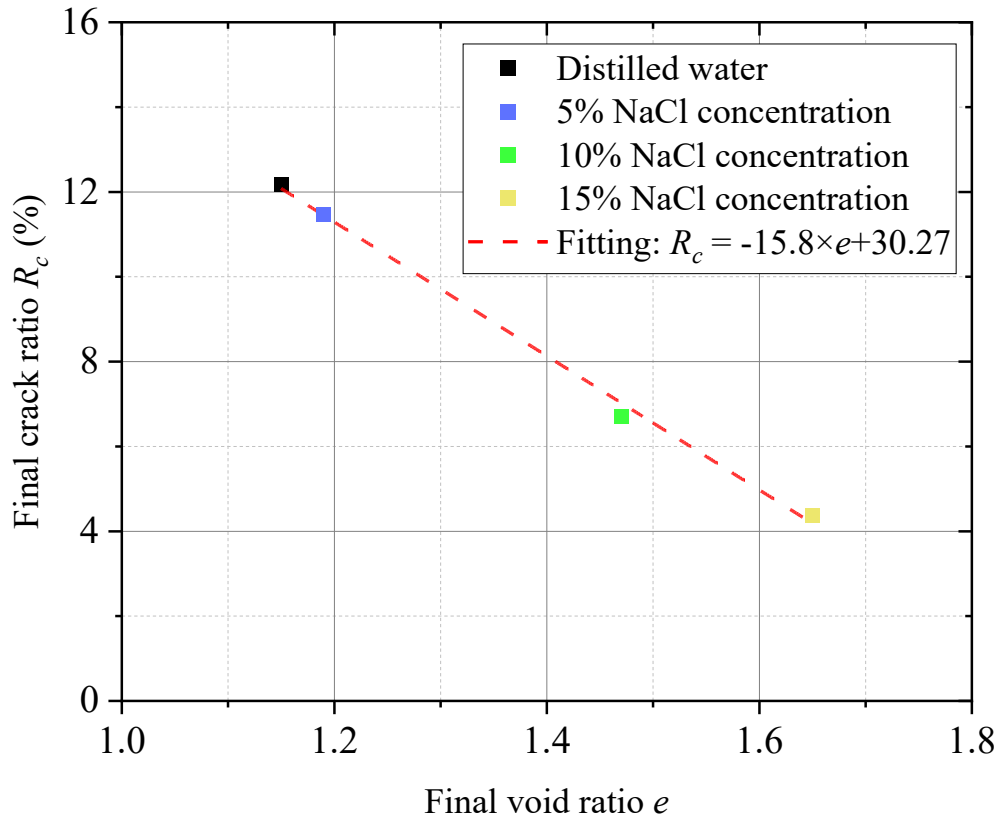


Figure 7-18 The relationship between cracking evolution and shrinkage behavior



**Figure 7-19 The relationship between final crack ratio ( $R_c$ ) and final void ratio ( $e$ )**

The relationship between final crack ratio ( $R_c$ ) in cracking tests and final void ratio ( $e$ ) in shrinkage tests are shown in **Figure 7-19**. As the final void ratio increased from 1.15 to 1.65, the final crack ratio decreased from 12.2% to 4.4%. Furthermore, there was a linear relationship between the final void ratio and the final crack ratio, which indicates that the sodium chloride solution weakened the development of cracks by suppressing the shrinkage of the specimen.

### Conclusions

In Akita mudstone, the sodium chloride solution weakened the development of cracks by suppressing the shrinkage of the specimen. The evolution of cracks has a strong correlation with the shrinkage characteristics of the soil, and as the shrinkage capacity

of the soil decreases, the final crack rate also linearly decreases. In addition, the evolution of cracks can be divided into four stages, namely Stage I - No crack stage; Stage II - Primary crack stage; Stage III - Sub-crack stage; and Stage IV - Crack extension stage. Moreover, these stages have distinct characteristic boundary points. The saturation of specimens by sodium chloride solution significantly shortened Stages II and III, and prolonged Stage I.

**Chapter 8. SLAKING TESTS ON  
MUDSTONE AND PORE AND PARTICLE  
ORIENTATION OF COMPACTED BLACK  
MUDSTONE**



## 8.1 Testing overview

Information of specimens for different tests are shown in **Figure 8-1**. In this study, natural black mudstone, oven-dried natural black mudstone and similar Terashima mudstones were used for slaking tests. Additionally, oven-dried remolded black mudstone with three different dry densities (target: 1.60; 1.80 and 2.00 g/cm<sup>3</sup>) were also used for slaking tests. Finally, specimens with similar dry densities that were oven-dried and then were used for SEM tests. Details of the slaking test and SEM tests will be presented later in the text.

**Table 8-1 Information of specimens for different tests**

Specimens	Condition	Water content (%)	Weight (g)	Dry density $\rho$ (g/cm <sup>3</sup> )	Test
Black mudstone	Natural	4.2	9.98	-	Slaking test
Black mudstone	Natural; Dried	0	9.80	-	Slaking test
Terashima mudstone	Natural	9.9	9.95	-	Slaking test
Terashima mudstone	Natural; Dried	0	10.03	-	Slaking test
Black mudstone	Remodeled; Dried	0	10.23	1.66	Slaking test
Black mudstone	Remodeled; Dried	0	11.13	1.81	Slaking test
Black mudstone	Remodeled; Dried	0	12.34	2.01	Slaking test
Black mudstone	Remodeled; Dried	0	5.27	1.60	SEM test
Black mudstone	Remodeled; Dried	0	5.85	1.84	SEM test
Black mudstone	Remodeled; Dried	0	6.26	1.96	SEM test

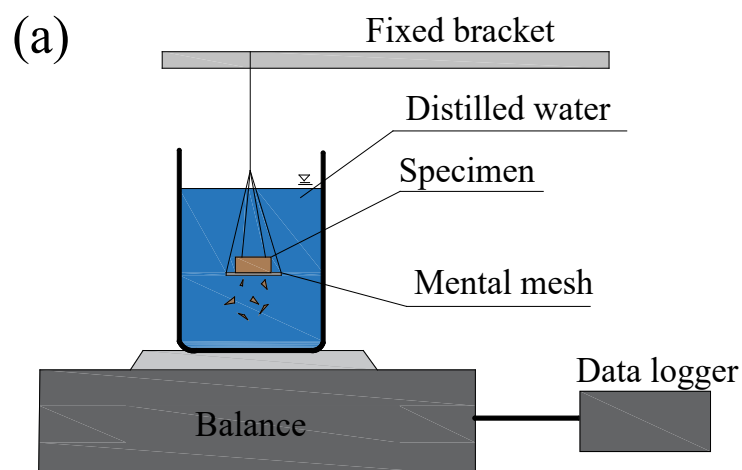
To quantify the slaking behavior of black mudstone and Terashima mudstone, a slaking equipments (see **Figure 8-1**) was employed. At the beginning of the test, the specimen was immersed in distilled water, and as the slaking proceeded, the soil specimen

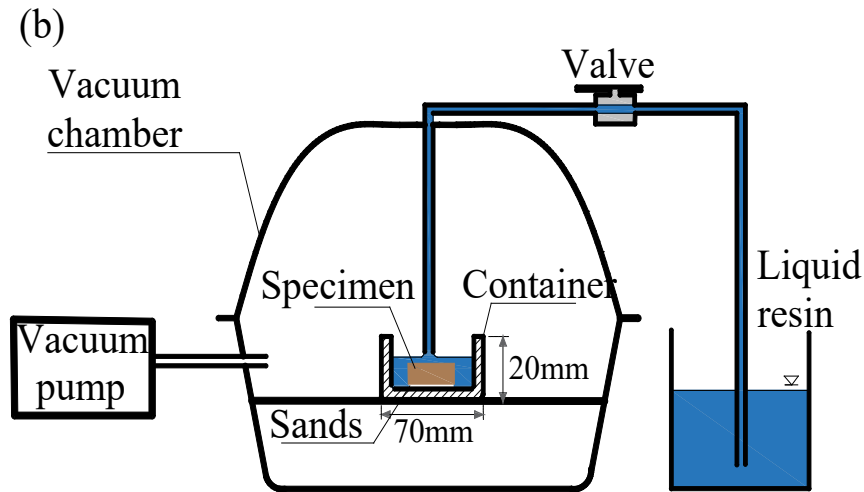
gradually peeled off and sank to the bottom. The weight measured by the balance continuously increased during this process, serving as a standard for quantitatively evaluating the slaking process. It should be noted that the metal mesh size was a square hole with a side length of 5.5mm. The measured weight was converted into the slaking ratio for studying the slaking process, using the following calculation formula:

$$R_s = \frac{m - m_{initial}}{m_{final} - m_{initial}} \times 100\% \quad (8-1)$$

Where  $m$  is weight measured by the balance;  $m_{initial}$  is the weight measured when the specimen is immersed in distilled water;  $m_{final}$  is the weight measured when the slaking process is finished.

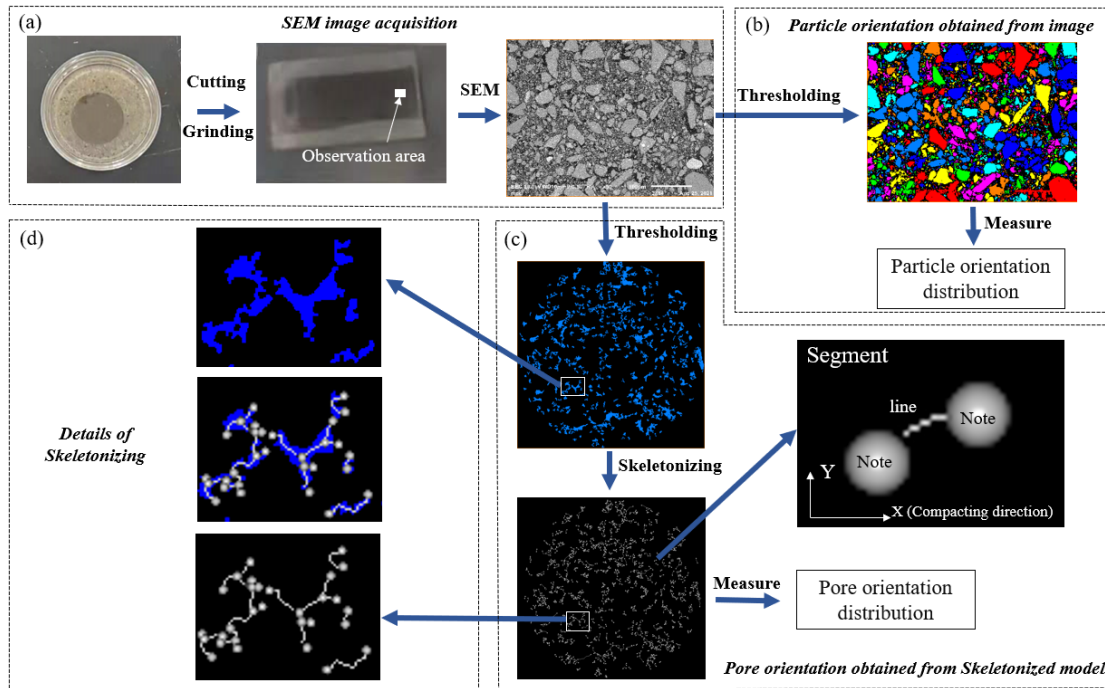
It is worth noting that sometimes the final weight of the specimen may not be equal to its original weight due to the presence of coarse particles that cannot pass through the mental mesh. However, this does not affect the accuracy of the results as it can be observed that the coarse particles have completed disintegrated after test.





**Figure 8-1 Equipments used in this study: (a) Slaking test instrument (b) Vacuum chamber**

To quantitatively study the pore size distribution, particle and pore orientation, compacted specimens with different dry densities were treated with resin. To prevent damage from entrapped air, a vacuum chamber (as shown in **Figure 8-1b**) was utilized during treatment. The compacted specimen was placed in a container with some sand in the vacuum chamber, and vacuum was maintained for 10 minutes with the valve closed. After that, the valve connecting to the liquid resin was opened to allow the resin to enter the container at a uniform speed. Sufficient liquid resin was injected into the container before closing the valve. Finally, the sample was removed from the vacuum chamber and prepared for SEM tests.



**Figure 8-2 Typical image processing and data acquisition: (a) SEM image acquisition; (b) particle orientation obtained from image; (c) pore orientation obtained from skeletonized model; and (d) details of skeletonizing.**

The preparations for SEM tests and image processes can be seen in **Figure 8-2**. Specimen treated by resin were cut and the area close to the cross-section center of the specimen was observed using SEM (see **Figure 8-2a**). The original SEM images have some noise, which affects the quantitative analysis. Some common image processes including Median Filter, Opening, and Closing were applied before Thresholding process (Danxi *et al.*, 2023). After these common processes, different thresholding values were performed on the SEM image for pores/particles extraction. Two parts were recognized from SEM image by Thresholding process as shown in **Figure 8-2b** and **c**: one part is the particle, and the other part is recognized as pores. The value of Thresholding is determined by artificial vision (Hu *et al.*, 2018). The Orientation of the particle in degrees  $[-90^\circ, +90^\circ]$  is computed with the inertia moments. However, due to the complex structure of pores, it is not appropriate to determine the pore orientation by inertia moments. Thus, skeletonization was carried out to create the skeleton of pores

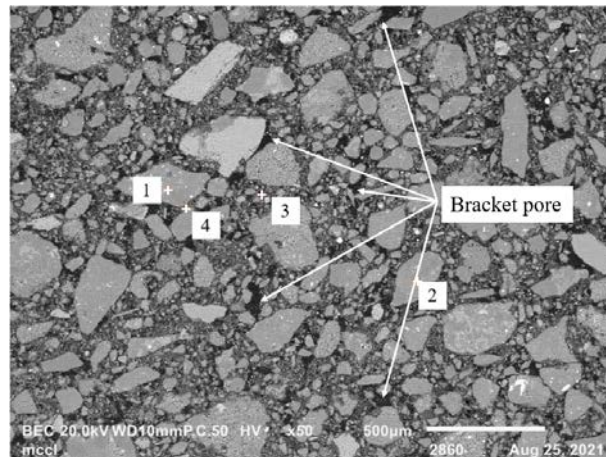
represented by a line and two nodes, where one line and two ending nodes are called a segment (**Figure 8-2c**). The length and orientation of skeleton were determined by coordinates of two ending nodes as shown in **Figure 8-2c**. Details of skeletonizing can be seen in **Figure 8-2d** and the skeleton can represent the orientation of the pores. Thus, skeleton orientations weighted by skeleton length were computed for pore orientation analysis. Details of the calculation method of orientation distribution will be introduced in section 8.2.4. Since the edges of the image gather skeletons, rectangular images result in an increase in the gravity of the pores in the side length direction in the result. Therefore, the images used for pore orientation analysis in this experiment are sheared into circle images. Finally, pore and particle information were analyzed to obtain pore and particle orientation distribution characteristics. In addition to pore and particle orientation, pore size distribution was also extracted and statistically analyzed in **Figure 8-2c**.

## 8.2 Results and discussion

### 8.2.1 Soil structure and EDS analysis

In this study, the structure of compacted crushed mudstone was analyzed by SEM and EDS, which will be the basis of subsequent analysis. The SEM image of specimen after grinding can be seen in **Figure 8-3**, there are lots of hard large particles distributed in the specimen and the bracket pores can be seen between large particles. It can be seen from the EDS results that the silicon content of the large particles (Point 1 and 2 in **Table 8-2**) is higher than that of the regions between large particles (Point 3 and 4 in **Table 8-2**), while the clay element content of the fine particles intercalated between the large particles is higher than the large particles. Thus, it is speculated that the large

particles should be quartz particles. It should be noted that resin was used in the preparation of the specimen and therefore C and O elements were excluded from the EDS test. In summary, the structure of compacted crushed mudstone is composed of large particles, bracket pores and clay between large particles.



**Figure 8-3 SEM image of compacted crushed mudstone specimen**

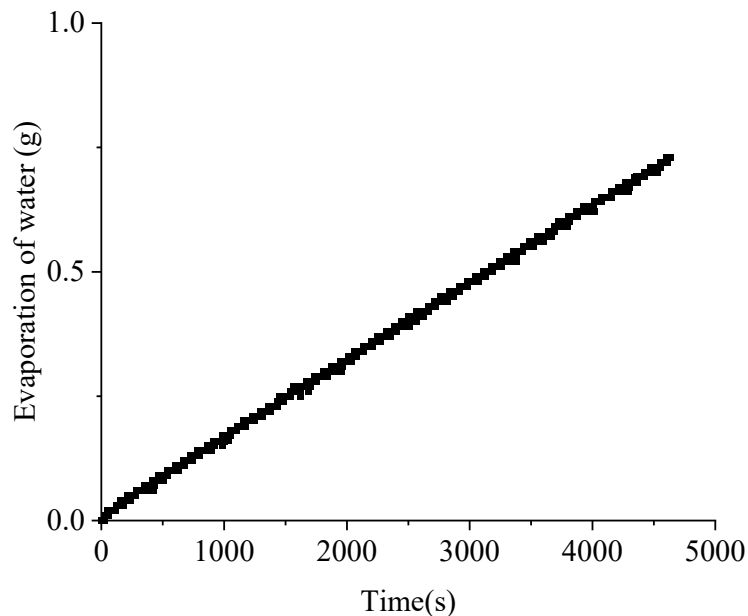
**Table 8-2 Results of EDS analysis**

Points	Si (mass%)	Al (mass%)	Mg (mass%)	Na (mass%)	Ca (mass%)
1	87.45	10.68	0.99	0.88	-
2	99.86	-	0.07	-	0.07
3	69.70	23.66	6.64	-	-
4	74.13	18.89	2.37	2.93	1.68

### 8.2.2 Slaking tests on natural mudstone

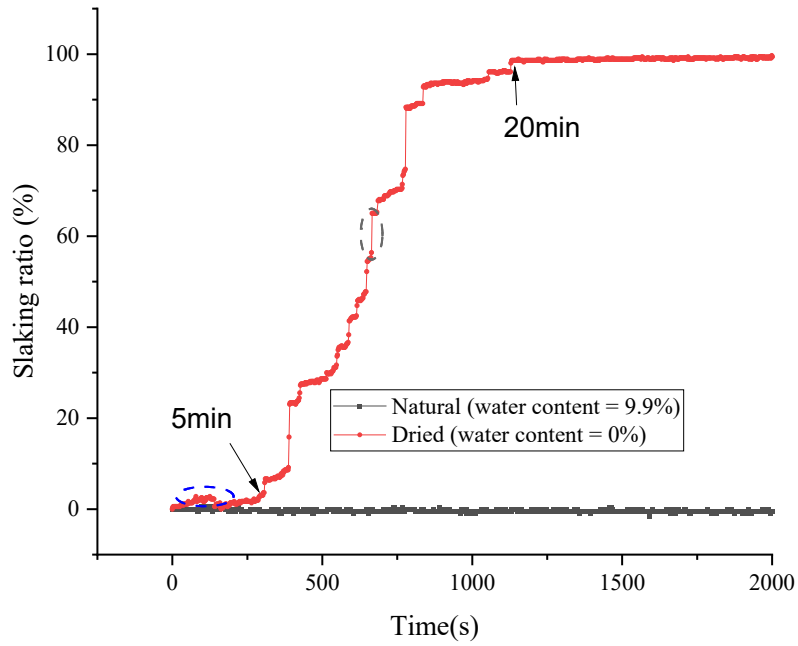
Two types of natural mudstone, including black mudstone and Terashima mudstone, were tested using the slaking test instrument shown in **Figure 8-1a**. The Terashima mudstone has a higher dry density, and its pores are almost invisible. However, the black mudstone is porous. Prior to conducting the experiment, water evaporation was measured (see **Figure 8-4**). It should be noted that subsequent test results were

calibrated using this curve. Additionally, please note that there were a few grammatical errors in the original text, which I have corrected.

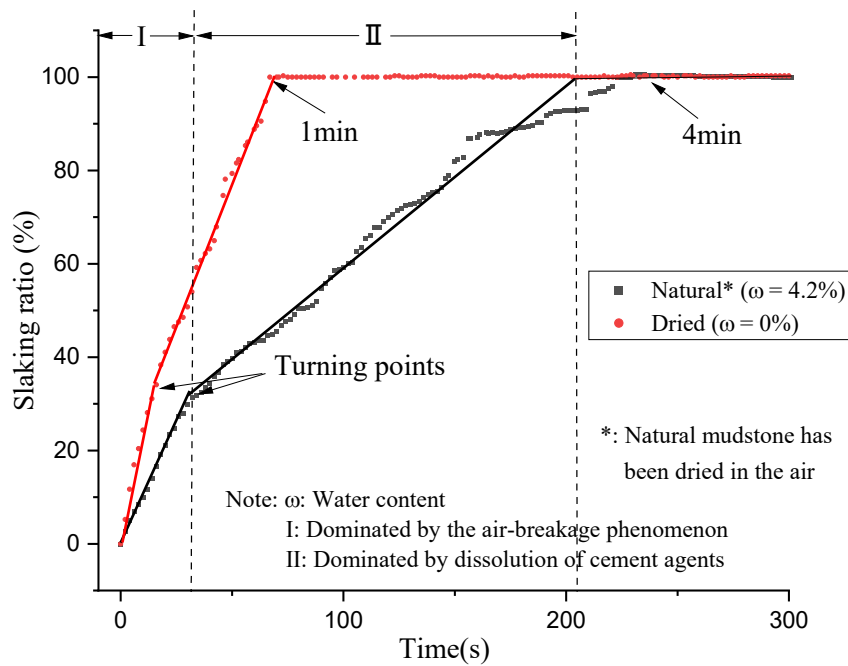


**Figure 8-4 Evaporation of water**

**Figure 8-5** presents the results of slaking tests conducted on natural and dried natural Terashima mudstone. It is interesting to note that natural Terashima mudstone, with a water content of 9.9%, did not exhibit any slaking properties during the test, maintaining a slaking ratio of 0% for more than 40 minutes. In contrast, the dried Terashima mudstone showed complete slaking phenomenon in 20 minutes. The curve had an S-shape, with the slaking ratio fluctuating around 0% during the first 5 minutes of the test. The specimen did not exhibit much change except for a series of small bubbles emerging from its surface. A decrease in the blue circle was observed due to air escaping from the dried soil. The low permeability resulting from low porosity causes dissolution of cement agents and differential swelling, leading to the fluctuation in the first 5 minutes of the test. With the infiltration of water, the dissolution of cement agents and differential swelling of the soil gradually caused slaking phenomenon.



**Figure 8-5 Slaking curves of Terashima mudstone**

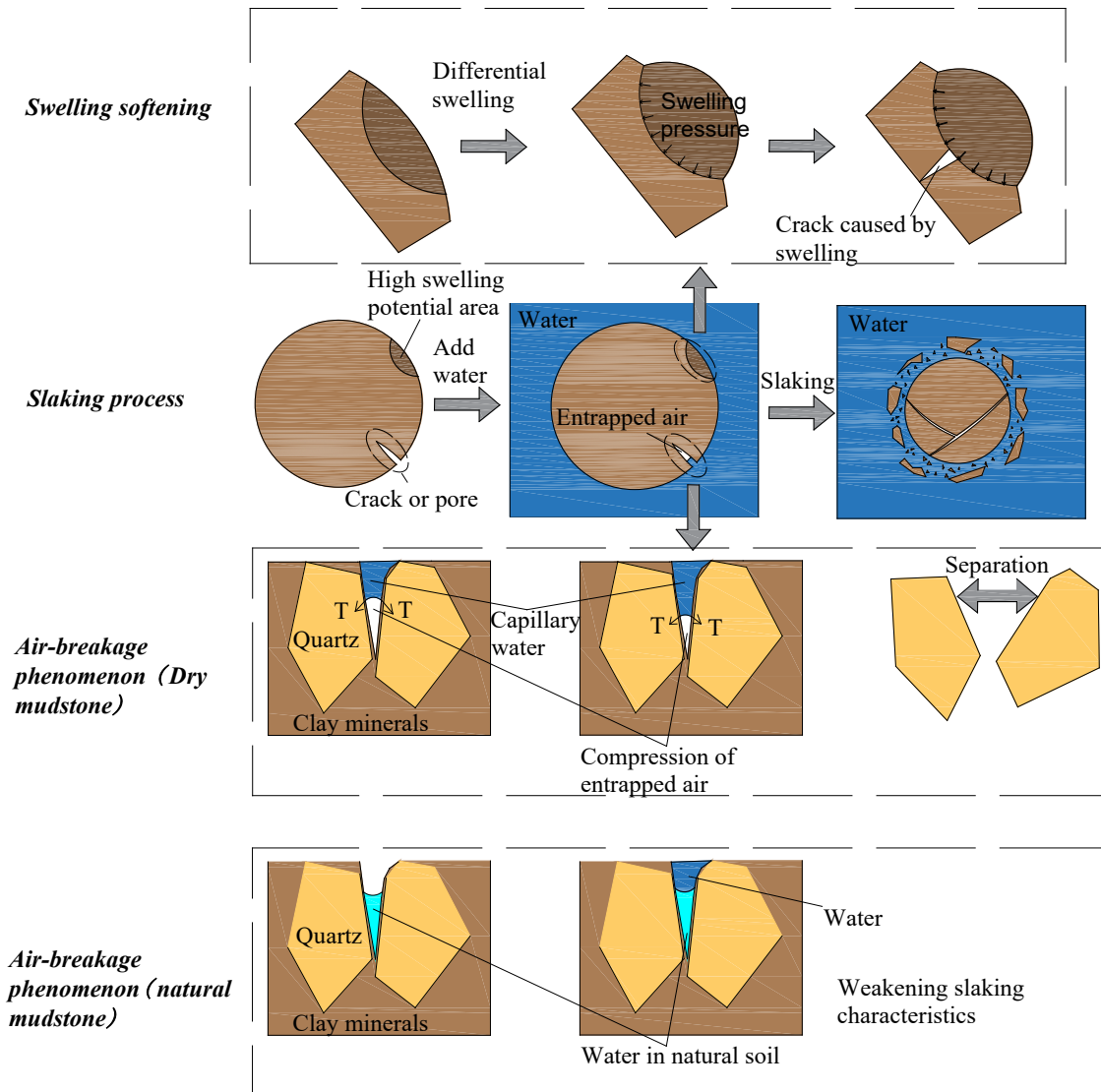


**Figure 8-6 Slaking curves of black mudstone**

**Figure 8-6** presents the results of the slaking tests conducted on natural and dried black mudstone. Similar to Terashima mudstone, the dried specimen showed a stronger



slaking behavior compared to the moist specimen. The dried specimen disintegrated completely in just one minute, while the specimen with 4.2% water content disintegrated completely in four minutes. Unlike Terashima mudstone, black mudstone exhibited rapid slaking behavior in the first few tens of seconds, followed by an obvious turning point. After the turning point, the slaking behavior slowed down until complete slaking. The slaking process in the first few tens of seconds was accompanied by the production of a large number of bubbles, indicating air-breakage phenomenon as the possible reason for the rapid slaking behavior in region I. When the specimen became completely saturated with water, the slaking behavior slowed down due to the cessation of the air-breakage phenomenon. The slaking behavior in region II was mainly caused by the dissolution of cement agents, which was also present in region I but had little influence because the part inside the specimen was not in contact with water. The rapid slaking behavior of the dried specimen in region II will be further explained later.



**Figure 8-7 Process of slaking**

As previously mentioned, drying treatment can promote the slaking behavior of undisturbed specimens. The process of slaking can be observed in **Figure 8-7**, which illustrates two reasons for slaking: swelling softening and air-breakage phenomenon. Dissolution of cement agents is not discussed here, but the structural damage caused by swelling softening and air-breakage phenomenon promotes contact between water and soil, thus promoting the process of cement agent dissolution. The differential swelling pressure damages the mudstone structure and results in slaking when water penetrates

the soil in the region of high expansion potential. For black mudstone, this mechanism makes a smaller contribution to slaking due to its weak swelling potential.

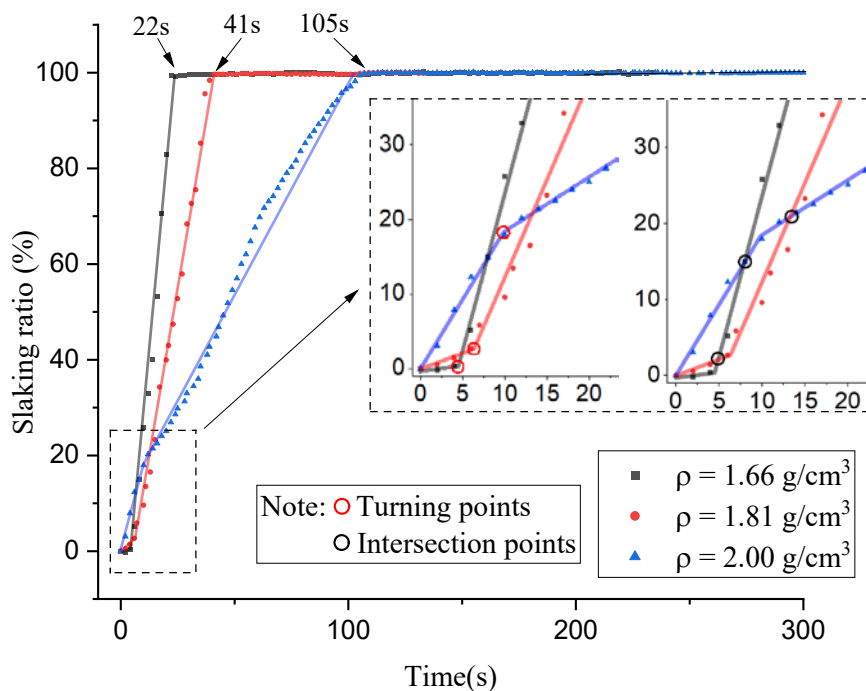
In dried mudstone, pore water has been removed, and therefore, entrapped air is compressed by the intruding water due to capillary action. The pressure from the entrapped air separates silica particles. During the slaking process, air-breakage phenomenon occurs at the moment when the soil contacts water, while the other two slaking mechanisms require water infiltration. As seen in the air-breakage phenomenon of natural mudstone, for soil with a certain moisture content, pore water exists in some pores before slaking behavior. Distilled water cannot invade these pores and form entrapped air due to the presence of original pore water. Therefore, pore water existing in some pores weakens the air-breakage phenomenon and results in weaker slaking behavior.

### 8.2.3 Slaking tests on remolded mudstone

To further investigate the relationship between pore structure and air-breakage phenomenon in region I of **Figure 8-6**, slaking tests were conducted on three remolded black mudstone specimens with varying dry densities. The results are presented in **Figure 8-8**.

The remolded black mudstone specimen with a dry density of  $\rho=1.66\text{g/cm}^3$  achieved complete slaking in 22 seconds, while the specimens with medium ( $\rho=1.81\text{g/cm}^3$ ) and maximum ( $\rho=2.00\text{g/cm}^3$ ) dry densities completed the slaking behavior in 41 seconds and 105 seconds, respectively. This observation is reasonable since soil particles with higher dry density exhibit greater adhesion. Furthermore, soils with lower dry density

possess better permeability and larger soil-water contact areas (more pores), leading to faster development of slaking behavior.



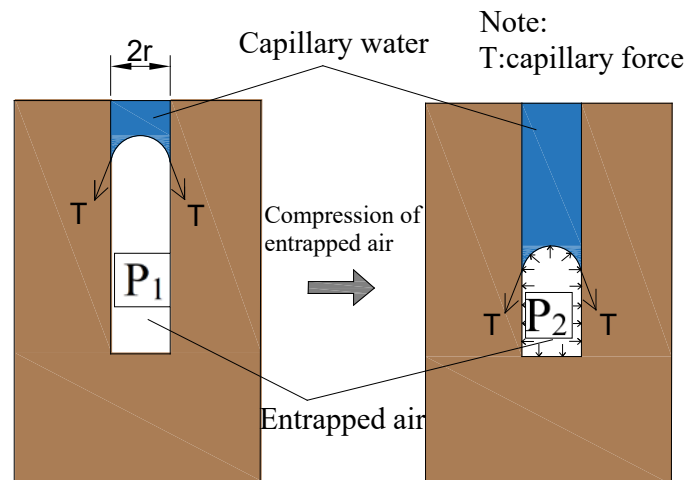
**Figure 8-8 Slaking curves of black mudstone**

However, an interesting phenomenon is observed in the initial 20 seconds of the slaking behavior. As depicted in **Figure 8-8**, there are three inflection points and intersection points in the first 20 seconds. Initially, the specimen with the highest dry density exhibits the fastest slaking behavior. After the first inflection point, the slaking behavior slows down, which is similar to the behavior observed in **Figure 8-6**. However, the two specimens with lower dry density did not exhibit rapid slaking behavior in the initial few seconds of the test. Instead, there are two inflection points where the slaking behavior accelerates until slaking behavior is complete. The specimen with the lowest dry density exhibits the earliest inflection point, and the slaking rate after the inflection point exceeds that of the specimen with medium dry density. This can be explained by comparing the pore characteristics of the three samples.

The actual pore shape can be simplified to cylindrical pore as shown in **Figure 8-9**.  $P_1$  is atmospheric pressure, and  $P_2$  is pore pressure after capillarity. The pressure difference can be calculated as Liu *et al.*, 2020:

$$\Delta P = P_2 - P_1 = \frac{2\gamma \cos\alpha}{r} \quad (8-2)$$

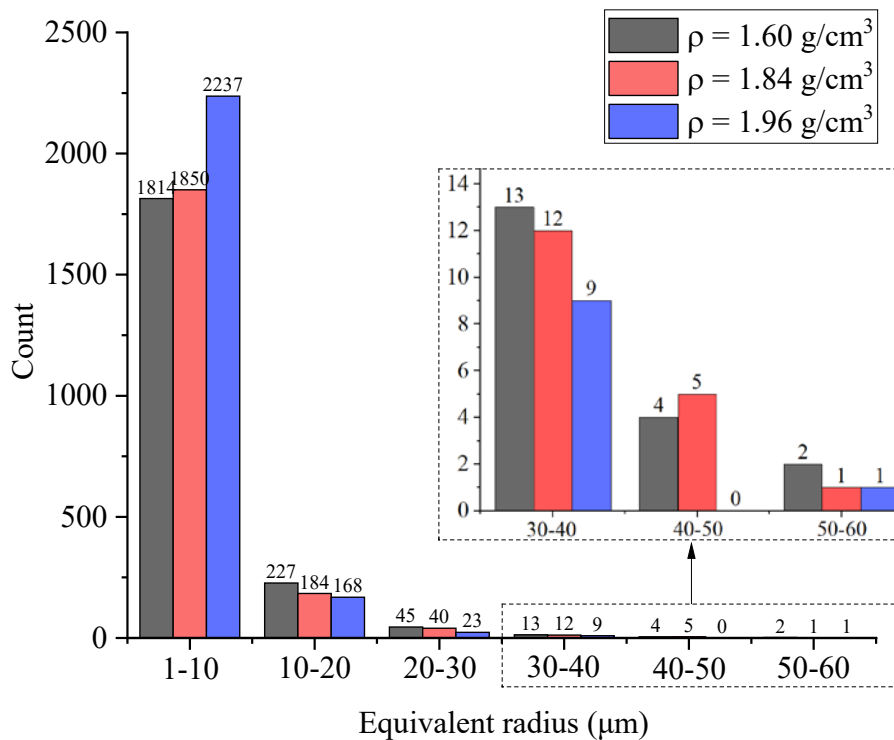
Where  $\gamma$  is the liquid surface tension coefficient;  $\alpha$  is the contact angle of water;  $r$  is the radius of a capillary tube.



**Figure 8-9 Compression of entrapped air**

As can be seen from the formula, smaller  $r$  values correspond to larger  $\Delta P$ . **Figure 8-10** illustrates the characteristics of pore size distribution. It should be noted that the pore radius in **Figure 8-10** is calculated after the pores are assumed to be circular. With an increase in dry density, the radius of pores above 10  $\mu\text{m}$  exhibits a decreasing trend. For the radius between 1 and 10  $\mu\text{m}$ , the number of pores in the specimens with a dry density of 1.60  $\text{g}/\text{cm}^3$  is similar to that of the specimen with medium dry density ( $\rho=1.84 \text{ g}/\text{cm}^3$ ). However, when the dry density reaches 1.96  $\text{g}/\text{cm}^3$ , the number of pores within the radius of 1-10  $\mu\text{m}$  significantly increases, and the increase is much larger than the decrease of the larger pores (10-60  $\mu\text{m}$ ) in the specimen. Combined with Formula (8-

2), it can be seen that smaller pores can generate greater pressure, thus reinforcing the air-breakage phenomenon. At the same time, more large pores result in more air escaping from the specimen at the beginning of the tests. These two factors explain why the specimen with the highest dry density in **Figure 8-6** slakes fastest at the beginning of the test. There is little difference in the number of small pores (1-10  $\mu\text{m}$ ) between the samples with dry densities of 1.66  $\text{g}/\text{cm}^3$  and 1.81  $\text{g}/\text{cm}^3$ . Therefore, the effect of the air-breakage phenomenon is similar in these two specimens. However, since there are more pores in the sample with a dry density of 2.00  $\text{g}/\text{cm}^3$ , the experimental results are smaller due to air escape, which ultimately leads to the slowest slaking behavior observed at the beginning of the test. As the specimen with the lowest dry density has more macropores, the air-breakage phenomenon, with air escaping, lasts for the shor



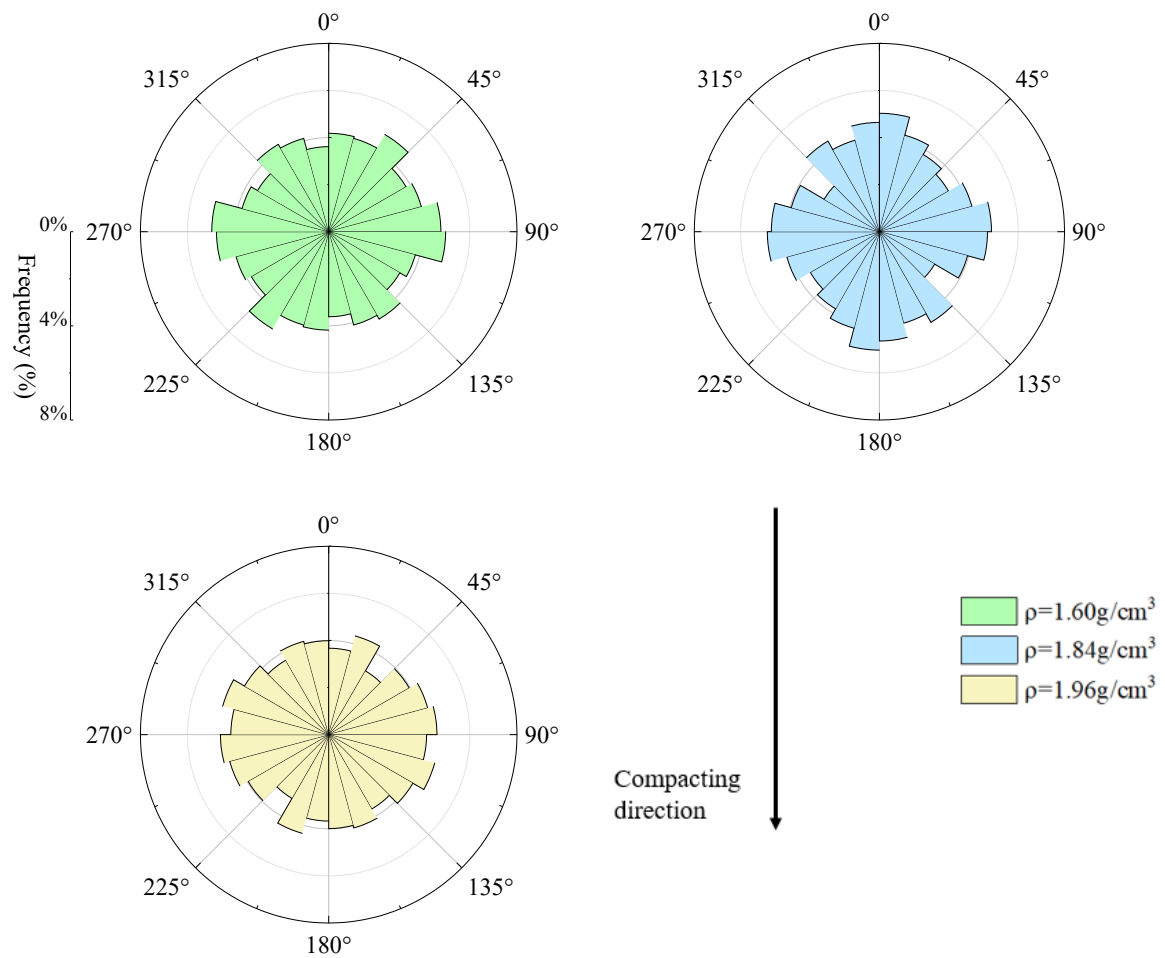
**Figure 8-10 Pore size distribution characteristic**

test period and results in reaching the turning point faster than other specimens.

#### 8.2.4 Pores and particles orientation distribution

Pore orientation determined by skeleton orientation was introduced in section 8.1. Skeletons with different lengths should represent different specific gravity in statistics. Therefore, the ratio of the sum of the skeleton length in each orientation interval to the total skeleton length is taken as the frequency of different directions (see **Figure 8-11**). The statistical orientation with the range of  $180^\circ$  are transformed into distribution results within the orientation range of  $360^\circ$  after common data processing (Hattab, Hammad and Fleureau, 2015; Tang *et al.*, 2020).

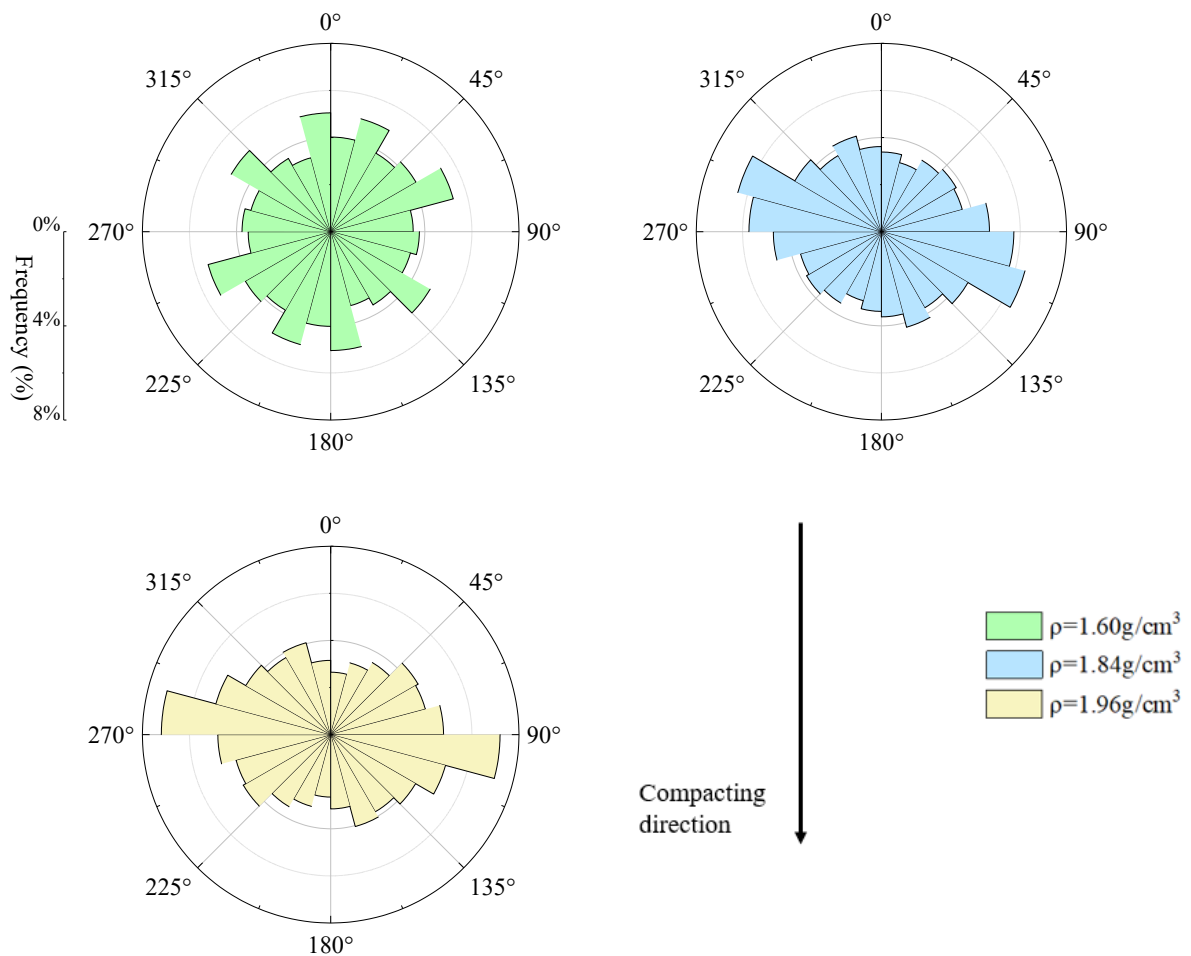
The orientation distribution of three specimens with different dry densities were shown in **Figure 8-11**. For the specimen with lowest dry density ( $\rho=1.60 \text{ g/cm}^3$ ), the main orientation of the pores is not clearly visible. The frequency is distributed between 4.97% and 3.49% for different pore orientations. When the dry density of the sample reaches  $1.84 \text{ g/cm}^3$ , the anisotropy of pore orientation distribution can be clearly observed. The orientations of pores are concentrated at  $0^\circ$ ,  $90^\circ$ ,  $180^\circ$  and  $270^\circ$ , reaching around 5% of frequency. Whereas the orientations of  $0^\circ$ ,  $90^\circ$ ,  $180^\circ$  and  $270^\circ$  have the smallest frequency, about 3%. The pore orientation distribution of specimen with dry density of  $1.96 \text{ g/cm}^3$  is also anisotropic, but not as obvious as that in specimen with medium dry density. This may be due to that in the specimen with the highest dry density, the pores are extruded into smaller pores that are beyond the observation range of SEM.



**Figure 8-11. Rosette Histogram of pore orientation distribution.**

Comparing the compacting direction ( $180^\circ$ ), the pore orientation gradually concentrates on two orientations during the increase of dry density: perpendicular to and parallel to compacting direction. While the pore proportion in other directions decreases. This can be interpreted as that the width of the bracket pores parallel to the compaction direction will be reduced after extrusion, thus forming directional pores. While the vertical pores are formed due to the change in the arrangement of particles, which will be explained later.





**Figure 8-12. Rosette Histogram of particle orientation distribution.**

In this study, the orientation of the moment of inertia is used to represent the orientation of the particle. The data is processed in the same way as the pore orientations, and results are distributed in the range of 360°. As can be seen in **Figure 8-12**, the particles orientation distribution of the specimen with lowest dry density ( $\rho=1.60 \text{ g/cm}^3$ ) is relatively uniform in the range of 360° and it's harder to observe the main orientation. For the specimen with  $1.84 \text{ g/cm}^3$  of dry density, the main orientation is close to the 90° and 270° direction, whose frequency reach 6.43%. While the lowest frequency is 3.04% in the range of 15° to 30°. The anisotropic orientation distribution of particles can be clearly seen in the specimen with the highest dry density. The orientation is

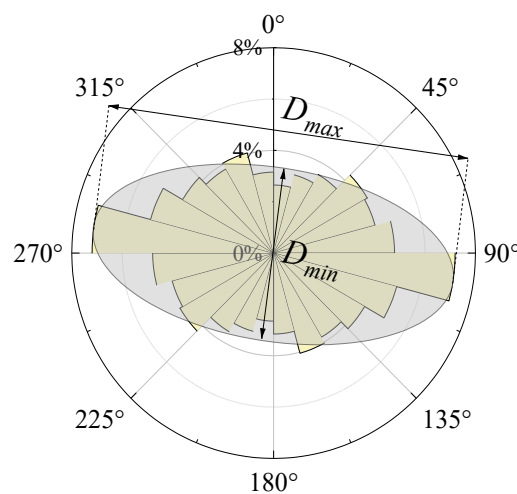
concentrated in 90° and 270°, and the frequency increase from 2.65% at the orientation of 0° and 180° to 7.20% at the orientation of 90° and 270°.

Comparing the compacting direction (180°), the particle orientation gradually concentrates on the orientation which is perpendicular to compacting direction during the increase of dry density. This indicates that the particles gradually become anisotropic as the compaction process. In the case of directional arrangement of particles, the orientation of the bracket pores between particles gradually changes, and eventually they are perpendicular to and parallel to the direction of compaction.

Anisotropy index ( $I_a$ ) has been widely used in many studies to reflect the degree of anisotropy of soil (Baojun, Bin and Inyang, 2008; Li *et al.*, 2020). In this study, the anisotropy index is calculated by a standard deviation ellipse as shown in **Figure 8-13** and the value can be calculated by the following formula:

$$I_a = \frac{D_{max} - D_{min}}{D_{max}} \times 100\% \quad (8-3)$$

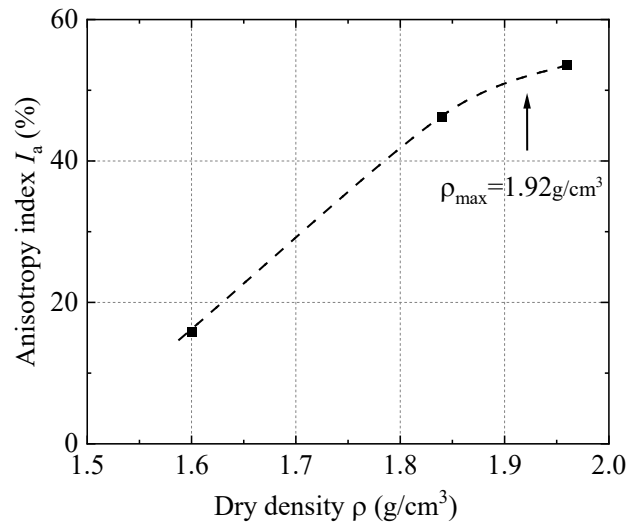
where  $D_{max}$  and  $D_{min}$  are the lengths of major and minor axes of the ellipse standard deviation ellipse shown in **Figure 8-13**.



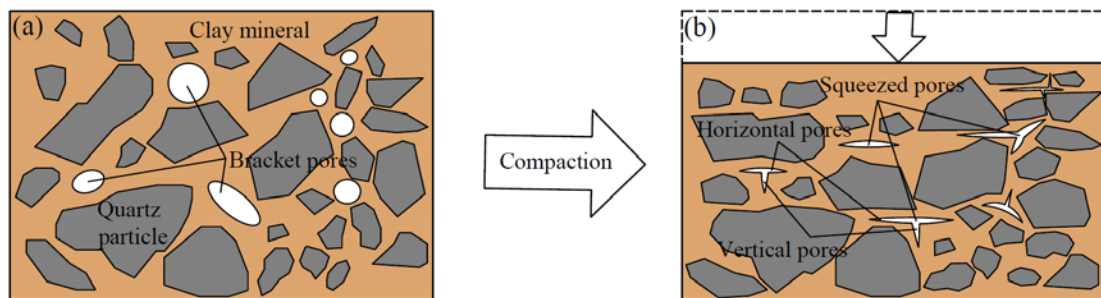
**Figure 8-13. Schematic diagram of determining the general direction and**

### anisotropy parameters.

After obtaining of anisotropy index, the relationship between anisotropy index and dry density is shown in **Figure 8-14**. As you can see, the anisotropic index increased from 15.79% to 46.21% as the dry density increased. After reaching the maximum dry density ( $\rho=1.92 \text{ g/cm}^3$ ), the growth rate of anisotropic index slowed, and the maximum anisotropic index value is 53.63% at the dry density of  $1.96 \text{ g/cm}^3$ .



**Figure 8-14. The relationship between anisotropy index and dry density.**



**Figure 8-15 Evolution of pore orientation during compaction**

As can be seen in **Figure 8-15**, the pore orientation gradually concentrates on two orientations during the increase of dry density: perpendicular to and parallel to compacting direction. While the pore proportion in other directions decreases. In the process of compaction, particles were oriented and perpendicular to the compaction direction (Shi, Murakami and Wu, 1998). Due to the rearrangement of particles and squeeze during compaction, the width of the bracket pores parallel to the compaction direction was reduced, thus forming pores perpendicular to the compaction direction (see **Figure 8-15b**: Horizontal pores). Whereas, the pores parallel to the compaction direction are formed due to pores between oriented particles (see **Figure 8-15b**: Vertical pores). The conclusion can be used in the study of anisotropic mechanical behavior as mentioned in the introduction.

## Conclusions

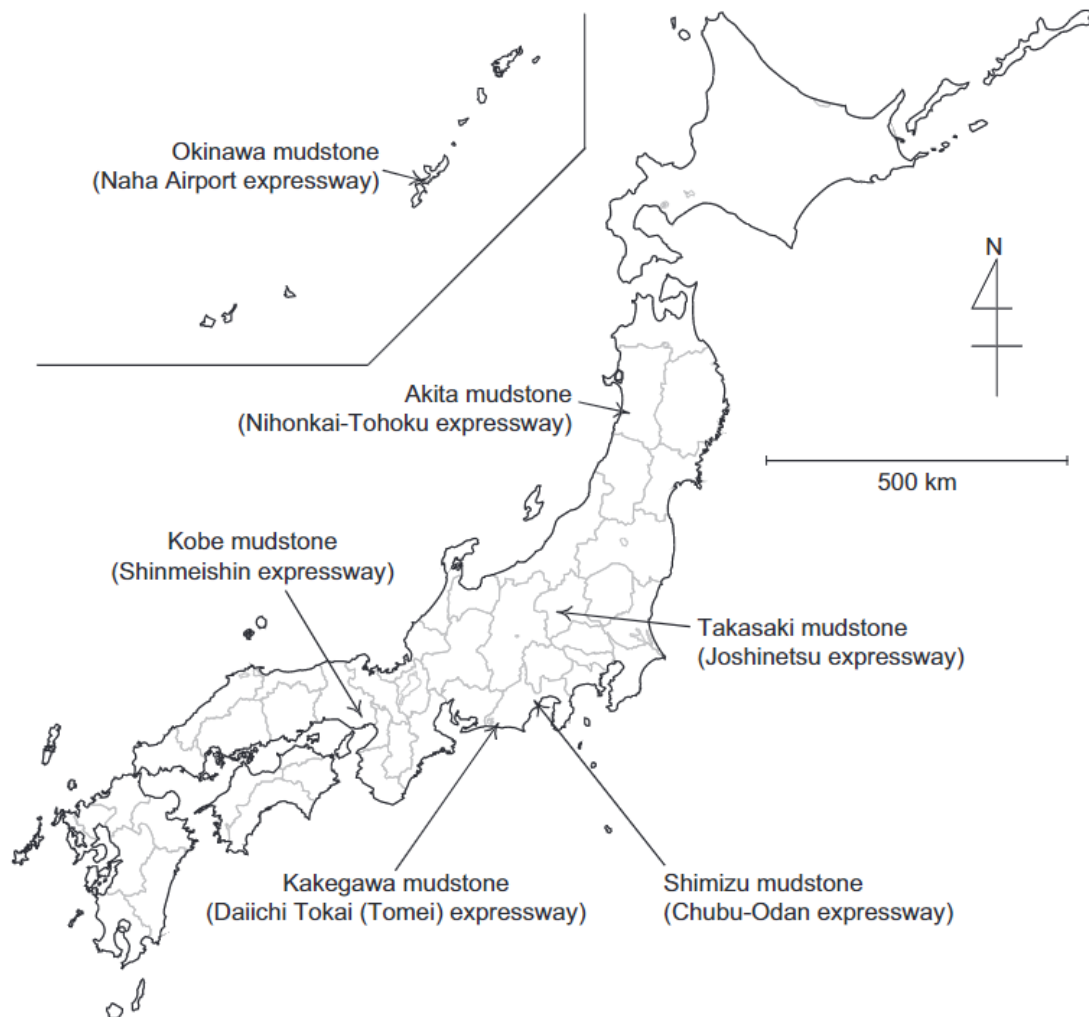
Through a series of tests, including expansion characteristics test, Slaking test and SEM test, the following conclusions were drawn in this study:

- (1) The structure of both natural and remodeled black mudstone is composed of quartz particles wrapped by clay minerals, and the large pores are between quartz particles.
- (2) Compared with natural mudstone, dried mudstone has stronger slaking performance. Under the condition of natural water content, Terashima mudstone does not slake. This is caused by pore water that is already present in the specimen.
- (3) Air-breakage phenomenon and air escaping result in the turning points in the slaking curves. Air-breakage phenomenon increases the slaking behavior while the air escape results in the low measured result. The different strength of the two causes result in different turning points

(4) SEM images of compacted crushed mudstone with different dry densities were studied. The results show that with the increase of dry density, the particle orientation distribution concentrates in the direction perpendicular to the compacting direction. While the pore orientation distribution gradually concentrates on the direction which is perpendicular to and parallel to compacting direction. On this basis, the relationship between anisotropy index and dry density were revealed: Anisotropy index ( $I_a$ ) increase with the increase of dry density and the growth slows down when the dry density reached the maximum dry density ( $\rho_{\max}$ ) obtained from the compaction curve.

**Chapter 9. APPLICATION IN PRACTICAL  
FIELD**

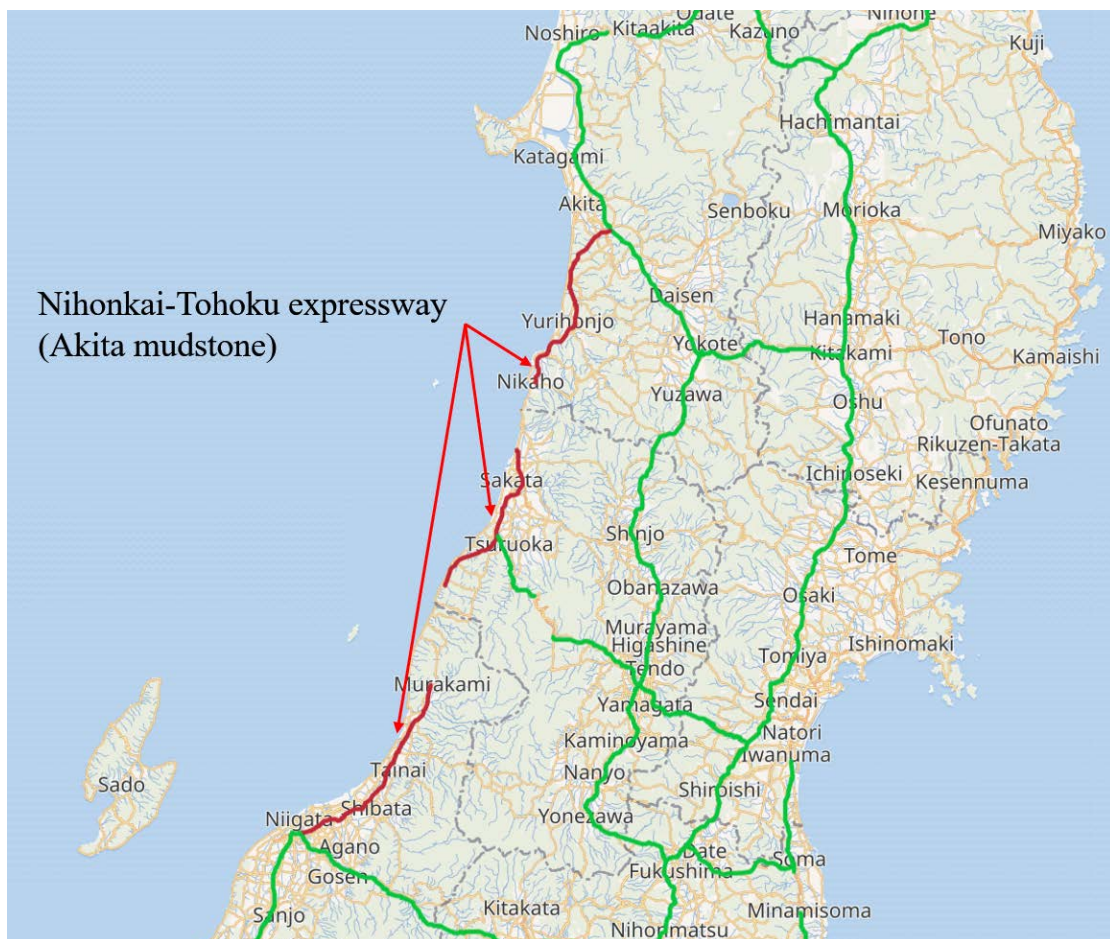
## 9.1 Overview



**Figure 9-1 Location of embankments in Japan from which mudstone specimens were sourced (Kikumoto, Putra and Fukuda, 2016)**

The construction of embankments or cut slopes through mudstone or shale formations has been plagued with numerous problems (Shamburger, Patrick and Lutton, 1975; Hopkins and Beckham, 1998). Crushed mudstone is commonly used in the construction of embankments in Japan, and the failure of one such embankment during the 2009 earthquake in the Makinohara district of the Tomei expressway was attributed to slaking of the mudstone, which has been investigated and analyzed in the field (Yasuda *et al.*,

2012). Landslides on tertiary sedimentary rocks are also of great interest in areas where such deposits are widely exposed, as the bedrock or mudstone in such cases is typically weathered and gradually weakened into landslide clay. Slaking of granular fills derived from mudstones and shales occurs when they are subjected to repeated wetting and drying cycles, leading to a finer grain size, reduced stiffness and strength, and structural instability. Thus, comprehending the weathering mechanism and the alterations in the physical and mechanical properties of geomaterials derived from feeble rocks like mudstones is imperative in examining the sustained stability of slopes (Bhattarai *et al.*, 2006).



**Figure 9-2 Nihonkai-Tōhoku Expressway (modified from [https://en.wikipedia.org/wiki/Nihonkai-T%<sup>C5</sup>%8Dhoku\\_Expressway#/map/0](https://en.wikipedia.org/wiki/Nihonkai-T%C5%8Dhoku_Expressway#/map/0))**

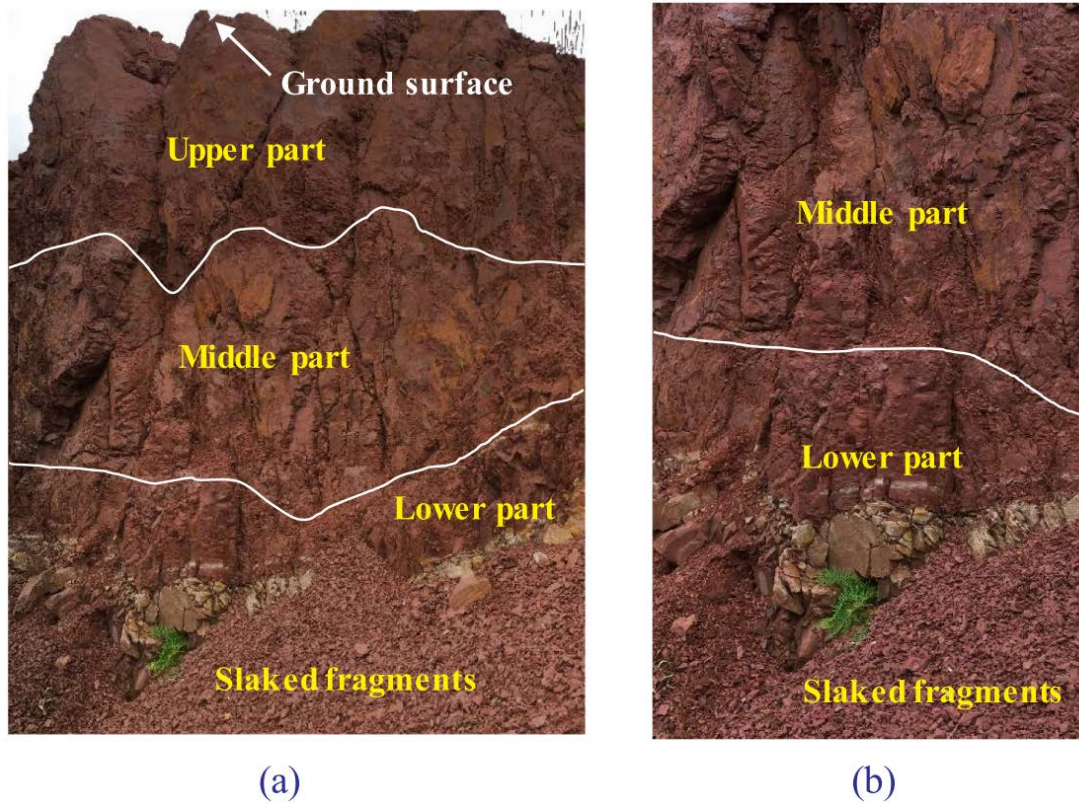


The course of the expressway takes it alongside the coastline of the Sea of Japan (Nihonkai) in the Tōhoku region of Japan (see **Figure 9-2**). The Nihonkai-Tōhoku Expressway is the operating name for the sections of the Nihonkai Engan Tōhoku Expressway that are operated by East Nippon Expressway Company. The Nihonkai Engan Tōhoku Expressway is an official designation consisting of several routes that link Niigata with Aomori via Yamagata and Akita (MLIT, 2011), reaching a total of approximately 322 km (MLIT, 2009). Akita mudstone is used in this expressway. And the seawater influence on this kind of material is necessary.



**Figure 9-3 Slaking problem of mudstone in embankment and tunnel**

**Figure 9-3** shows that a failure of highway embankment of Tomei expressway caused by slaking of mudstone. And the slaking of mudstone in tunnels results in layer-by-layer stone peeling, significantly affecting the project's safety. In addition, the fact that stress can promote slaking behavior has already been observed in some studies (Z. Zhang *et al.*, 2020). As shown in **Figure 9-4**, the lower part of the slope exhibits much more severe fragmentation than the upper part. In this chapter, the application of study about mudstone will be introduced.



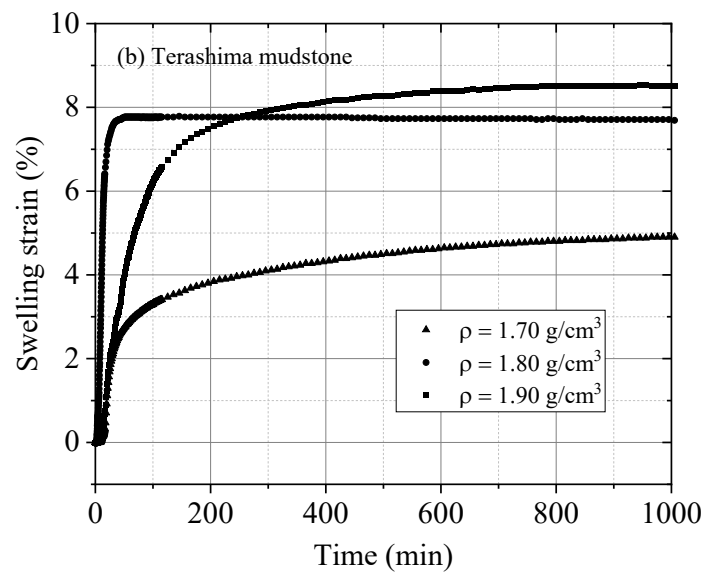
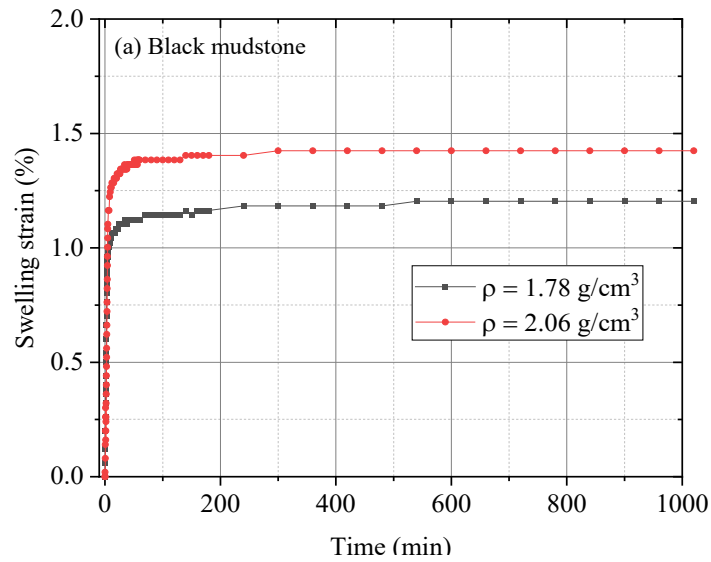
**Figure 9-4 Surfacial slaking phenomenon of Wulidui slope: (a) surficial slaking zonation of the slope and (b) surficial slaking in lower and middle parts of the slope (Z. Zhang *et al.*, 2020)**

## 9.2 Application of mudstone in embankment

The use of mudstones in road construction may cause the roadbed to lift or settle due to volume changes. This can pose a safety hazard to expressways. In addition, soil shrinkage can also lead to the formation of cracks, which promote the movement of water in the soil. The presence of cracks can also affect the strength of the soil.

The swelling strains of three kinds of mudstone are shown in **Figure 9-5**. The swelling strains of black mudstone are lowest in these three kinds of mudstone, which are between 1.0% and 1.5% under the stress of 7.95kpa. When this material is used in the embankment, it hardly causes any uplift of the roadbed. Therefore, in this respect, black mudstone is a material with excellent properties for embankment. However, the

swelling strains of Terashima and Akita mudstone is larger than black mudstone, which means that as embankment materials, these two materials need to consider their swelling property and the effect on the uplift of the embankment.



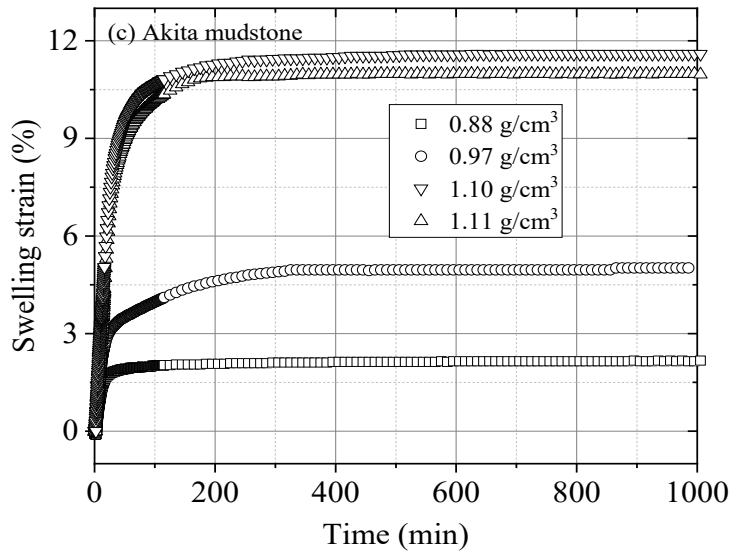


Figure 9-5 Swelling strain of three kinds of mudstone (stress: 7.95kPa)

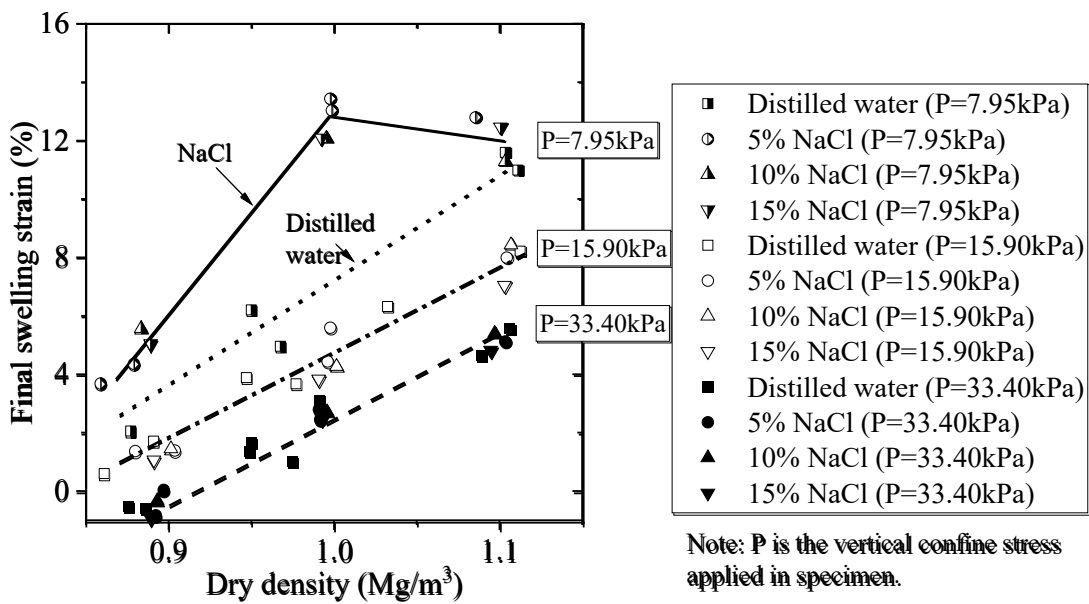
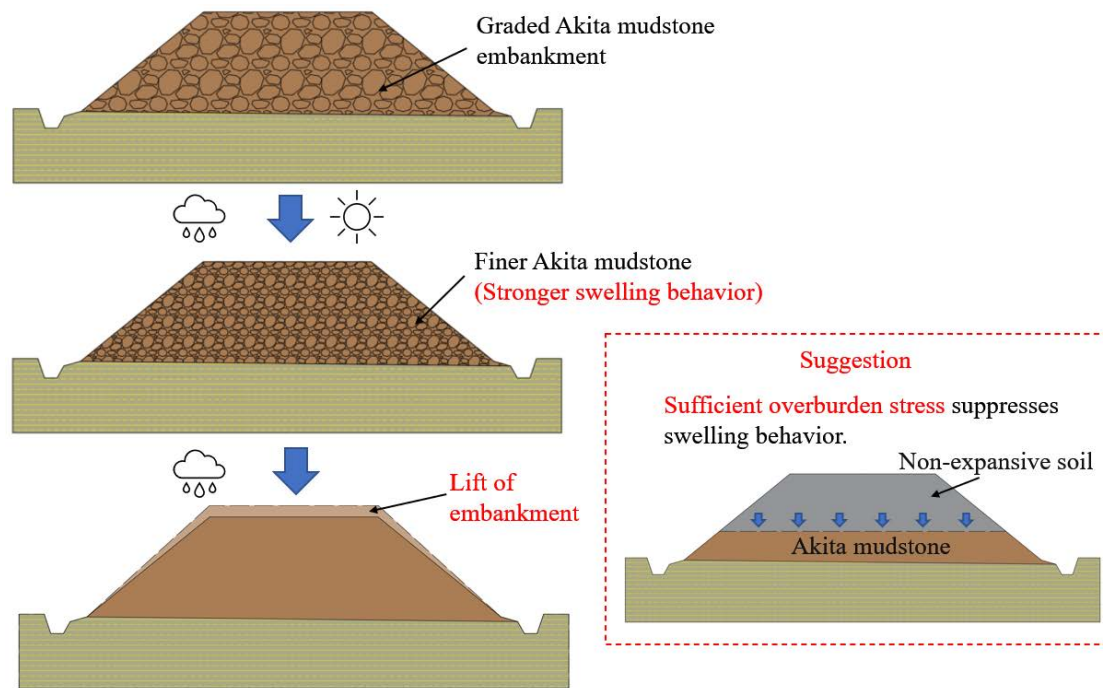


Figure 9-6 Swelling strain of Akita mudstone with different concentration of NaCl solution and different vertical confine stress



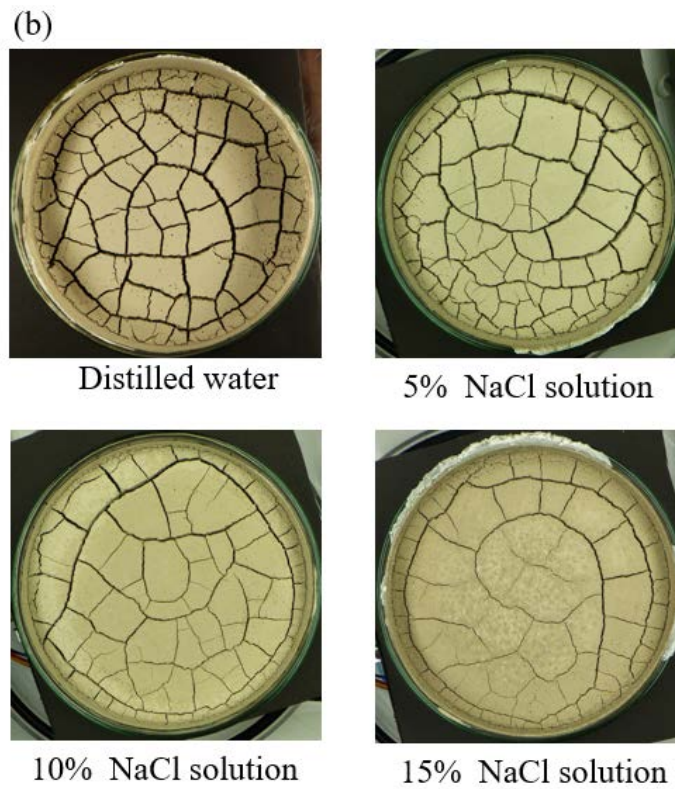
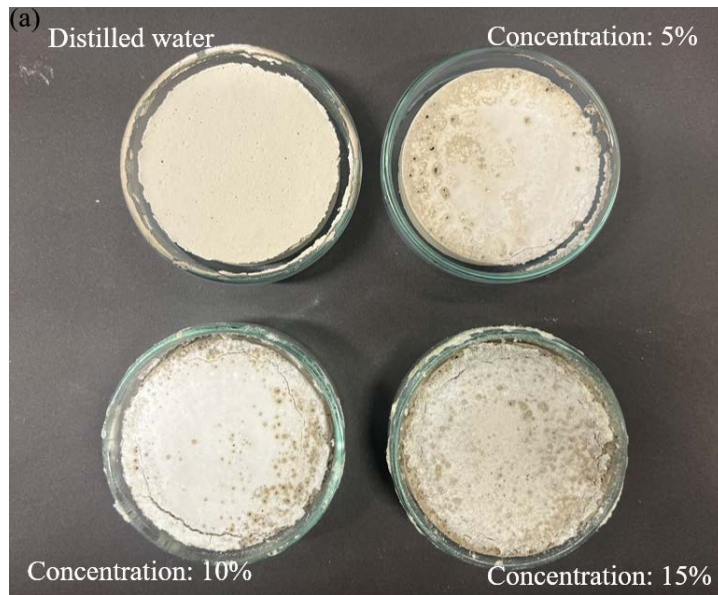
**Figure 9-7 Suggestion for avoiding lift of embankment**

As Akita mudstone is applied in coastal expressway-Nihonkai-Tōhoku Expressway, the impact of seawater on the swelling characteristics of Akita mudstone cannot be ignored. From the **Figure 9-6**, it can be observed that at low stress stages (7.95kPa), the sodium chloride solution significantly increases the swelling strain of Akita claystone, especially at medium dry densities (1.0g/cm<sup>3</sup>). Therefore, the following suggestions are proposed for practical engineering:

- 1) Akita mudstone should not be used as fill material for coastal highway embankments.
- 2) If Akita mudstone is used as fill material for coastal highway embankments, low dry density (0.9g/cm<sup>3</sup>) will result in significant settlement, and Akita mudstone with medium dry density (1.0g/cm<sup>3</sup>) will have significant swelling due to the influence of seawater. Therefore, it is recommended to use Akita claystone with higher dry density (1.1g/cm<sup>3</sup>) for embankment construction.
- 3) When the overburden stress is low, sodium chloride solution can greatly enhance the swelling behavior of Akita mudstone. Therefore, it is recommended to use Akita

claystone as fill material for lower layer embankments to ensure that the larger overburden stress suppresses its swelling behavior as shown in **Figure 9-7**.

Shrinkage and cracking evolution of Akita mudstone mixed with NaCl solution are shown in **Figure 9-8**. Akita mudstone has strong shrinkage characteristics, which can lead to cracking during the drying process, posing a threat to engineering. However, sodium chloride can reduce the shrinkage characteristics of mudstone (see **Figure 9-8a**) and suppress the development of cracks (see **Figure 9-8b**). Therefore, if Akita mudstone is used to fill the embankment in the construction of a coastal expressway, the sodium chloride in seawater will reduce the shrinkage of Akita mudstone and reduce the development of cracks. However, it should be noted that although the sodium chloride solution reduces the shrinkage characteristics of Akita mudstone, the dry density after drying is also greatly reduced (see **Figure 7-17**), which may become a new safety hazard. Therefore, it is recommended to refer to the research results of this paper and combine them with actual engineering to choose a more optimal solution.

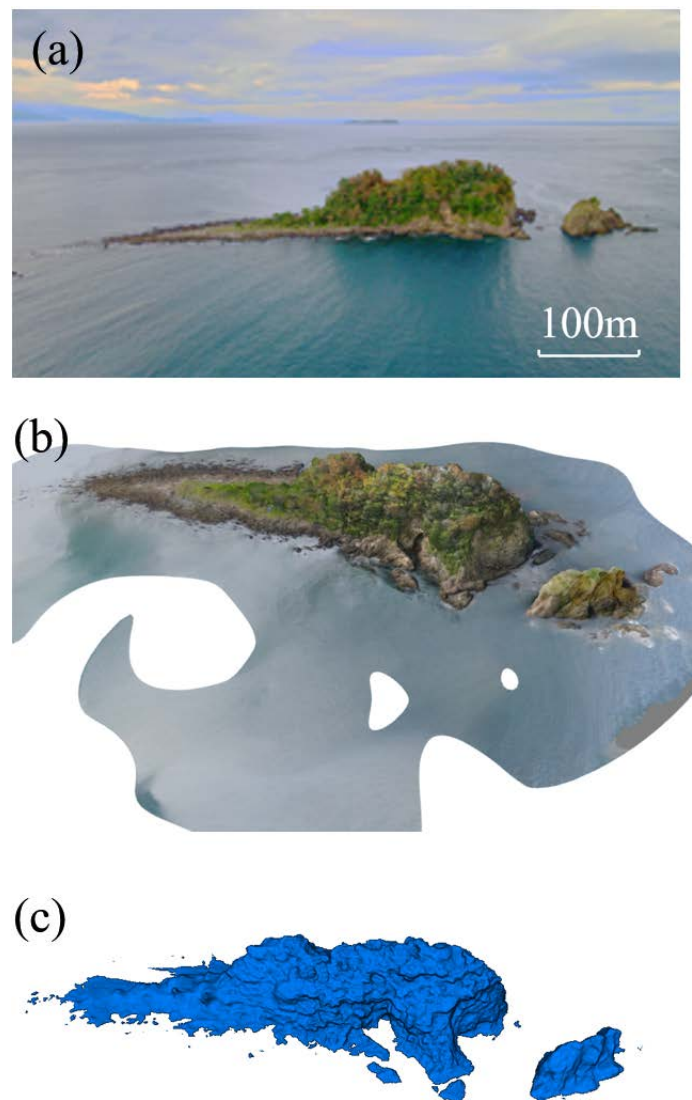


**Figure 9-8 (a)Shrinkage and (b)cracking evolution of Akita mudstone**

### **9.3 Application of multi-view approach**

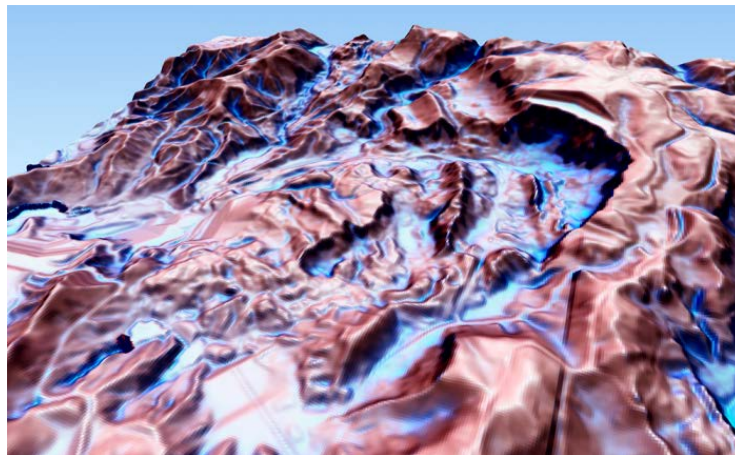
The application of the multi-view approach has been validated, especially in the case of large-scale models, as it offers strong convenience (see **Figure 9-9** and **Figure 9-10**).

The multi-view approach has been validated for monitoring large-scale landforms and can provide detailed information for design. It can also be applied to the study of surface roughness and rockfall. However, this study introduced this method to laboratory experiments. Not only could data such as sample volume and surface area be extracted, but the scope could also be extended to small scales, such as microscopes and SEM (see **Table 4-4**). In addition, using the improved experimental method in this study can obtain a more precise 3D model of the sample (see **Figure 4-4**). This makes it possible to use this method for the study of three-dimensional parameters of microscale particles, such as the study of particle breakage.

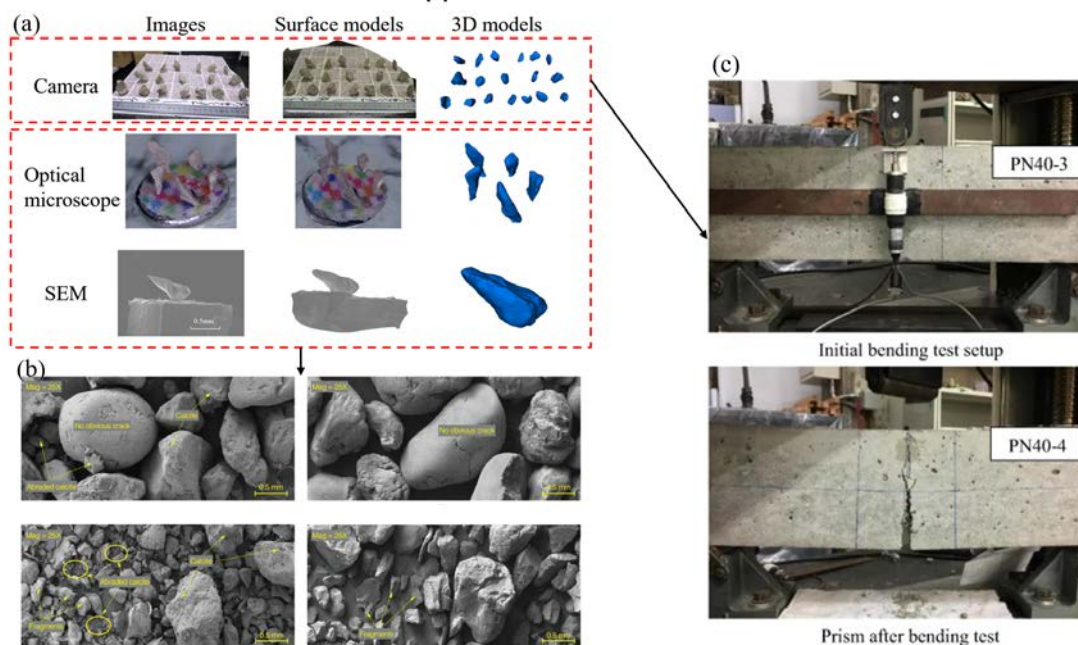


**Figure 9-9 Application of multi-view approach on large scale**





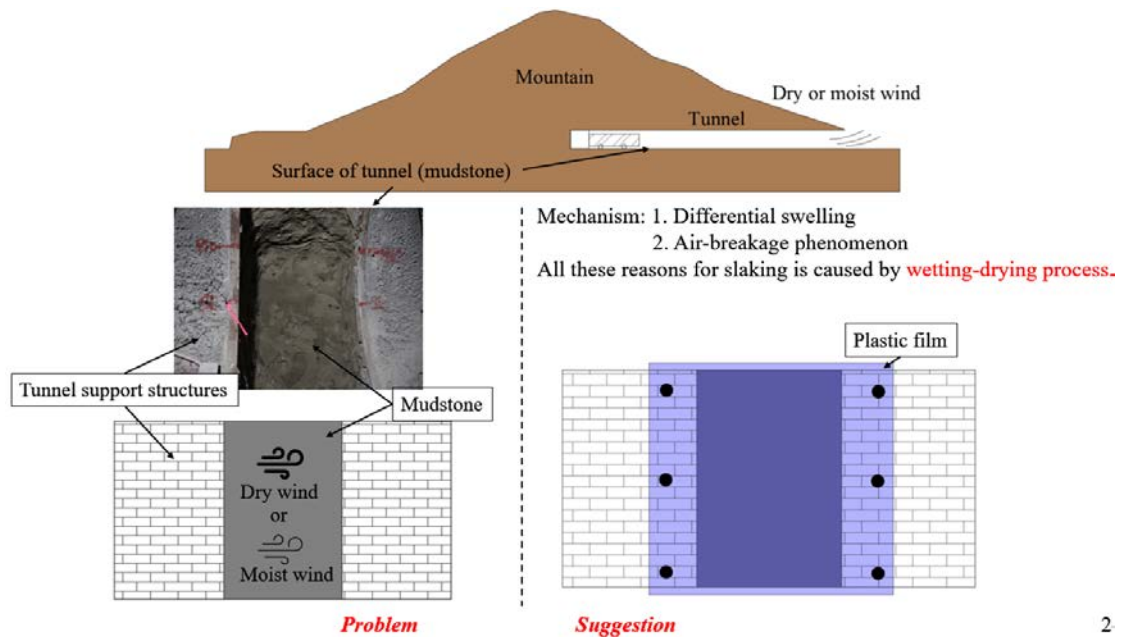
**Figure 9-10 Slope failure SV map of Aratozawa - aerial view from Chuo Kaihatsu Corporation (<https://www.ckcnet.co.jp/technology/survey/geodx/>)**



**Figure 9-11 Application of SfM-MVS approach on research such as (a) Bending tests of concrete (Raju R A, Lim S, Akiyama M, et al. ) and (b) Different shapes of sands after breakage (Xiao Y, Chen H, Stuedlein A W, et al.)**

The SfM-MVS method can also be applied in research. For instance, as shown in **Figure 9-11a**, photographs of specimens can be taken during deformation experiments for deformation analysis. Additionally, this technique can be utilized for studying shape of particle after breakage due to various reasons, as depicted in **Figure 9-11b**.

## 9.4 Slaking problem and low strength of mudstone in tunnel and embankment

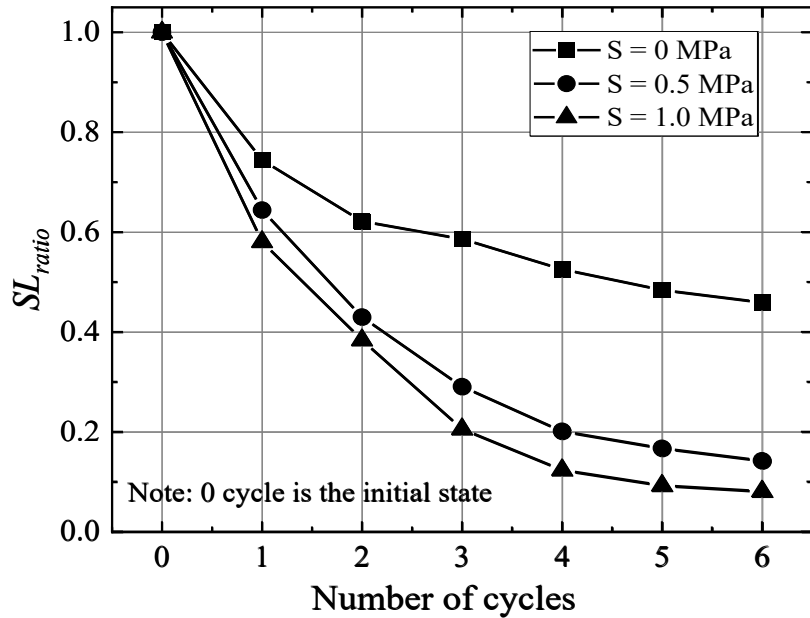


2

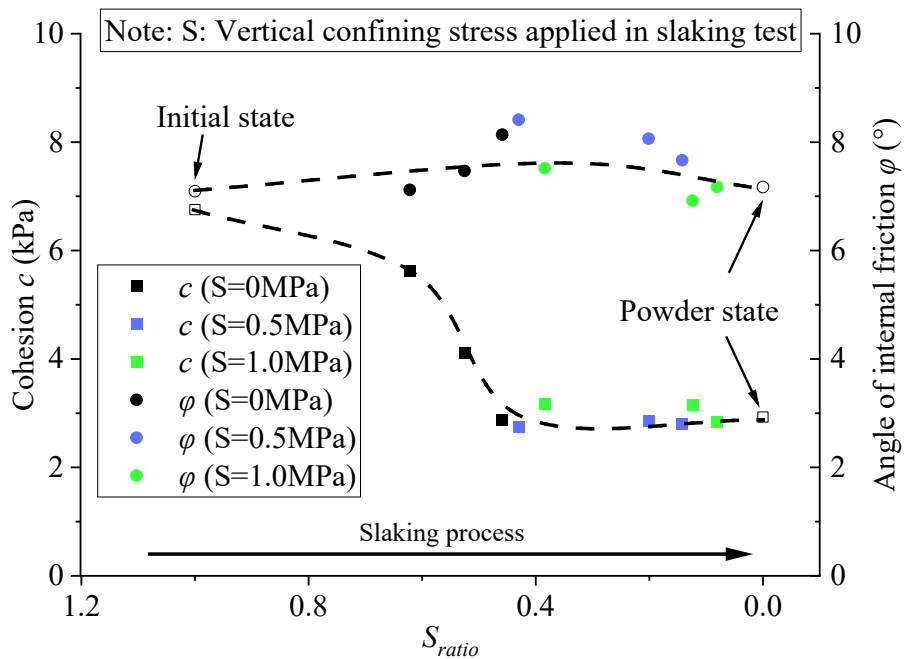
**Figure 9-12 Suggestion for slaking problem in tunnel**

During tunnel excavation, the slaking phenomenon of mudstone will result in a decrease in its strength, which poses a threat to the engineering project. The mechanisms of the slaking have been discussed in Chapter 5, with three mechanisms identified: (1) the air-breakage phenomenon, (2) differential swelling and (3) the dissolution of cement agents. All three mechanisms are related to water infiltration, therefore slaking of the mudstone will not happen if it is maintained at a constant water content, as demonstrated in Chapter 8. As shown in **Figure 9-12**, during the tunnel excavation process, the surface layer of the mudstone in the tunnel is exposed to the air and dried or wetted by dry or moist wind. This ultimately leads to air-breakage phenomenon, differential swelling

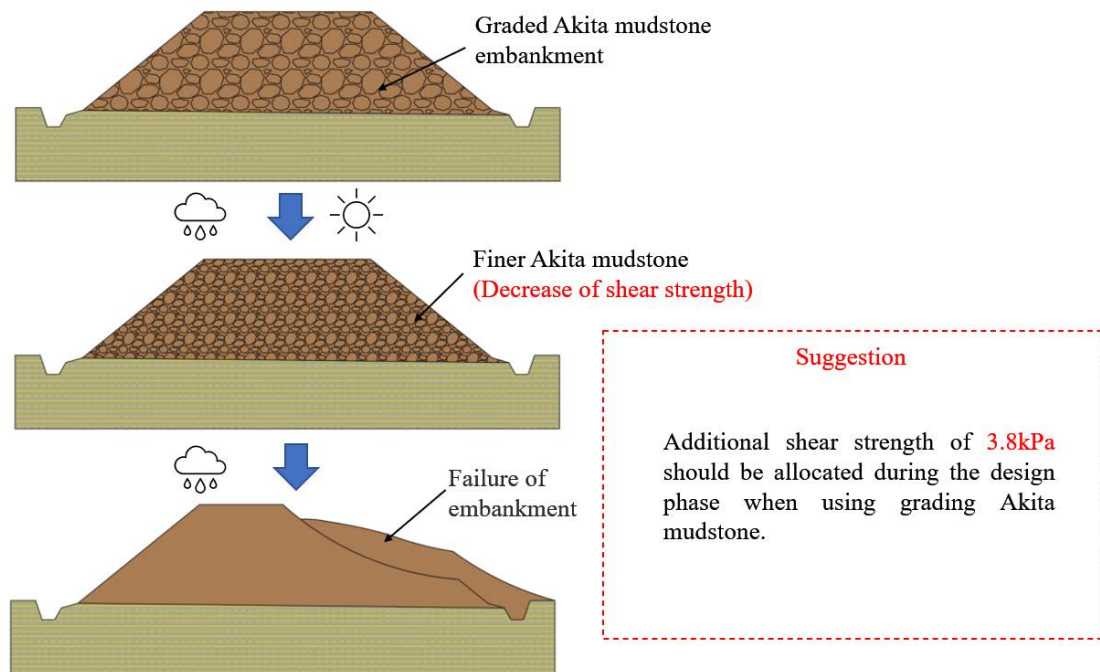
and the dissolution of cement agents of the surface mudstone in the tunnel, and results in the peeling and collapse of the unsupported portion in **Figure 9-12**.



**Figure 9-13 Evolution of  $SL_{ratio}$  with slaking process under different vertical stress**



**Figure 9-14 Summarize of  $c$  and  $\phi$  during slaking process**



**Figure 9-15 Suggestion for avoiding failure of embankment**

The presence of stress will accelerate the rate of mudstone slaking, as shown in **Figure 9-13**. With increasing stress, the degree of slaking is strengthened, resulting in a reduction in particle size and ultimately a decrease in cohesion ( $c$ ), which can be observed in **Figure 9-14**. In engineering program, it is important to consider the slaking of mudstone in high-pressure areas. Meanwhile, as shown in **Figure 9-15**, additional shear strength of 3.8kPa should be allocated during the design phase when using grading Akita mudstone as the embankment filling material. However, as shown in **Figure 9-12**, the premise for slaking is to experience cycles of wetting and drying. Therefore, even if the mudstone is subjected to high stress, slaking behavior will not occur if it is not exposed to air, such as the area protected by the tunnel support structure in **Figure 9-12**. Therefore, during tunnel excavation, it is advisable to use plastic film to cover the exposed mudstone to prevent the mudstone from experiencing the process of dry-wet cycles and avoid the occurrence of slaking behavior.

## 9.5 Future plan

This paper's research is mainly divided into three parts:

1. The mechanism of mudstone slaking and the influence of stress on slaking behavior, as well as the changes in direct shear strength of mudstone after slaking were studied.
2. The swelling-shrinkage characteristics of mudstone and its cracking evolution under the influence of sodium chloride solution were studied.
3. The orientation distribution of pores and particles during compaction were studied.

The future plans consist of the following points:

1. With mudstone slaking process, the cracking evolution will change with the variation of particle size distribution of mudstone, which has not been studied yet. Therefore, the plan is to conduct cracking tests on mudstones with different PSDs.
2. In the future, the cracking characteristics of other mudstones besides Akita mudstone should also be studied.
3. Although the pores and particles orientation of compacted specimens were studied in Chapter 8, the influence of soil anisotropy on soil strength has not been investigated. Therefore, in order to apply the study of soil anisotropy to practical engineering, the influence of soil anisotropy on soil strength should be investigated in the future.

Overall, future research will be done based on existing studies and focus on investigating the characteristics of mudstone.

Conclusions

From the perspective of swelling characteristics, black mudstone is a suitable expressway embankment filling material due to its lower swelling property. However, the swelling strains of Terashima and Akita mudstone is larger than black mudstone, which means that as embankment materials, these two materials need to consider their swelling property and the effect on the uplift of the embankment. As coastal highway embankments material, larger dry density of Akita mudstone should be used considering seawater influence. On the other hand, although the sodium chloride solution reduces the shrinkage characteristics of Akita mudstone, the dry density after drying is also greatly reduced, which may become a new safety hazard. Finally, in order to avoid slaking behavior during tunnel excavation, the surface of mudstone exposed to air should avoid wet-dry cycles.

## **Chapter 10. CONCLUSIONS**

As a widely distributed soft rock, mudstone has been used as a material for embankment. In this thesis, swelling properties of three kinds of mudstone were studied. Based on the swelling strain tests, improved multi-view approach was introduced for studying the mechanism of mudstone slaking behavior. Besides, considering different vertical confining stresses, the particle size distributions (PSD) of mudstone during slaking were studied and the shear strength evolution along with the changes of PSD were studied. The cracking evolution of mudstone under different concentration of NaCl solution was also studied by the corresponding shrinkage behavior. Finally, the orientation of pores and particles of compacted mudstone were also studied by scanning electron microscope (SEM) tests.

In Chapter 1, the damage caused by mudstone in engineering practice, such as slope failures on expressways and slaking behavior of mudstone in tunnels, is introduced. Based on these, the mechanisms of slaking, volume change and crack evolution of the soil are discussed in detail. Finally, the research framework and objectives of this study are presented.

In Chapter 2, the basic physical characteristics of three mudstone materials are introduced. In addition, scanning electron microscopy and X-ray diffraction experiments were also conducted. The results showed that Akita mudstone has a higher content of montmorillonite. In particular, accelerated slaking experiments were also carried out on these three mudstones and finally, they were classified accordingly.

In Chapter 3, the swelling strain tests were conducted and results imply that the swelling strain and pressure of black mudstone are both within a relatively low range, which may be attributed to its low content of montmorillonite. On the other hand, although Terashima mudstone also has low content of montmorillonite, its swelling strain is much greater than that of black mudstone. This suggests that there may be other



minerals in Terashima mudstone that contribute to its larger swelling strain. Swelling strains of Akita mudstone decrease with the increase of vertical stress and increase with the increase of dry density. With different concentration of sodium chloride solution, the swelling strains increase due to the conversion of some calcium-based montmorillonite into sodium-based montmorillonite under low stress and this increase can be compacted by applying stress. On the other hand, the  $\text{Ca}^+$  and  $\text{Mg}^+$  ions in Akita mudstone were leached out by  $\text{Na}^+$  ions in the solution, which support the conclusion. In Chapter 4, the improvement of multi-view approach was proposed. Compared to the CT method, multi-view approach cannot observe the internal structure of the specimen. However, this method can be applied to specimens of different scales, and the accuracy of the obtained model increases with higher resolution of images. Based on the mechanism of the multi-view approach, this chapter proposes an improved multi-view method that can optimize the accuracy of the model at the contact between the specimen and the specimen plate. The results of the measured parameters also confirm this. In addition, the multi-view approach can be applied using SEM images, but its accuracy needs to be further studied.

In Chapter 5, multi-view approach was used for measure the shape of mudstone during slaking process. During the tests, the shape of Akita mudstone during slaking was studied using the multi-view approach. The medium particles typically have a larger specific surface area than particles of other sizes, resulting in peaks in the  $S_{3d}$  curves. These peak values in the vacuum slaking tests are larger than in the atmospheric slaking tests, indicating that the differential swelling mechanism causes the shell-like medium specimens. Finally, two co-existing mechanisms for Akita mudstone slaking were explored and a new insight into the differential swelling mechanism due to the uneven

water distribution during slaking behavior was proposed. A typical layer-slaking phenomenon caused by this differential swelling mechanism was observed.

In Chapter 6, slaking tests under vertical confine stresses were conducted and the results imply that vertical stress accelerates the slaking process of Akita mudstone. With the increase of vertical stress, the phenomenon of slaking will also be further intensified, which results in lager change in PSD of grading Akita mudstone. And with the PSD change of specimens during slaking process, cohesion value decreases from 7 to 3kPa until the  $SL_{ratio}$  reaches 0.4 and then remain constant. Meanwhile, the change angle of internal friction is not visible during slaking process, fluctuating between 7 and 8°.

In Chapter 7, the shrinkage and cracking tests were conducted on Akita mudstone and the results imply that the sodium chloride solution weakened the development of cracks by suppressing the shrinkage of the specimen In Akita mudstone. The development of cracks has a strong correlation with the shrinkage characteristics of the soil, and as the shrinkage capacity of the soil decreases, the final crack rate also linearly decreases. In addition, the evolution of cracks can be divided into four stages, namely Stage I - No crack stage; Stage II - Primary crack stage; Stage III - Sub-crack stage; and Stage IV - Crack extension stage. Moreover, these stages have distinct characteristic boundary points. The saturation of specimens by sodium chloride solution significantly shortened Stages II and III, and prolonged Stage I.

In Chapter 8, the slaking tests were conducted and the pores and particles oritention distribution during compaction were studied by SEM tests. Compared with natural mudstone, dried mudstone has stronger slaking performance. Under the condition of natural water content, Terashima mudstone does not slake. This is caused by pore water that is already present in the specimen. Air-breakage phenomenon and air escaping result in the turnning points in the slaking curves. Air-breakage phenomenon increases

the slaking behavior while the air escape results in the low measured result. The different strength of the two causes result in different turning points. Moreover, SEM images of compacted crushed mudstone with different dry densities were studied. The results show that with the increase of dry density, the particle orientation distribution concentrates in the direction perpendicular to the compacting direction. While the pore orientation distribution gradually concentrates on the direction which is perpendicular to and parallel to compacting direction. On this basis, the relationship between anisotropy index and dry density were revealed: Anisotropy index ( $I_a$ ) increase with the increase of dry density and the growth slows down when the dry density reached the maximum dry density ( $\rho_{\max}$ ) obtained from the compaction curve.

In Chapter 9, the engineering application of this study was discussed. From the perspective of swelling characteristics, black mudstone is a suitable expressway embankment filling material due to its lower swelling property. However, the swelling strains of Terashima and Akita mudstone is larger than black mudstone, which means that as embankment materials, these two materials need to consider their swelling property and the effect on the uplift of the embankment. As coastal highway embankments material, larger dry density of Akita mudstone should be used considering seawater influence. On the other hand, although the sodium chloride solution reduces the shrinkage characteristics of Akita mudstone, the dry density after drying is also greatly reduced, which may become a new safety hazard. Finally, in order to avoid slaking behavior during tunnel excavation, the surface of mudstone exposed to air should avoid wetting-drying cycles.

Based on the above research results, the following conclusions can be drawn:

- (1) Of the three mudstone types, Akita mudstone and Terashima mudstone have relatively high rates of expansion. When used as roadbed fill material, designers

need to consider their swelling properties and their potential to uplift the expressways. Especially for Akita mudstone, under specific conditions, the sodium chloride solution will significantly increase its swelling strain.

- (2) A new insight into the differential swelling mechanism due to the uneven water distribution during slaking behavior was proposed in Akita mudstone. And this slaking mechanism will result in the broken particles presenting a larger specific surface area. Furthermore, the slaking process resulted in changes to the particle size distribution (PSD) of the mudstone, which subsequently reduced its shear strength. This could potentially lead to the occurrence of embankment landslides.
- (3) The sodium chloride solution inhibits the shrinkage of the soil and thus reduce the development of cracks. However, it should be noted that although cracks are reduced, the reduction in soil strength caused by the low dry density under NaCl solution exposure can become a new hazard.

In summary, this paper provides a detailed study of the slaking, swelling, shrinkage, and cracking characteristics of mudstones. The study has demonstrated that certain properties of mudstones can be the cause of disasters, and thus these issues should be taken into consideration during design and construction. The experimental results presented in this paper can serve as a reference for the design and construction of expressways and tunnels.

## Chapter 11. References

- Agarwal, S. *et al.* (2011) 'Building rome in a day', *Communications of the ACM*, 54(10), pp. 105–112.
- Amorim, C.L.G. *et al.* (2007) 'Effect of clay–water interactions on clay swelling by X-ray diffraction', *Nuclear Instruments and Methods in Physics Research Section A: Accelerators, Spectrometers, Detectors and Associated Equipment*, 580(1), pp. 768–770.
- Asner, G.P. (2000) 'Contributions of multi-view angle remote sensing to land-surface and biogeochemical research', *Remote Sensing Reviews*, 18(2–4), pp. 137–162.
- Baojun, W., Bin, S. and Inyang, H.I. (2008) 'GIS-based quantitative analysis of orientation anisotropy of contaminant barrier particles using standard deviational ellipse', *Soil and Sediment Contamination*, 17(4), pp. 437–447.  
doi:10.1080/15320380802146784.
- Bhattacharai, P. *et al.* (2006) 'Influence of weathering on physical and mechanical properties of mudstone', *Disaster mitigation of debris flows, slope failures and landslides*, 2, pp. 467–479.
- Boynton, S.S. and Daniel, D.E. (1985) 'Hydraulic conductivity tests on compacted clay', *Journal of Geotechnical Engineering*, 111(4), pp. 465–478.
- Chaduvula, U., Viswanadham, B.V.S. and Kodikara, J. (2017) 'A study on desiccation cracking behavior of polyester fiber-reinforced expansive clay', *Applied Clay Science*, 142, pp. 163–172.
- Colina, H. and Roux, S. (2000) 'Experimental model of cracking induced by drying shrinkage', *The European Physical Journal E*, 1, pp. 189–194.

- Cornelis, W.M. *et al.* (2006) 'Measuring and modelling the soil shrinkage characteristic curve', *Geoderma*, 137(1–2), pp. 179–191.
- Dai, Z. *et al.* (2021) 'Long-term uplift of high-speed railway subgrade caused by swelling effect of red-bed mudstone: case study in Southwest China', *Bulletin of Engineering Geology and the Environment*, 80, pp. 4855–4869.
- Danxi, S. *et al.* (2023) 'Three-dimensional characterization of cracks in undisturbed Mile expansive soil using X-ray computed tomography', *Soils and Foundations*, 63(3), p. 101282.
- Erguler, Z.A. and Shakoor, A. (2009) 'Relative contribution of various climatic processes in disintegration of clay-bearing rocks', *Engineering Geology*, 108(1–2), pp. 36–42. doi:10.1016/j.enggeo.2009.06.002.
- Fereidooni, D. and Ghobadi, M.H. (2015) 'Effect of mineralogy on durability and strength of hornfelsic rocks under acidic rainfall in urban areas', *Journal of Engineering Geology*, 9(2), pp. 2765–2788.
- Fernlund, J.M.R. (1998) 'The effect of particle form on sieve analysis: a test by image analysis', *Engineering Geology*, 50(1–2), pp. 111–124.
- Foster, W.R., Savins, J.G. and Waite, J.M. (1954) 'Lattice expansion and rheological behavior relationships in water-montmorillonite systems', *Clays and Clay Minerals*, 3, pp. 296–316.
- Franklin, J.A. and Chandra, R. (1972) 'The slake-durability test', in *International Journal of Rock Mechanics and Mining Sciences & Geomechanics Abstracts*. Elsevier, pp. 325–328.
- Fredlund, D.G. and Rahardjo, H. (1993) *Soil mechanics for unsaturated soils*. John Wiley & Sons.

- Gao, Y. and El-Zein, A. (2021) 'Observation of autogenous sealing of bentonite clay with X-ray computerized tomography', *Japanese Geotechnical Society Special Publication*, 9(2), pp. 14–19.
- Gautam, T.P. and Shakoor, A. (2013) 'Slaking behavior of clay-bearing rocks during a one-year exposure to natural climatic conditions', *Engineering Geology*, 166, pp. 17–25. doi:10.1016/j.enggeo.2013.08.003.
- Groenevelt, P.H. and Grant, C.D. (2004) 'Analysis of soil shrinkage data', *Soil and Tillage Research*, 79(1), pp. 71–77.
- Hattab, M., Hammad, T. and Fleureau, J.M. (2015) 'Internal friction angle variation in a kaolin/montmorillonite clay mix and microstructural identification', *Geotechnique*, 65(1), pp. 1–11. doi:10.1680/geot.13.P.081.
- Hopkins, T.C. and Beckham, T.L. (1998) 'Embankment construction using shale'.
- Hu, D.X. *et al.* (2018) 'Quantitative analysis of swelling and shrinkage cracks in expansive soil', *Rock and Soil Mechanics*, 39(S1), pp. 318–324.
- Ito, D & Komine, H. (2020). Evaluating influence of cementation on swelling properties of bentonite buffer material based on the results of bentonite ores, *Journal of JSCE*, 76(3), 295-305,.
- JGS 2006. Accelerated rock-slaking test. JGS 2125-2006, Laboratory Testing Standards of Geomaterials, *Japanese Geotechnical Society Standards*.
- JGS 2009. Test method for bulk density of soils. JGS 0191-2009. Laboratory Testing Standards of Geomaterials, *Japanese Geotechnical Society Standards*.
- JGS 2020. Determination of cation exchange capacity. JGS 0261-2020, Laboratory Testing Standards of Geomaterials, *Japanese Geotechnical Society Standards*.

- Jiang, G. *et al.* (2018) 'Field study on swelling-shrinkage response of an expansive soil foundation under high-speed railway embankment loads', *Soils and Foundations*, 58(6), pp. 1538–1552.
- Jiang, Q., Cui, J. and Feng, X. (2014) 'Application of computerized tomographic scanning to the study of water-induced weakening of mudstone', pp. 1293–1301. doi:10.1007/s10064-014-0597-5.
- JIS 2019. Test method for methylene blue adsorption on bentonite and acid clay. JIS standard Z2451. *Japanese Industrial Standard Committee*.
- JIS 2020. Test method for density of soil particles. JIS A 1202-2020, Laboratory Testing Standards of Geomaterials, *Japanese Geotechnical Society Standards*.
- JIS 2020. Test method for liquid and plastic limit of soils. JIS A 1205-2020, Laboratory Testing Standards of Geomaterials, *Japanese Geotechnical Society Standards*.
- Ju, X., Qiu, Z. and Yang, X. (2022) 'Settlement characteristics of mudstone embankments: a case study of He-chang Expressway in western China', *Arabian Journal of Geosciences*, 15(11), p. 1029.
- Kang, X. *et al.* (2015) 'Chemically stabilized soft clays for road-base construction', *Journal of Materials in Civil Engineering*, 27(7), p. 4014199.
- Kikumoto, M.Ã., Putra, A.D. and Fukuda, T. (2016) 'Slaking and deformation behavior', (9), pp. 771–785.
- Kodikara, J. and Costa, S. (2013) 'Desiccation cracking in clayey soils: Mechanisms and modelling', *Springer Series in Geomechanics and Geoengineering*, 3, pp. 21–32. doi:10.1007/978-3-642-32492-5\_2.
- Kolay, E. and Kayabali, K. (2006) 'Investigation of the effect of aggregate shape and surface roughness on the slake durability index using the fractal dimension approach', 86, pp. 271–284. doi:10.1016/j.enggeo.2006.05.007.



Komine, H. and Ogata, N. (1994) 'Experimental study on swelling characteristics of compacted bentonite', *Canadian geotechnical journal*, 31(4), pp. 478–490.

Komine, H. and Ogata, N. (2003) 'New equations for swelling characteristics of bentonite-based buffer materials', *Canadian Geotechnical Journal*, 40(2), pp. 460–475.

Komine, H., Yasuhara, K. and Murakami, S. (2009) 'Swelling characteristics of bentonites in artificial seawater', *Canadian Geotechnical Journal*, 46(2), pp. 177–189.

Konrad, J.-M. and Ayad, R. (1997) 'A idealized framework for the analysis of cohesive soils undergoing desiccation', *Canadian Geotechnical Journal*, 34(4), pp. 477–488.

Lee, D.H., Tien, K.G. and Juang, C.H. (1996) 'Full-scale field experimentation of a new technique for protecting mudstone slopes, Taiwan', *Engineering geology*, 42(1), pp. 51–63.

Li, J.H. and Zhang, L.M. (2010) 'Geometric parameters and REV of a crack network in soil', *Computers and Geotechnics*, 37(4), pp. 466–475.

Li, J.H. and Zhang, L.M. (2011) 'Study of desiccation crack initiation and development at ground surface', *Engineering Geology*, 123(4), pp. 347–358.

Li, X. *et al.* (2020) 'Microanisotropy and preferred orientation of grains and aggregates (POGA) of the Malan loess in Yan'an, China: a profile study', *Bulletin of Engineering Geology and the Environment*, 79(4), pp. 1893–1907.

doi:10.1007/s10064-019-01674-0.

Liu, C.-D. *et al.* (2021) 'Experimental study on the effect of water on mechanical properties of swelling mudstone', *Engineering Geology*, 295, p. 106448.

- Liu, X. *et al.* (2020) 'Assessing the slake durability of red stratum sandstone in different solution environments by a novel dual rotation test', *Engineering Geology*, 267(January), p. 105503. doi:10.1016/j.enggeo.2020.105503.
- Liu, X., Zhao, M. and Su, Y. (2006) 'Improvement and application of fractal model to size distribution of sedimentary rock and soil.', *Yanshilixue Yu Gongcheng Xuebao/Chinese Journal of Rock Mechanics and Engineering*, 25(8), pp. 1691–1697.
- Mingbin, X.U. and Guoguo, C. (2015) 'Engineering Properties of Pliocene Mudstone in Xihe-Tianshui Section of Shitian Expressway', *Soil Engineering and Foundation*, 29(5), p. 23.
- Ministry of Land, Infrastructure and Transport. "High Standard Trunk Road Map" (PDF). Archived from the original (pdf) on September 20, 2011. Retrieved 2008-04-13.
- Ministry of Land, Infrastructure and Transport. "Nihonkai Engan Tohoku Expressway Construction Status". Retrieved 2008-04-17.
- Mo, F. *et al.* (2011) 'Evaluation of soil and water conservation capacity of different forest types in Dongling Mountain', *Shengtai Xuebao/Acta Ecologica Sinica*, 31(17), pp. 5009–5016.
- Moore, D.M. and Reynolds Jr, R.C. (1989) *X-ray Diffraction and the Identification and Analysis of Clay Minerals*. Oxford University Press (OUP).
- Morris, P.H., Graham, J. and Williams, D.J. (1992) 'Cracking in drying soils', *Canadian Geotechnical Journal*, 29(2), pp. 263–277.
- Peng, X. and Horn, R. (2005) 'Modeling soil shrinkage curve across a wide range of soil types', *Soil Science Society of America Journal*, 69(3), pp. 584–592.

- Peng, X. and Horn, R. (2013) 'Identifying Six Types of Soil Shrinkage Curves from a Large Set of Experimental Data', *Soil Science Society of America Journal*, 77(2), pp. 372–381. doi:10.2136/sssaj2011.0422.
- Peron, H. *et al.* (2009) 'Fundamentals of desiccation cracking of fine-grained soils: Experimental characterisation and mechanisms identification', *Canadian Geotechnical Journal*, 46(10), pp. 1177–1201. doi:10.1139/T09-054.
- Perras, M.A., Wannemacher, H. and Diederichs, M.S. (2015) 'Underground excavation behavior of the queenston formation: tunnel back analysis for application to shaft damage dimension prediction', *Rock Mechanics and Rock Engineering*, 48(4), pp. 1647–1671.
- Raju, R. A., Lim, S., Akiyama, M., & Kageyama, T. (2020). Effects of concrete flow on the distribution and orientation of fibers and flexural behavior of steel fiber-reinforced self-compacting concrete beams. *Construction and Building Materials*, 262, 119963.
- Rayhani, M.H.T., Yanful, E.K. and Fakher, A. (2007) 'Desiccation-induced cracking and its effect on the hydraulic conductivity of clayey soils from Iran', *Canadian geotechnical journal*, 44(3), pp. 276–283.
- Sadeghi, H. and Nasiri, H. (2021) 'Hysteresis of soil water retention and shrinkage behavior for various salt concentrations', *Géotechnique Letters*, 11(1), pp. 21–29.
- Sakai, T. and Nakano, M. (2019) 'ScienceDirect Effects of slaking and degree of compaction on the mechanical properties of mudstones with varying slaking properties', *Soils and Foundations*, 59(1), pp. 56–66.  
doi:10.1016/j.sandf.2018.09.004.

- Sattar, A. *et al.* (2011) ‘Measurement of debris mass changes and assessment of the dam-break flood potential of earthquake-triggered Hattian landslide dam’, *Landslides*, 8(2), pp. 171–182.
- Selen, L., Panthi, K.K. and Vistnes, G. (2020) ‘An analysis on the slaking and disintegration extent of weak rock mass of the water tunnels for hydropower project using modified slake durability test’, pp. 1919–1937.
- Shakoor, T.P.G.A. (2016) ‘Comparing the Slaking of Clay-Bearing Rocks Under Laboratory Conditions to Slaking Under Natural Climatic Conditions’, *Rock Mechanics and Rock Engineering*, pp. 19–31. doi:10.1007/s00603-015-0729-7.
- Shamburger, J.H., Patrick, D.M. and Lutton, R.J. (1975) *DESIGN AND CONSTRUCTION OF COMPACTED SHALE EMBANKMENTS. VOLUME 1. SURVEY OF PROBLEM AREAS AND CURRENT PRACTICES.*
- Shen, P. *et al.* (2019) ‘Experimental study of slaking properties of red- bed mudstones from the Three Gorges Reservoir area’, *Marine Georesources & Geotechnology*, 37(8), pp. 891–901. doi:10.1080/1064119X.2018.1504839.
- Shi, B., Chen, S. and Zheng, C. (2014) ‘Expansive soil crack depth under cumulative damage’, in *Soil Behavior and Geomechanics*, pp. 1–14.
- Shi, B., Murakami, Y. and Wu, Z. (1998) ‘Orientation of aggregates of fine-grained soil: quantification and application’, *Engineering Geology*, 50(1–2), pp. 59–70.
- Shin, H. and Santamarina, J.C. (2011) ‘Desiccation cracks in saturated fine-grained soils: particle-level phenomena and effective-stress analysis’, *Géotechnique*, 61(11), p. 961.
- Stirk, G.B. (1954) ‘Some aspects of soil shrinkage and the effect of cracking upon water entry into the soil’, *Australian Journal of Agricultural Research*, 5(2), pp. 279–296. doi:10.1071/AR9540279.

- Su, X. *et al.* (2020) ‘The role of pH in red-stratum mudstone disintegration in the Three Gorges reservoir area , China , and the associated micromechanisms’, *Engineering Geology*, 279(October 2019), p. 105873.  
doi:10.1016/j.enggeo.2020.105873.
- Sun, C. *et al.* (2020) ‘Meso-scale mechanical properties of mudstone investigated by nanoindentation’, *Engineering Fracture Mechanics*, 238, p. 107245.
- Tafti, A.P. *et al.* (2015) ‘Recent advances in 3D SEM surface reconstruction’, *Micron*, 78, pp. 54–66. doi:10.1016/j.micron.2015.07.005.
- Tang, C.-S. *et al.* (2011) ‘Experimental investigation of the desiccation cracking behavior of soil layers during drying’, *Journal of Materials in Civil Engineering*, 23(6), pp. 873–878.
- Tang, C.-S. *et al.* (2019) ‘Three-dimensional characterization of desiccation cracking behavior of compacted clayey soil using X-ray computed tomography’, *Engineering geology*, 255, pp. 1–10.
- Tang, C.-S. *et al.* (2020) ‘Quantification and characterizing of soil microstructure features by image processing technique’, *Computers and Geotechnics*, 128, p. 103817.
- Tang, C.S. *et al.* (2019) ‘Three-dimensional characterization of desiccation cracking behavior of compacted clayey soil using X-ray computed tomography’, *Engineering Geology*, 255, pp. 1–10.
- Thoeni, K. *et al.* (2014) ‘A COMPARISON OF MULTI-VIEW 3D RECONSTRUCTION OF A ROCK WALL USING SEVERAL CAMERAS AND A LASER SCANNER.’, *International Archives of the Photogrammetry, Remote Sensing & Spatial Information Sciences*, 45.

- Tollenaar, R.N., Van Paassen, L.A. and Jommi, C. (2017) ‘Observations on the desiccation and cracking of clay layers’, *Engineering geology*, 230, pp. 23–31.
- Towner, G.D. (1988) ‘The influence of sand-and silt-size particles on the cracking during drying of small clay-dominated aggregates’, *Journal of Soil Science*, 39(3), pp. 347–356.
- Tyler, S.W. and Wheatcraft, S.W. (1992) ‘Fractal scaling of soil particle-size distributions: Analysis and limitations’, *Soil Science Society of America Journal*, 56(2), pp. 362–369.
- Vanneschi, C. *et al.* (2019) ‘SFM-MVS photogrammetry for rockfall analysis and hazard assessment along the ancient roman via Flaminia road at the Furlo gorge (Italy)’, *ISPRS International Journal of Geo-Information*, 8(8).  
doi:10.3390/ijgi8080325.
- Vogel, H.J. *et al.* (2005) ‘Studies of crack dynamics in clay soil: I. Experimental methods, results, and morphological quantification’, *Geoderma*, 125(3–4), pp. 203–211. doi:10.1016/j.geoderma.2004.07.009.
- Wang, G. *et al.* (2011) ‘Deformation characteristics of rock salt with mudstone interbeds surrounding gas and oil storage cavern’, *International Journal of Rock Mechanics and Mining Sciences*, 48(6), pp. 871–877.
- Wang, H. *et al.* (2020) ‘Movement of water in compacted bentonite and its relation with swelling pressure’, *Canadian Geotechnical Journal*, 57(6), pp. 921–932.
- Wang, H., Komine, H. and Gotoh, T. (2022) ‘A swelling pressure cell for X-ray diffraction test’, *Géotechnique*, 72(8), pp. 675–686.
- Wang, J. jie *et al.* (2018) ‘Shear strength of sandstone–mudstone particle mixture from direct shear test’, *Environmental Earth Sciences*, 77(12), pp. 1–12.  
doi:10.1007/s12665-018-7622-0.

- Wang, L. *et al.* (2015) ‘Microscale insight into the influence of humidity on the mechanical behavior of mudstones’, *Journal of Geophysical Research: Solid Earth*, 120(5), pp. 3173–3186.
- Weinberger, R. (1999) ‘Initiation and growth of cracks during desiccation of stratified muddy sediments’, *Journal of structural geology*, 21(4), pp. 379–386.
- Wöhler, C. (2012) *3D computer vision: efficient methods and applications*. Springer Science & Business Media.
- Xiao, Y. *et al.* (2020). Restraint of particle breakage by biotreatment method. *Journal of Geotechnical and Geoenvironmental Engineering*, 146(11), 04020123.
- Yamaguchi, H. *et al.* (1988) ‘Slaking and shear properties of mudstone’, in *ISRM International Symposium*. OnePetro.
- Yang, Z.C., Zhang, J.Y. and Zhou, D. (2006) ‘Study on fast weathering characteristics of red bed mudstone slope’, *Chinese Journal of Rock Mechanics and Engineering*, 25(2), pp. 275–283.
- Yao, E. *et al.* (2022) ‘Experimental and Mechanistic study of mudstone volumetric swelling at the bottom of salt cavern gas storage’, *Arabian Journal of Chemistry*, 15(9), p. 104082.
- Yasuda, S. *et al.* (2012) ‘Reduction of static and dynamic shear strength due to the weathering of mudstones’, in *Proceedings of the 15th World Conference on Earthquake Engineering, Lisboa*, pp. 4–11.
- Yuan, S. *et al.* (2016) ‘Multi-scale characterization of swelling behavior of compacted Maryland clay’, *Acta Geotechnica*, 11(4), pp. 789–804.
- Yuan, S. *et al.* (2019) ‘Swelling behavior of compacted Maryland clay under different boundary conditions’, *Géotechnique*, 69(6), pp. 514–525.

- Zabat, M. *et al.* (1997) ‘Surface topography and mechanical properties of smectite films’, in *Trends in Colloid and Interface Science XI*. Springer, pp. 96–102.
- Zeng, Z. and Kong, L. (2019) ‘Effect of wetting–drying–freezing–thawing cycles on the swelling behavior of the Yanji mudstone’, *Environmental Earth Sciences*, 78, pp. 1–14.
- Zhang, C.L., Wicczorek, K. and Xie, M.L. (2010) ‘Swelling experiments on mudstones’, *Journal of Rock Mechanics and Geotechnical Engineering*, 2(1), pp. 44–51.
- Zhang, D. *et al.* (2015) ‘Geomorphology Quantitative determination of the effect of temperature on mudstone decay during wet – dry cycles : A case study of “ purple mudstone ” from’, *Geomorphology*, 246, pp. 1–6.  
doi:10.1016/j.geomorph.2015.06.011.
- Zhang, H. *et al.* (2017) ‘Mechanism of the mudstone tunnel failures induced by expansive clay minerals’, *Geotechnical and Geological Engineering*, 35, pp. 263–275.
- Zhang, X. *et al.* (2020) ‘Engineering geology of residual soil derived from mudstone in Zimbabwe’, *Engineering Geology*, 277(July), p. 105785.  
doi:10.1016/j.enggeo.2020.105785.
- Zhang, Z. *et al.* (2020) ‘Disintegration law of strongly weathered purple mudstone on the surface of the drawdown area under conditions of Three Gorges Reservoir operation’, *Engineering Geology*, 270(November 2018), p. 105584.  
doi:10.1016/j.enggeo.2020.105584.
- Zhong, S. *et al.* (2016) ‘Shear strength features of soils developed from purple clay rock and containing less than two-millimeter rock fragments’, *Journal of Mountain Science*, 13, pp. 1464–1480.



## Chapter 12. Figure list

<b>Figure 1-1 Failure of highway embankment and slaking problem of mudstone in Japan</b> .....	7
<b>Figure 1-2 Road diseases in He-chang Expressway, China (Ju, Qiu and Yang, 2022)</b> .....	8
<b>Figure 1-3 Cracking ground on the field besides high-speed rail in southwest of China</b> .....	9
<b>Figure 1-4 Research flow</b> .....	17
<b>Figure 2-1 Outlooking of three kinds of mudstone:(a) Black mudstone; (b) Terashima mudstone (c) Akita mudstone</b> .....	19
<b>Figure 2-2 Soil particle density testing details</b> .....	19
<b>Figure 2-3 Liquid limits testing device</b> .....	21
<b>Figure 2-4 Montmorillonite content testing details</b> .....	23
<b>Figure 2-5 Results of accelerated rock-slaking tests</b> .....	25
<b>Figure 2-6 XRD apparatus</b> .....	26
<b>Figure 2-7 XRD results of Akita mudstone</b> .....	27
<b>Figure 2-8 XRD result of Terashima mudstone</b> .....	28
<b>Figure 2-9 XRD result of hard black mudstone</b> .....	29
<b>Figure 2-10 XRD result of medium black mudstone</b> .....	29
<b>Figure 2-11 XRD result of soft black mudstone</b> .....	30
<b>Figure 2-12 Scanning electron microscope (JEOL JSM-IT100LA)</b> .....	31
<b>Figure 2-13 SEM image of hard black mudstone</b> .....	31
<b>Figure 2-14 SEM image of medium black mudstone</b> .....	32
<b>Figure 2-15 SEM image of soft black mudstone</b> .....	32
<b>Figure 3-1 (a) Photo and (b) schematic diagram of equipments for swelling strain test</b> .....	35
<b>Figure 3-2 Preparation of natural and remodeled mudstone</b> .....	36
<b>Figure 3-3 Static compression device</b> .....	36
<b>Figure 3-4 (a) Mixture of Akita mudstone with distilled water and different concentration of NaCl solution and (b) centrifugation device</b> .....	39
<b>Figure 3-5 Ion analyzer (IA-300)</b> .....	39

<b>Figure 3-6 Swelling strain evolution curves of remodeled black mudstones with different dry densities .....</b>	<b>41</b>
<b>Figure 3-7 Swelling pressure evolution curves of remodeled black mudstone with different dry densities .....</b>	<b>41</b>
<b>Figure 3-8 Swelling strain evolution curves of remodeled Terashima mudstones with different dry densities .....</b>	<b>41</b>
<b>Figure 3-9 The evolution of final swelling strains with dry densities.....</b>	<b>42</b>
<b>Figure 3-10 Swelling strain evolution curves of remodeled Akita mudstones with different dry densities .....</b>	<b>44</b>
<b>Figure 3-11 The evolution of final swelling strains with dry densities.....</b>	<b>44</b>
<b>Figure 3-12 Swelling strains of natural and remolded Akita mudstone.....</b>	<b>45</b>
<b>Figure 3-13 Swelling pressure evolution curves of remodeled Akita mudstones with different dry densities .....</b>	<b>46</b>
<b>Figure 3-14 The evolution of final swelling pressures of Akita mudstone with dry densities .....</b>	<b>47</b>
<b>Figure 3-15 The evolution of final swelling strain with dry densities under different vertical confine stress .....</b>	<b>49</b>
<b>Figure 3-16 Swelling strain of Akita mudstone with different concentration of NaCl solution and different vertical confine stresses .....</b>	<b>50</b>
<b>Figure 3-17 The leached Ca<sup>+</sup> and Mg<sup>+</sup> concentration from supernatants ..</b>	<b>51</b>
<b>Figure 4-1 Devices used in this study: (a) Drone; (b) High resolution Camera; (c) Low resolution Camera; (d) Scanning Electron Microscope; (e) Laser scanning microscope; (f) Optical microscope ...</b>	<b>55</b>
<b>Figure 4-2 Muti-view approach process .....</b>	<b>58</b>
<b>Figure 4-3 Images obtained from SEM for muti-view approach .....</b>	<b>59</b>
<b>Figure 4-4 3D structure obtained by muti-view approach with or without background plate .....</b>	<b>62</b>
<b>Figure 4-5 The improvement of muti-view approach using colored plate ...</b>	<b>63</b>
<b>Figure 4-6 3D models of cuboid with different reconstruction resolutions and different camera resolutions.....</b>	<b>67</b>
<b>Figure 5-1 (a) Photo and (b) diagram of equipment for the vacuum slaking test.....</b>	<b>70</b>
<b>Figure 5-2 Process of atmospheric and vacuum cyclic drying-wetting test..</b>	<b>71</b>
<b>Figure 5-3 Schematic diagram of particles with different Shape-3d (<math>S_{3d}</math>)....</b>	<b>72</b>
<b>Figure 5-4 Specimens during cyclic drying–wetting slaking tests .....</b>	<b>72</b>

<b>Figure 5-5 Some typical particles in the slaking process: (a) primary body particle (b) medium particles .....</b>	<b>73</b>
<b>Figure 5-6 Particle size distribution curves for (a) atmospheric and (b) vacuum cyclic drying–wetting slaking tests.....</b>	<b>74</b>
<b>Figure 5-7 (a) Mathematical derivation of the slaking ratio and (b) relationship between <math>SL_{ratio}</math> and the number of cycles.....</b>	<b>77</b>
<b>Figure 5-8 Sampling method.....</b>	<b>79</b>
<b>Figure 5-9 (a) Curve of Shape-3d (<math>S_{3d}</math>) with original data point and (b) Curve of <math>S_{3d}</math> after removing original data points .....</b>	<b>81</b>
<b>Figure 5-10 Shape-3d (<math>S_{3d}</math>) of different particle sizes in atmospheric slaking tests .....</b>	<b>82</b>
<b>Figure 5-11 Shape-3d (<math>S_{3d}</math>) of different particle sizes in vacuum slaking tests .....</b>	<b>83</b>
<b>Figure 5-12 Evolution of <math>P_v</math> and <math>R_v</math> in cyclic atmospheric and vacuum slaking tests.....</b>	<b>84</b>
<b>Figure 5-13 Two co-existing mechanisms for Akita mudstone slaking.....</b>	<b>86</b>
<b>Figure 5-14 Relationship between <math>S_{3d}</math> and mass-size fractal dimension .....</b>	<b>88</b>
<b>Figure 6-1 Cycle slaking process under vertical stress.....</b>	<b>91</b>
<b>Figure 6-2 Devices for applying stresses in wetting-drying cycle slaking tests .....</b>	<b>92</b>
<b>Figure 6-3 Drying process: (a)before drying and (b)after drying .....</b>	<b>92</b>
<b>Figure 6-4 Direct shear instrument used in this study .....</b>	<b>93</b>
<b>Figure 6-5 Particles size distribution curves during slaking test under different stresses.....</b>	<b>94</b>
<b>Figure 6-6 Mathematical derivation of the slaking ratio .....</b>	<b>95</b>
<b>Figure 6-7 Evolution of <math>SL_{ratio}</math> with slaking process under different vertical stress .....</b>	<b>96</b>
<b>Figure 6-8 An example of relationship between horizontal deformation and shear stress (vertical stress: 0MPa; number of cycle: 6) .....</b>	<b>96</b>
<b>Figure 6-9 Shear strength evolution during the slaking process .....</b>	<b>97</b>
<b>Figure 6-10 Summarize of <math>c</math> and <math>\phi</math> during slaking process .....</b>	<b>98</b>
<b>Figure 6-11 Mechanism of mudstone slaking (a)without vertical stress or (b)with vertical stress.....</b>	<b>99</b>
<b>Figure 7-1 Equipments used for taking pictures in this study.....</b>	<b>103</b>

<b>Figure 7-2 Image process.....</b>	<b>104</b>
<b>Figure 7-3 WP4C Dewpoint Potential Meter .....</b>	<b>104</b>
<b>Figure 7-4 Some specimens for shrinkage test .....</b>	<b>105</b>
<b>Figure 7-5 Wax sealing process .....</b>	<b>106</b>
<b>Figure 7-6 volume measurement equipments.....</b>	<b>107</b>
<b>Figure 7-7 Images for specimen during cracking with distilled water .....</b>	<b>108</b>
<b>Figure 7-8 Images for specimen during cracking with 2% NaCl solution .</b>	<b>109</b>
<b>Figure 7-9 Images for specimen during cracking with 5% NaCl solution .</b>	<b>110</b>
<b>Figure 7-10 Images for specimen during cracking with 10% NaCl solution .....</b>	<b>111</b>
<b>Figure 7-11 Images for specimen during cracking with 15% NaCl solution .....</b>	<b>112</b>
<b>Figure 7-12 The water loss rate of the samples under distilled water and different concentrations of sodium chloride.....</b>	<b>114</b>
<b>Figure 7-13 Relationship between moisture content and crack ratios.....</b>	<b>115</b>
<b>Figure 7-14 Soil-water retention curves (SWRC) of Akita mudstone .....</b>	<b>116</b>
<b>Figure 7-15 Pictures of totally dried specimens for SSCC tests .....</b>	<b>118</b>
<b>Figure 7-16 Soil-water retention curves of specimens saturated by different concentration of sodium chloride solution.....</b>	<b>118</b>
<b>Figure 7-17 The relationship between final void ratio and concentration of NaCl.....</b>	<b>119</b>
<b>Figure 7-18 The relationship between cracking evolution and shrinkage behavior .....</b>	<b>122</b>
<b>Figure 7-19 The relationship between final crack ratio (<math>R_c</math>) and final void ratio (<math>e</math>).....</b>	<b>123</b>
<b>Figure 8-1 Equipments used in this study: (a) Slaking test instrument (b) Vacuum chamber .....</b>	<b>128</b>
<b>Figure 8-2 Typical image processing and data acquisition: (a) SEM image acquisition; (b) particle orientation obtained from image; (c) pore orientation obtained from skeletonized model; and (d) details of skeletonizing. ....</b>	<b>129</b>
<b>Figure 8-3 SEM image of compacted crushed mudstone specimen .....</b>	<b>131</b>
<b>Figure 8-4 Evaporation of water .....</b>	<b>132</b>
<b>Figure 8-5 Slaking curves of Terashima mudstone .....</b>	<b>133</b>

<b>Figure 8-6 Slaking curves of black mudstone.....</b>	<b>133</b>
<b>Figure 8-7 Process of slaking .....</b>	<b>135</b>
<b>Figure 8-8 Slaking curves of black mudstone.....</b>	<b>137</b>
<b>Figure 8-9 Compression of entrapped air.....</b>	<b>138</b>
<b>Figure 8-10 Pore size distribution characteristic .....</b>	<b>139</b>
<b>Figure 8-11. Rosette Histogram of pore orientation distribution.....</b>	<b>141</b>
<b>Figure 8-12. Rosette Histogram of particle orientation distribution. ....</b>	<b>142</b>
<b>Figure 8-13. Schematic diagram of determining the general direction and anisotropy parameters.....</b>	<b>143</b>
<b>Figure 8-14. The relationship between anisotropy index and dry density..</b>	<b>144</b>
<b>Figure 8-15 Evolution of pore orientation during compaction .....</b>	<b>144</b>
<b>Figure 9-1 Location of embankments in Japan from which mudstone specimens were sourced (Kikumoto, Putra and Fukuda, 2016) .....</b>	<b>148</b>
<b>Figure 9-2 Nihonkai-Tōhoku Expressway (modified from <a href="https://en.wikipedia.org/wiki/Nihonkai-T%C5%8Dhoku_Expressway#/map/0">https://en.wikipedia.org/wiki/Nihonkai-T%C5%8Dhoku_Expressway#/map/0</a>).....</b>	<b>149</b>
<b>Figure 9-3 Slaking problem of mudstone in embankment and tunnel .....</b>	<b>150</b>
<b>Figure 9-4 Surficial slaking phenomenon of Wulidui slope: (a) surficial slaking zonation of the slope and (b) surficial slaking in lower and middle parts of the slope (Z. Zhang <i>et al.</i>, 2020) .....</b>	<b>151</b>
<b>Figure 9-5 Swelling strain of three kinds of mudstone (stress: 7.95kpa)....</b>	<b>153</b>
<b>Figure 9-6 Swelling strain of Akita mudstone with different concentration of NaCl solution and different vertical confine stress .....</b>	<b>153</b>
<b>Figure 9-7 Suggestion for avoiding lift of embankment.....</b>	<b>154</b>
<b>Figure 9-8 (a)Shrinkage and (b)cracking evolution of Akita mudstone .....</b>	<b>156</b>
<b>Figure 9-9 Application of muti-view approach on large scale .....</b>	<b>157</b>
<b>Figure 9-10 Slope failure SV map of Aratozawa - aerial view from Chuo Kaihatsu Corporation (<a href="https://www.ckcnet.co.jp/technology/survey/geodx/">https://www.ckcnet.co.jp/technology/survey/geodx/</a>).....</b>	<b>158</b>
<b>Figure 9-11 Application of SfM-MVS approach on research such as (a) Bending tests of concrete (Raju R A, Lim S, Akiyama M, et al. ) and (b) Different shapes of sands after breakage (Xiao Y, Chen H, Stuedlein A W, et al.) .....</b>	<b>158</b>
<b>Figure 9-12 Suggestion for slaking problem in tunnel .....</b>	<b>159</b>

<b>Figure 9-13 Evolution of <math>SL_{ratio}</math> with slaking process under different vertical stress .....</b>	<b>160</b>
<b>Figure 9-14 Summarize of <math>c</math> and <math>\phi</math> during slaking process .....</b>	<b>160</b>
<b>Figure 9-15 Suggestion for avoiding failure of embankment.....</b>	<b>161</b>

**Chapter 13. Table list**

<b>Table 2-1 Soil particle densities of mudstones.....</b>	<b>20</b>
<b>Table 2-2 Liquid and plastic limits of mudstones .....</b>	<b>22</b>
<b>Table 2-3 Montmorillonite contents of bentonites .....</b>	<b>22</b>
<b>Table 2-4 Definition of slaking classes (JGS 2125-2006) .....</b>	<b>23</b>
<b>Table 3-1 Specimens information for swelling pressure tests .....</b>	<b>34</b>
<b>Table 3-2 Specimen details for swelling strain test.....</b>	<b>36</b>
<b>Table 3-3 Akita mudstone specimen details for swelling strain test with different concentration of NaCl solution under vertical confining stress .....</b>	<b>37</b>
<b>Table 4-1 Configuration features of devices used in this study .....</b>	<b>55</b>
<b>Table 4-2 Results of multi-view approach in different scales .....</b>	<b>60</b>
<b>Table 4-3 Results of using multi-view approach with or without colored plate and CT scanner .....</b>	<b>64</b>
<b>Table 4-4 Results of parameters extracted from cuboid model with different camera resolution and reconstruction resolutions .....</b>	<b>66</b>
<b>Table 4-5 Results of multi-view approach and laser microscope for one sand .....</b>	<b>68</b>
<b>Table 5-1 specimens of original images, surface models and 3D models.....</b>	<b>80</b>
<b>Table 8-1 Information of specimens for different tests .....</b>	<b>126</b>
<b>Table 8-3 Results of EDS analysis .....</b>	<b>131</b>

## List of research achievements for application of Doctor of Engineering, Waseda University

Full Name : 孫 丹曦

seal or signature

Date Submitted(yyyy/mm/dd):

2023/10/5

種類別 (By Type)	題名、 発表・発行掲載誌名、 発表・発行年月、 連名者 (申請者含む) (theme, journal name, date & year of publication, name of authors inc. yourself)
1. Journal paper	
○Journal paper	<u>Sun Danxi</u> , Liu Xian-feng, Yuan Sheng-yang, Pan Gaofeng, Jiang Guanlu, Wang Hailong, Komine Hideo, Olivier Buzzi. "Three-dimensional characterization of cracks in undisturbed Mile expansive soil using X-ray computed tomography". Soils and Foundations, 2023, 63(3): 101282.
2. Presentation	
○Presentation	<u>Sun Danxi</u> , Komine Hideo, Ito Daichi, Takagi Makiko. 2023. "Study of pore orientation in compacted crushed mudstone by SEM image". 17th Asian Regional Conference on Soil Mechanics and Geotechnical Engineering. Astana, KAZAKHSTAN.
○Presentation	<u>Sun Danxi</u> , Jiang Guanlu, Liu Xianfeng, Komine Hideo, Wang Hailong. 2021. "Study of crack ratio of undisturbed Mile expansive soil via x-ray computed tomography". The 56th annual meeting of the Japan national conference on geotechnical engineering. Yamagata, JAPAN.
○Presentation	<u>Sun Danxi</u> , Jiang Guanlu, Liu Xianfeng, Komine Hideo, Wang Hailong. 2021. "Study of crack orientation of undisturbed mile expansive soil via x-ray computed tomography". 76 th Annual Meeting of the Japan Society of Civil Engineers. Kanagawa, JAPAN.
○Presentation	<u>Sun Danxi</u> , Komine Hideo, Wang Hailong. 2022. "Three-dimensional particle analysis during slaking behavior of Akita mudstone by photographic method. Part I". The 57th annual meeting of the Japan national conference on geotechnical engineering. Niigata, JAPAN.
○Presentation	<u>Sun Danxi</u> , Komine Hideo, Wang Hailong. 2022. "Three-dimensional particle analysis during slaking behavior of Akita mudstone by photographic method. Part II". 77 th Annual Meeting of the Japan Society of Civil Engineers. Kyoto, JAPAN.